

University of Windsor

Scholarship at UWindor

Electronic Theses and Dissertations

Theses, Dissertations, and Major Papers

2014

Mechanical and Material Characterization of Mining Wheels for Enhanced Safety

Sante DiCecco
University of Windsor

Follow this and additional works at: <https://scholar.uwindsor.ca/etd>

Recommended Citation

DiCecco, Sante, "Mechanical and Material Characterization of Mining Wheels for Enhanced Safety" (2014). *Electronic Theses and Dissertations*. 5157.
<https://scholar.uwindsor.ca/etd/5157>

This online database contains the full-text of PhD dissertations and Masters' theses of University of Windsor students from 1954 forward. These documents are made available for personal study and research purposes only, in accordance with the Canadian Copyright Act and the Creative Commons license—CC BY-NC-ND (Attribution, Non-Commercial, No Derivative Works). Under this license, works must always be attributed to the copyright holder (original author), cannot be used for any commercial purposes, and may not be altered. Any other use would require the permission of the copyright holder. Students may inquire about withdrawing their dissertation and/or thesis from this database. For additional inquiries, please contact the repository administrator via email (scholarship@uwindsor.ca) or by telephone at 519-253-3000ext. 3208.

Mechanical and Material Characterization of Mining Wheels for Enhanced Safety

By

Sante DiCecco

A Thesis

Submitted to the Faculty of Graduate Studies
through the Department of Engineering Materials
in Partial Fulfillment of the Requirements for
the Degree of Master of Applied Science
at the University of Windsor

Windsor, Ontario, Canada

2013

© 2013 Sante DiCecco

Mechanical and Material Characterization of Mining Wheels for Enhanced Safety

by

Sante DiCecco

APPROVED BY:

B. Minaker

Mechanical, Automotive, and Materials Engineering

R. Bowers

Mechanical, Automotive, and Materials Engineering

W. Altenhof, Advisor

Mechanical, Automotive, and Materials Engineering

H. Hu, Co-Advisor

Mechanical, Automotive, and Materials Engineering

15 April, 2014

AUTHOR'S DECLARATION OF ORIGINALITY

I hereby certify that I am the sole author of this thesis and that no part of this thesis has been published or submitted for publication.

I certify that, to the best of my knowledge, my thesis does not infringe upon anyone's copyright nor violate any proprietary rights and that any ideas, techniques, quotations, or any other material from the work of other people included in my thesis, published or otherwise, are fully acknowledged in accordance with the standard referencing practices. Furthermore, to the extent that I have included copyrighted material that surpasses the bounds of fair dealing within the meaning of the Canada Copyright Act, I certify that I have obtained a written permission from the copyright owner(s) to include such material(s) in my thesis and have included copies of such copyright clearances to my appendix.

I declare that this is a true copy of my thesis, including any final revisions, as approved by my thesis committee and the Graduate Studies office, and that this thesis has not been submitted for a higher degree to any other University or Institution.

ABSTRACT

A study was undertaken to evaluate the mechanical and material behaviour of the Q345 alloy, used in fabrication of five-piece mining wheel assemblies. Material samples were extracted from all components of a five-piece wheel. Material testing included compositional analyses, fully submerged corrosion testing, and microstructural analyses. Mechanical testing included hardness testing, tensile testing and stress-based high-cycle fatigue testing of specimens with polished and pre-corroded surface conditions. Special emphasis was placed on obtaining the fatigue behaviour of the alloy in the pre-corroded condition. Component microstructures were all found to consist of ferrite and colony pearlite. Ultimate tensile strengths of most component samples ranged from 471 MPa to 544 MPa, which was within minimum alloy specifications. Fatigue results found polished specimens and pre-corroded specimens to have endurance strengths of approximately 295 MPa and 222 MPa, respectively, at 5,000,000 cycles. The pre-corroded condition resulted in a decrease in fatigue strength of 25.6%.

DEDICATION

In loving memory of
Anne Eldracher-DiCecco

ACKNOWLEDGEMENTS

This study was completed under the supervision and guidance of my advisors, Dr. William Altenhof and Dr. Henry Hu. I am thankful for their support, encouragement, and, most notably, patience during the past two and a half years of my studies. From their efforts, I have been able to learn the skills required to succeed both academically and within the workplace.

I would like to express my appreciation to committee members Dr. Bruce Minaker and Dr. Randy Bowers, both of whom have always offered constructive criticism regarding my work. Additionally, I am thankful to Mr. Richard Banting, who provided input regarding my studies.

I would like to give acknowledgement to all technical staff within Faculty of Engineering; with special emphasis given to Andy Jenner, who, without a doubt, played a critical role in ensuring my completion in a timely manner.

Graciously acknowledged is the financial support of the Natural Sciences and Engineering Research Council of Canada (NSERC), the Government of Ontario (OGS), and the Workplace Safety and Insurance Board (WSIB).

Finally, I would like to thank my friends and family for their constant support and encouragement.

TABLE OF CONTENTS

Author's Declaration of Originality.....	iii
Abstract.....	iv
Dedication.....	v
Acknowledgements.....	vi
List of Tables	ix
List of Figures.....	x
1. Introduction.....	1
1.1. Background.....	1
1.2. Objectives of Study.....	3
1.3. Scope of Study	4
1.4. Organization of Study.....	5
2. Literature Review	7
2.1. Multi-Piece Mining Wheel Failures.....	7
2.1.1. Multi-Piece Wheel Failure Incident Reports	8
2.1.2. Failure Analysis of a Cracked Wheel Rim	10
2.2. Fatigue in Metals.....	11
2.2.1. Stages of Fatigue.....	12
2.2.2. Fatigue Design Approaches	17
2.2.3. Fatigue Life Factors	21
2.3. Statistical Analysis of Fatigue Data.....	26
2.3.1. Testing and Data Sampling.....	27
2.3.2. Curve Fitting.....	29
2.3.3. Confidence Bands	32
2.4. Corrosion Testing of Steels.....	34
2.4.1. Corrosion in the Mining Environment.....	36
2.4.2. Accelerated Corrosion Testing Standards.....	42
2.5. Properties of Mining Wheel Fabrication Material	46
2.5.1. Tensile Studies	47
2.5.2. Fatigue Studies.....	48
2.5.3. Corrosion Studies.....	50
2.6. Summary of Literature Review.....	52

3.	Experimental Procedures	53
3.1.	Specimen Extraction	54
3.2.	Energy Dispersive Spectroscopy Analysis	55
3.3.	Accelerated Corrosion Testing	56
3.3.1.	Mass-Loss	56
3.3.2.	Surface Roughness.....	59
3.4.	Optical Microscopy.....	60
3.5.	Cross-Sectional Hardness Measurements	62
3.6.	Tensile Testing.....	64
3.7.	Fatigue Testing and Analysis.....	66
3.7.1.	Fatigue Testing Procedures.....	67
3.7.2.	Statistical Analysis of Fatigue Data.....	72
3.7.3.	Surface Analysis	74
3.7.4.	Fatigue Testing Matrix.....	75
4.	Results and Discussion	77
4.1.	Energy Dispersive Spectroscopy Analysis	78
4.2.	Corrosion Behaviour.....	80
4.2.1.	Mass-Loss	81
4.2.2.	Surface Roughness.....	85
4.3.	Microstructure.....	88
4.4.	Cross-Sectional Hardness	97
4.5.	Tensile Properties.....	100
4.6.	Fatigue Properties	106
4.6.1.	As-Extracted Fatigue Behaviour.....	107
4.6.2.	Pre-Corroded Fatigue Behaviour	115
4.6.3.	Fracture Surface Analysis	122
4.7.	Summary of Results	128
5.	Conclusions and Recommendations	131
	References.....	137
	Appendix A: Summary of Corrosion Conditions in Select Mines	142
	Vita Auctoris.....	143

LIST OF TABLES

Table 2.1 ASTM E739 fatigue test sampling recommendations	28
Table 2.2: Chemical composition of Q345 and A572 G50	47
Table 3.1: Estimated cycles to fatigue failure and corresponding loads.....	71
Table 3.2: Initial fatigue testing matrix.....	76
Table 4.1: EDS analysis of all components of a five-piece mining wheel with corrections made to include a nominal carbon content of 0.2 wt%	80
Table 4.2: Summary of surface area mass-loss corrosion data discussed in 4.2.1	85
Table 4.3: Summary of surface roughness measurements of a sample pre-corroded specimen, a sample worn wheel component, and a sample new wheel component.....	88
Table 4.4: Summary of wheel component microstructure pearlite area fractions	96
Table 4.5: Summary of average HRB hardness measurements of five-piece wheel components	99
Table 4.6: Mean and range YS and UTS values of specimens in the as extracted condition	101
Table 4.7: Mean and range YS and UTS values of specimens in the pre-corroded condition	104
Table 4.8: Percent difference in YS and UTS of as-extracted and pre-corroded wheel specimens.....	105
Table 4.9: As-extracted fatigue dataset fit coefficients and statistical analysis values of each fit.....	108
Table 4.10: Percent replication of each as-extracted fatigue dataset	110
Table 4.11: Endurance strengths and lower limit fatigue equations for as-extracted ‘Rim’ and Gutter datasets	113
Table 4.12: Results of statistical analysis of pre-corroded Gutter and Lock Ring fatigue datasets	116
Table 4.13: Failure stresses of pre-corroded dataset fits at 50,000 and 5,000,000 cycles	118
Table 4.14: Failure stresses of as-extracted and pre-corroded ‘Rim’ fits at 50,000 and 5,000,000 cycles.....	120
Table 4.15: Lower confidence band equations of as-extracted and pre-corroded ‘Rim’ datasets.....	122
Table 4.16: Summary of key results from experimental testing discussed throughout Chapter 4.....	128

LIST OF FIGURES

Figure 1.1: Cross-sectional view of a five-piece wheel assembly [7]	2
Figure 2.1: 2007, Massachusetts, USA wheel failure. Black arrow indicates failure region [4].....	9
Figure 2.2: Stages of slip band development during fatigue initiation	14
Figure 2.3: Fatigue crack growth direction [17]	16
Figure 2.4: Fatigue crack growth as a function of crack propagation stage [17].....	16
Figure 2.5: Fatigue surface factors for surface conditions as a function of material UTS [22].....	23
Figure 2.6: Sample S-N plot demonstrating application of confidence bands [34].....	33
Figure 2.7: Summary of ground water conditions in various Pa, USA anthracite mines [40].....	37
Figure 2.8: (a) Chloride, (b) oxygen and (c) sulfate levels in the ground water of a South African gold mine [38].....	38
Figure 2.9: Analysis of two groundwater conditions from a South African gold mine [41]	39
Figure 2.10: Summary of mine water properties for various Canadian mines [39]	41
Figure 2.11: Summary of atmospheric properties for various Canadian mines [39].....	42
Figure 2.12: Microstructure of Q345 for different heat treatments: (a) base metal zone, (c) recrystallized zone, (e) fusion zone, (f) weld metal zone [53].....	49
Figure 2.13: High-cycle fatigue life of a 16Mn steel [55]	50
Figure 2.14: Mass-loss corrosion behaviour of Q345 and other HSLA steels after wet/dry cyclic corrosion testing [57].....	51
Figure 3.1: Accelerated corrosion test setup: (a) all corrosion containers, and (b) top view of one corrosion container	58
Figure 3.2: Roughness profile with equally spaced roughness readings for calculation of R_z	60
Figure 3.3: (a) 100x micrograph of specimen extracted from the flange, (b) binary image of (a) created using ImageJ	62
Figure 3.4: (a) Wilson Rockwell Hardness tester and (b) sample Lock Ring hardness specimen	64
Figure 3.5: Tensile specimen geometry with gauge length, G, of 51.25 mm, fillet radius, R, of 1.68 mm, and gauge diameter of 6.35 mm	65
Figure 3.6: Tensile testing of pre-corrosion tensile specimen equipped with extensometer for strain tracking: (a) before testing), and (b) after testing.....	66

Figure 3.7: (a) Instron illustration of RR Moore system, (b) RR Moore machine in operation, (c) up close image of image machine with pre-corroded specimen, and (d) weights used to adjust specimen stress	68
Figure 3.8: Fatigue specimen geometry and dimensions	69
Figure 3.9: Sample roughness profile of fully ground Rim Base fatigue specimen	69
Figure 4.1: (a) EDS Spectrum of BS band at 500x magnification, (b) BSE image of the sample analyzed	79
Figure 4.2: Percent mass-loss over time of fatigue specimens submerged in 3.5 wt% NaCl solution	82
Figure 4.3: Surface area mass-loss over time of fatigue specimens submerged in 3.5 wt% NaCl solution	83
Figure 4.4: Surface roughness profile of pre-corroded fatigue specimen	86
Figure 4.5: Surface roughness profile of in-service corroded wheel component	86
Figure 4.6: Roughness profile of new painted flange	88
Figure 4.7: Micrographs of Rim Base at (a) 100x, (b) 500x, and in binary at (c) 100x, (d) 500x	89
Figure 4.8: Micrographs of BS Band at (a) 100x, (b) 500x, and in binary at (c) 100x, (d) 500x	90
Figure 4.9: Micrographs of Flange at (a) 100x, (b) 500x, and in binary at (c) 100x, (d) 500x	91
Figure 4.10: Micrographs of Gutter at (a) 100x, (b) 500x, and in binary at (c) 100x, (d) 500x	92
Figure 4.11: Micrographs of Lock Ring at (a) 100x, (b) 500x, and in binary at (c) 100x, (d) 500x	93
Figure 4.12: SEM micrographs of Lock Ring (a) 500x, (b) 1000x, (c) 2000x, and (d) 4000x	95
Figure 4.13: Component HRB hardness as a function of depth	99
Figure 4.14: Yield strength and ultimate tensile strength as a function of pearlite content for as-extracted wheel component tensile testing	102
Figure 4.15: Engineering stress-strain behaviour of as-extracted specimens from the Lock Ring and the Gutter	103
Figure 4.16: As-extracted and pre-corroded stress-strain curves of Lock Ring and Gutter specimens	106
Figure 4.17: High-cycle fatigue behaviour of as-extracted specimens from all wheel components	107
Figure 4.18: As-extracted fatigue data with upper and lower confidence bands	112
Figure 4.19: S-N fatigue behaviour of pre-corroded Lock Ring and Gutter datasets	116

Figure 4.20: S-N curves of as-extracted and pre-corroded 'Rim' fatigue datasets	119
Figure 4.21: Fracture surfaces of low-load Gutter fatigue specimens (a) as-extracted and (b) pre-corroded	124
Figure 4.22: Higher magnification SEM fractographs of low-load Gutter fatigue specimens in the (left) as-extracted and (right) pre-corroded conditions. From top to bottom: (a,b) 100x, (c,d) 500x fatigue initiation zone; (e,f) 100x, (g,h) 500x fatigue failure zone.....	126
Figure 4.23: Fracture surfaces of high-load Gutter fatigue specimens (a) as-extracted and (b) pre-corroded	128

1. INTRODUCTION

1.1. Background

A mining industry is essential for the economic growth and long term prosperity of a country. It promotes expansion of a country's underlying infrastructure, and must grow accordingly. For a mining industry to maintain growth, modern machinery and mining techniques are employed to allow for greater expansion of a mine beneath the earth's surface. With the increasing depth of mines, heavy mining vehicles are exposed to more severe conditions, both environmental, e.g., corrosion, elevated temperature, as well as mechanical loading, e.g., vehicle payload, uneven terrain and side-impact due to narrow mine pathways conditions. In these conditions, components of the mining vehicles have the potential to fail prematurely if proper preventative maintenance procedures are not implemented. Of particular susceptibility to failure are the multi-piece wheels used for mounting of mining vehicle tires [1].

A typical multi-piece wheel, Figure 1.1, is manufactured using high-strength low-alloy (HSLA) structural steel. The design consists of a rim base, a mounting disc, a front flange, a rear flange, a split lock ring, and a bead seat band. Based on the expected function of the wheel (e.g. loading, tire size), certain components are sometimes combined into one forged or machined component. These wheels are used in place of single piece rims when their corresponding tires are too stiff to be mounted, using conventional methods, without becoming damaged [2]. Such is the case for heavy

mining vehicles, which require stiff and durable Off-The-Road (OTR) tires to support their large payloads and to withstand the harsh terrain conditions of a mine.

While the necessity for multi-piece wheels is clear, their use introduces additional safety hazards into the workplace [3], [4]. These hazards are caused by the relatively complex working mechanisms of the wheels, the high pressures used within the tires and the unfavourable environmental and operational conditions associated with underground mining. Thus, extra care and due diligence are taken when dealing with multi-piece wheels by ensuring mining personnel are trained to safely install and handle the wheels, as well to as perform scheduled preventative maintenance. Unfortunately, even with current safety measures, several instances of workplace injuries and fatalities associated with multi-piece wheel failures have been reported [4], [5] [6].

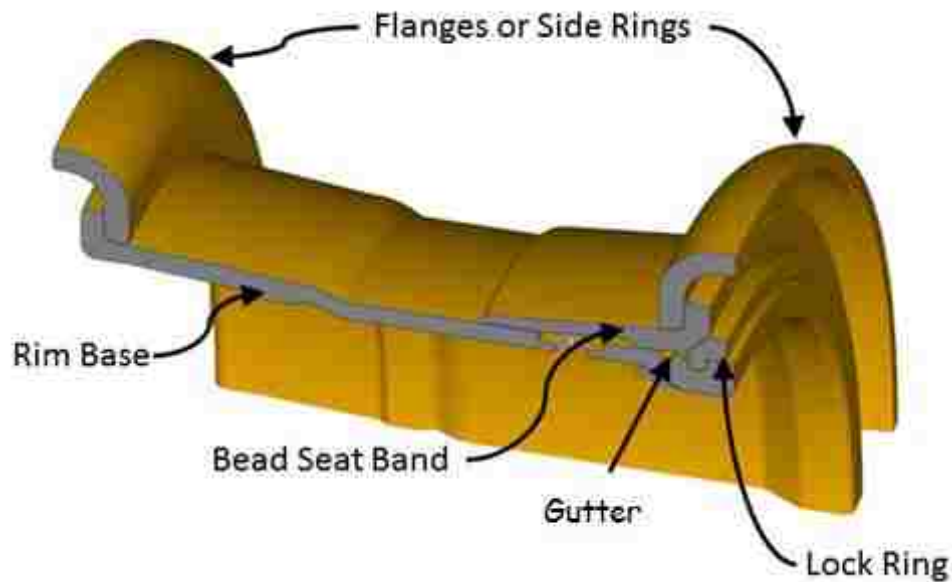


Figure 1.1: Cross-sectional view of a five-piece wheel assembly [7]

Based on available mining wheel failure incident reports, wheel failures can be broadly categorized into two groups: (a) those attributable to human error and (b) those

attributable to mechanical failure of individual wheel components. Human error can be addressed by better safety and handling training; however, mechanical failure indicates that current wheel preventative maintenance procedures are inadequate at addressing wheel failures. The cause for this inadequacy is rooted in the fact that little information is available to accurately estimate the lifespan of multi-piece mining wheels, which experience fatigue, wear, corrosion, fretting, and sudden impact and high cyclic loadings, as noted within incident reports [6], [8], [9] [10] and a mining wheel failure analysis survey [11].

The research presented in this study is part of an on-going project that investigates the failure mechanisms of multi-piece wheel assemblies and develops innovative solutions to improve the safety associated with all facets of multi-piece mining wheels. Specific to this work, the material properties of the structural steel used in the manufacturing of a five-piece wheel are evaluated. Attention is placed on obtaining the fatigue behaviour of the wheel material in the as-extracted and pre-corroded conditions. Material property variations are to be determined between wheel components, which are attributable to microstructural and compositional variances. Data from this study will later be used within the project research group to facilitate prediction of the fatigue life of the five-piece wheel design under investigation.

1.2. Objectives of Study

The primary objective of the present study is to assess the mechanical and material properties of the structural steel used in manufacturing of a five-piece mining wheel. Special emphasis is placed on the fatigue life of the material in the as-extracted and pre-corroded conditions. Explicit research objectives include:

1. Evaluate the mechanical and material properties of the structural steel used in the manufacturing of the components of a five-piece mining wheel to ensure the mechanical properties coincide with minimum strength standards;
2. Note differences in material properties between wheel components and correlate this behaviour with microstructural and compositional variations, where possible; and
3. Quantify the high-cycle fatigue behaviour of the wheel material in the as-extracted and pre-corroded conditions using stress based fatigue testing. Employ appropriate methods of statistical fatigue life analysis to evaluate data.

1.3. Scope of Study

Experimental testing is to be conducted to obtain the mechanical and material properties of the structural steel used in construction of the components of a five-piece mining wheel. Testing examines the behaviour of the material in the as-extracted and artificially pre-corroded states. Test specimens are to be extracted at random from each wheel component under investigation to ensure any variations in component microstructures were accounted for during testing. Artificial corrosion is necessitated because specimen extraction from used rim components would remove all traces of corrosion. Obtaining the fatigue behaviour of the steel in the corroded state is of special interest in this work, based on its reported role in multi-piece wheel failure. Welded areas of the wheel components are assumed to satisfy all relevant quality control standards and further investigation of this topic is beyond the scope of this work.

Artificial corrosion consists of fully submerging test specimens in an aerated saltwater solution and recording mass-loss. Specimens are then to be dried and

periodically re-exposed to the solution until a corrosive film has formed on their surfaces. Surface roughness of the used wheels and artificially corroded specimens is to then be measured to verify that the level of corrosion sufficiently reflects the corrosion wheel components experience during service.

Microstructural and compositional analyses are to be performed on specimens extracted from the new wheels to observe any variations in material behaviour between wheel components. The results are to be cross-referenced with cross-sectional hardness testing and uniaxial tensile testing, when necessary, and based on available specimens. Tensile testing in the corroded state is to be performed to determine the effects of corrosion on the strength and ductility of the material.

Fatigue behaviour of the wheel material in the two conditions under investigation is to be determined through stress-based rotating bending fatigue testing. Testing at various stress amplitudes is to be done at random to reduce environmental bias. A logarithmic regression analysis is to be performed on each data set to generate confidence bands and trends from the fatigue data.

1.4. Organization of Study

Chapter 2 presents a detailed review of topics relevant to the failure and analysis of multi-piece mining wheels. It includes a summary of wheel failure incidents to justify the work being conducted. Sections are included on the fatigue of metals and related statistical analysis procedures, in preparation for the fatigue work undertaken in this study. Discussion on corrosion in the mining workplace and accelerated corrosion testing is presented. Finally, selected works with the structural steel used in fabrication of multi-piece wheels are discussed.

Chapter 3 presents the detailed methodologies and testing procedures employed throughout this study. Included in this chapter are sections on: (a) specimen extraction, (b) compositional analysis (c) accelerated corrosion, (d,e) cross-sectional hardness and surface roughness procedures, (f) optical microscopy and (g) tensile testing. In addition to these basic topics, detailed methodologies regarding fatigue testing are presented. These include the fatigue testing matrix, the type of fatigue testing selected, with justification, as well as a discussion of the statistical methods employed for fatigue data analysis.

Chapter 4 includes all of the results and related discussions from experimental testing. The primary objective of this chapter is to discuss and analyze the experimental fatigue behaviour of the structural steel of the five-piece mining wheel under investigation in the as-extracted and pre-corroded conditions. In addition to fatigue data, data from other experimental mechanical and material tests are presented and discussed. Where appropriate, this data is used to explain differences in wheel material fatigue behaviour.

In Chapter 5, conclusions from the research of this study are presented, as well as recommendations for future research. Details regarding how the data from this work will be implemented to reduce future multi-piece wheel failures are also discussed.

2. LITERATURE REVIEW

The purpose of this literature review is to address key subjects related to this study. Included in section 2.1 is a summary of a select group of reports dealing with mining wheel failures. Sections 2.2 and 2.3 deal with fatigue in metals and relevant means of fatigue data analysis. In section 2.4, corrosion in the mining workplace and a summary of relevant accelerated corrosion testing procedures is discussed. Section 2.5 summarizes relevant works which have involved the structural steel used in the manufacturing of five-piece mining wheels.

2.1. Multi-Piece Mining Wheel Failures

Multi-piece mining wheel incident reports are generated whenever mining personnel experience injuries or fatalities while working with the wheels. Often, these injuries occur from a lack of care by parties involved [10], [12], however, there are also many reports where failures have occurred simply due to failure of a wheel component. Summarized below is a sample of reported wheel failures that were not preventable with current wheel safety practices. The selection comes from over 40 known multi-piece wheel incident reports. It is suspected that a great deal more incidents have occurred worldwide, however, developing nations with prominent mining industries do not always have strong incident reporting standards. Additionally, results of a metallurgical failure analysis of a cracked wheel rim are presented.

2.1.1. Multi-Piece Wheel Failure Incident Reports

In 1998, in Saskatchewan, Canada, the rear wheel from a Toro 35D underground haul truck failed during removal of the wheel. The failure occurred as the service technician was removing the final bolt connecting the wheel assembly to the vehicle axle. During failure, the outer flange was projected away from the wheel with the full force of the pressurized tire, resulting in the death of the technician. An investigation into the incident found that extensive fatigue cracks were present both in the rim and in the outer bolting flange [8].

Documented in 2000, in Ontario, Canada, a worker was critically injured while inflating a multi-piece wheel tire. During inflation, the lock ring became disengaged and was propelled away from the tire into the employee. The worker sustained a broken left arm, broken right hand, and bruise to the left leg. Cause for the failure was not reported [5].

A lock ring was propelled from a three-piece wheel during installation onto an off-the-road vehicle in 2003, in Alaska, USA. The lock ring struck the wheel service worker, ultimately resulting in their death. An investigation into the incident found that the lock ring had experienced severe pitting from corrosion, and had become sprung due to excessive loading. These factors reduced the structural integrity of the ring, preventing it from safely engaging other wheel components. Recommendations from the incident included better wheel inspection schemes and better wheel handling safety training [9].

In 2004, in Saskatchewan, Canada, the tire used on a multi-piece wheel exploded during installation onto a vehicle, resulting in a single fatality. Investigation into the cause of the incident found that the gutter region of the wheel had experienced significant

damage over the course of its service life, attributable to both corrosion and fatigue. The damage to this component meant that the related wheel lock ring could not be properly seated within the gutter region. This issue prevented full engagement of other wheel components, and subsequently caused the sudden loss of tire pressure once the tire was rolled to the mining vehicle for installation [6].

A multi-piece split rim failure occurred while a mechanic was changing the tire of a container handler vehicle (Figure 2.1) in 2007, in Massachusetts, USA. Upon failure, wheel components were propelled away from the vehicle, striking, and fatally injuring, the mechanic. The incident occurred due to a variety of factors, including improper tire handling procedures and mechanical failure of the gutter region of the wheel due to material degradation, resulting in fatigue cracks within the gutter. Recommendations from the incident involved better handling procedures, in addition to more vigorous wheel component structural integrity examinations [4].



Figure 2.1: 2007, Massachusetts, USA wheel failure. Black arrow indicates failure region [4].

Incidents 1 and 2 involved wheel failures where the primary factors were fatigue and corrosion, respectively. Reports 4 and 5 involved wheel failures where both corrosion and fatigue facilitated the premature failure of the wheels. These sample reports are representative of the general trend in wheel failures, when human error is not considered. Thus, obtaining the corrosion and fatigue behaviour of the structural steel used in construction of mining wheels was a primary objective of this study. In incident report 3, no cause for the wheel failure was determined. This report was included in an effort to also highlight the need for a greater knowledge of multi-piece wheel failure mechanisms, and the early signs of their failure.

2.1.2. Failure Analysis of a Cracked Wheel Rim

In a report commissioned by North Shore Industrial Wheel Manufacturer, Bodycote performed a metallurgical failure analysis of a cracked wheel rim [11]. Evaluation incorporated visual and stereomicroscopic examination techniques, scanning electron microscopy (SEM), energy dispersive X-ray spectroscopy (EDS), metallographic examination and microhardness testing. Visual and stereomicroscopic examination revealed cracks located in the gutter region, where the lock ring made contact with the rim. Scanning electron microscopy analysis of locations near the cracks showed signs of rubbing and wear damage. Crack analysis revealed relatively brittle fracture features, including intergranular and cleavage features. Energy dispersive spectroscopy analysis found most of the crack surface to be covered by oxides; however, levels of chloride were also detected.

Microhardness testing was conducted on the core of the wheel rim. Three measurements were taken. The average HRB hardness from the measurements was

found to be 82. Cross-sectional hardness readings were also taken, at depths from 0.03 mm to 2.00 mm from the surface. Hardness measurements near the surface were recorded as 97.8-99.4 HRB. Measurements at a depth of 2.00 mm from the surface found the hardness to be 90.3. Overall, hardness did not vary significantly beyond a depth of 0.4 mm.

Conclusions from the investigation of Bodycote found that the gutter cracks occurred through either corrosion assisted fatigue or stress corrosion cracking. It is stated that even if corrosion was the cause, it would not be feasible to remove chloride from the mining environment. Therefore, the recommendation was made to reduce or eliminate the relative motion between the lock ring and gutter to mitigate wheel failures.

2.2. Fatigue in Metals

Fatigue in metals is characterized as the progressive, localized, damage of a metal subjected to cyclic and/or fluctuating loads [13]. Fatigue failure is the result of fatigue loading conditions that were allowed to persist until failure. These loading conditions are always below the ultimate tensile strength (UTS) of the metal, and often below the yield strength (YS). Because fatigue failures always occur below the UTS, special considerations must be given when designing any structure expected to experience variable loading conditions. The condition of variable loading is exactly the case of a mining vehicle wheel, which, by nature, experiences cyclic fluctuating loads during operation. To correctly address the problem of fatigue associated with the structural steel of mining wheels - a primary objective of this study - a summary of key aspects of fatigue in metals is presented.

2.2.1. Stages of Fatigue

From a mechanical standpoint, the progression of fatigue within a material can generally be divided into three stages: (a) fatigue crack initiation, (b) fatigue crack propagation or growth, and (c) fatigue failure. Similarly, from a materials standpoint, fatigue progression can be divided into four stages: (a) cyclic plastic deformation, (b) fatigue crack initiation, (c) propagation of micro-cracks into macro-cracks, and (d) fatigue failure. The two definitions of fatigue behaviour are roughly equivalent, except that crack initiation in the former definition is further separated into crack initiation and cyclic plastic deformation in the latter definition. Regardless of which progression scheme is followed, the establishment of fatigue stages (notably the crack initiation and progression stages) has allowed for significant advances in engineering design through a better understanding of the mechanisms associated with each stage [13].

Fatigue crack initiation can only take place if the material experiences cyclic plastic deformation. In contrast, most fatigue failures occur at stress levels below the yield strength of the material. This discrepancy is explained by examination of what occurs at the microstructural level of the material during application of a cyclic load. Discussion is first presented for uniaxial loading, and then made for the more general loading conditions seen within industry.

During uniaxial loading, stresses are not evenly distributed within the material. Local defects in the microstructure cause stress concentrations that can exceed the nominal applied stress, resulting in areas of local plasticity. Some common defects include inclusions, high density dislocation areas, and mismatched grain boundaries. If the stress in these regions exceeds the fatigue crack initiation threshold, crack initiation

can occur at these locations. In practice, however, fatigue crack initiation sites are primarily located at the surface [14] of any component experiencing variable loading conditions.

Cyclic loading of most structural components often encompasses some degree of bending in addition to uniaxial loading, generates an uneven macroscopic stress distribution within the material, with the maximum stress being at the surface of the material. Even if this stress is below the yield stress of the material (as is often the case), it still results in a local maximum stress. This stress is augmented through interaction with the surface defects of the component, which acts as stress risers. Typical defects can include nicks, dents, pitting, corrosion, wear, or simply surface roughness caused by the machining process [13]. The net effect can produce stress levels sufficient to cause local plasticity, eventually resulting in fatigue crack initiation.

From a microscopic viewpoint, localized plasticity within a cyclically loaded component also preferentially arises at the component surface due to the absence of adjacent material on the surface, exposed to the testing environment. Since the surface of the material is exposed to half as many adjacent grain boundaries as the remaining microstructure, it is less constrained to motion, allowing for deformation to transpire with more ease, and thus at lower stress levels [15].

Once local deformation takes place on the surface of the material, a slip step is formed. The slip step implies the creation of a new layer of material. The new layer is exposed to the testing environment, and for most materials and testing environments, this instantly causes the formation of a thin oxide layer. The oxide film adheres to the

material, and is not easily removed during reversed slip; thus resulting in some irreversible changes [15].

Over several cycles of slip step generation, slip bands develop. Dislocation gliding takes place along these bands in an effort to minimize energy. Slip and dislocation gliding continues in this way until an obstacle is reached, at which point dislocation pileup occurs. Eventually, with a high enough dislocation density, the obstacle may be overcome through dislocation climb, jog, cross-slip or similar mechanisms [16]. This process repeats itself over the course of many cycles, due to the continued preference of dislocation motion along the low energy slip bands. The result of this activity creates persistent slip bands (PSB), as illustrated in Figure 2.2.

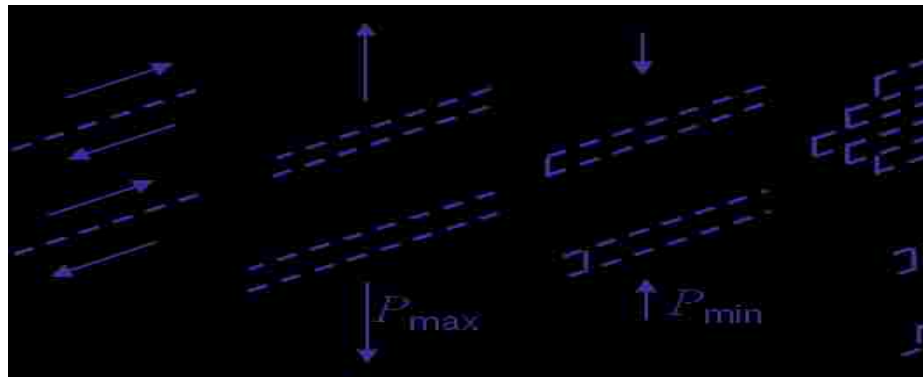


Figure 2.2: Stages of slip band development during fatigue initiation

With continued dislocation motion along the PSBs, dislocation density and interaction increases, resulting in some work hardening and plastic deformation along the PSBs. Parallel slip bands in the material can be formed from this activity, as well as a ladder type slip structure. Over more cycles, PSB dislocations begin to interact with intersecting grain boundaries and free surfaces. Stress concentrations result and slip into adjacent grains occurs. The plastic strain from this repeated process accumulates over

time, eventually overwhelming the surrounding microstructure, and prompting the initiation of fatigue cracks [16].

Following crack initiation, crack propagation takes place. Fatigue behaviour in this stage is primarily controlled by fracture mechanics and bulk material properties, which is contrasted with the initiation stage, in which surface effects dictate fatigue behaviour. Crack propagation is discussed in three stages: (a) micro-cracks, (b) macro-cracks, and (c) fracture.

In the first stage of crack propagation, fatigue micro-cracks move along shear planes, and thus have a tendency to be angled at 45° (Figure 2.3) relative to the surface (in the case of crack initiation at the surface). During this stage, cracks propagate freely until microstructural barriers are encountered (e.g. grain boundaries, inclusions, sufficiently hard material phases). The cracks then lose energy and decelerate if they are able to overcome the crack barrier, or they become arrested if sufficient energy is unavailable to overcome the obstacle. Knowledge of this behaviour has allowed material engineers to prolong the first stage of crack propagation by use of grain refiners within the material, and shot-peening to the material surface [13].

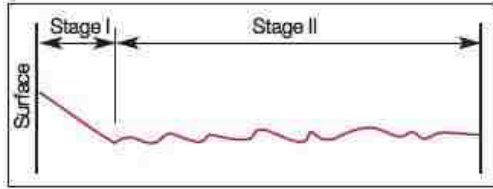


Figure 2.3: Fatigue crack growth direction [17]

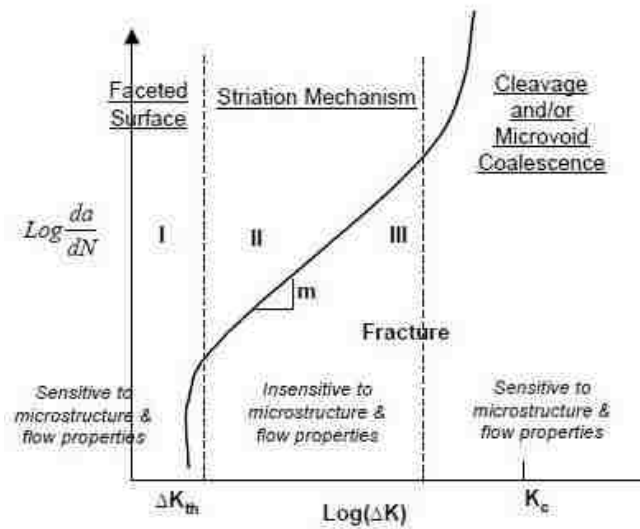


Figure 2.4: Fatigue crack growth as a function of crack propagation stage [17]

In the second stage of crack propagation, prolonged crack growth results in an increase in the stress intensity at the tip of the crack. As a result, cracks begin to deviate from the initial slip bands, and generally move perpendicular to the applied stress. Continued progression of cracks in this stage results in the development of a crack front. Here, the crack tip can be approximated by a single continuous line, and the crack propagation rate can be averaged from individual crack rate values. At this stage, individual micro-cracks may be considered as one continuous macro-crack, governed by the balance between crack driving forces, and the crack growth resistance of the material [17]. The time for a macro-crack to develop is highly sensitive to the material being studied, as would be expected based on the role of the microstructure in crack propagation. Nevertheless, a common trait of macro-crack propagation is the generation of striations within the material; however, this effect does not occur in all materials [17].

In the final stage of fatigue crack growth, crack growth rates are unstable, as the material approaches failure, as illustrated in Figure 2.4. In this regime, the process is comparable to a quasi-static failure, as the crack tip stress intensity is approaching the fracture toughness of the material. Based on material properties and microstructure, loading ratio ($R = \text{min}/\text{max}$ stress), and stress state, the failure is ductile or brittle. The fracture surface after failure can be characterized by two areas: (a) the region in which crack initiation and stable propagation transpired, and (b) the region where final crack propagation occurred, after crack stress levels exceeded the fracture toughness of the material [17].

Duration of the crack initiation and crack propagation stages is strongly governed by, among other factors, the amplitude of the applied stress and the strength of the material. If the stress amplitude is high (above yield), stresses within the material are sufficient for crack propagation; thus, the fatigue life is primarily controlled by crack propagation. Conversely, for lower stress amplitudes (below yield), stresses within the material are low, requiring a greater amount of time to allow for fatigue crack initiation. These two scenarios are referred to as low-cycle and high-cycle fatigue, respectively.

2.2.2. Fatigue Design Approaches

In fatigue design, knowledge of component loading conditions and desired lifespan are essential. Once these parameters have been determined, the appropriate fatigue life prediction scheme can be selected. In the case of infinite life (cycles $>10^6$) component design, the stress-based fatigue prediction scheme can be used. For a component design of finite fatigue life (cycles $<10^3$), the strain-based fatigue prediction scheme must be employed.

The stress-life (S-N), or infinite life, method is the first fatigue prediction scheme to see widespread usage, with its origins dating as far back as the mid 1800's in the prediction of railroad axle failures [13]. The basis of the stress-life method consists of generating S-N diagrams. S-N diagrams are developed by plotting nominal material stress amplitudes (S) against the corresponding number of cycles to material failure (N). The diagram is normally displayed on a log-log plot, with a log-linear line of best fit representing the mean fatigue behaviour of the material. Two central features typically arise from S-N diagrams: (a) a power law relationship between stress and fatigue cycles and (b) a fatigue endurance limit.

The power law relationship is classically observed as a straight line through S-N test data on a log-log plot. This relationship is critical for the design engineer because it allows for the mathematical representation of the material's fatigue behaviour in the high-cycle regime. With S-N test data and knowledge of its power law behaviour, statistical analyses may be made to ensure reliability of the high-cycle stress-life data by taking the lower limit of the mean fatigue behaviour for a desired confidence band.

Certain materials, notably low alloy carbon steels, display what is known as an endurance limit. This means that below a certain stress level, they no longer display signs of fatigue degradation, or, stated otherwise, they have an infinite fatigue life. This behaviour is primarily attributable to a lack of energy for crack initiation to persist into crack growth, due to insufficient stress levels. The endurance limit is dependent on a number of factors, including material surface finish, and therefore cannot be considered a true material property [18]. Furthermore, not all materials exhibit an endurance limit,

however, for design considerations, an endurance limit is sometimes assigned, which is determined from the fatigue strength at 10^8 cycles [18].

The stress-life method makes use of continuum theory, i.e., no cracks, and is generally only applicable to stress amplitudes below the yield strength of a material. Thus, the stress-life method is a high-cycle fatigue methodology ($>10^4$ cycles to failure), in which the total fatigue life of the material is largely associated with the fatigue crack initiation phase. Because of this, the only failure criterion the stress-life method can measure is the cycles to total separation of a material test specimen. Despite these limitations, the stress-life method is still widely used within industry due to its simplicity and the abundance of historically available test data.

The strain-life (ϵ -N), or finite-life, method is a fatigue prediction scheme meant to address the fatigue behaviour of a material for the relatively low cycle regime (approximately 10^2 to 10^6 cycles). Like the S-N approach, the strain-life method assumes a material continuum, and thus, is incompatible with the presence of cracks. Furthermore, the strain-life approach uses strain, instead of stress, as the controlling factor, and can thus be applied to situations involving local plastic deformation. This feature allows for several advantages over the S-N method.

The strain-life method can be used in the evaluation of low-cycle high stress fatigue regimes, by accounting for the work hardening a material experiences during cyclic plastic deformation. Thus, the strain-life approach is well suited for evaluation of notch effects on the fatigue response of materials.

While the strain-life approach is primarily used in the low-cycle fatigue regime, it can also be applied in high-cycle testing (when no material endurance limit exists) with a

marginally higher degree of accuracy relative to the stress-life approach. This is because even in the high-cycle regime, small amounts of cyclic plastic deformation and work hardening occur (as is required for fatigue), which alters the material's response to the application of stress. The result is that the stress-life method may tend to be more conservative in fatigue life estimations [13].

Given that strain is the controlling factor in the strain-life method, and that in the low-cycle fatigue regime the crack-initiation period occupies a lower percentage of the total fatigue life, various failure criteria can be selected for strain-life evaluation. These criteria include separation, percentage maximum load drop for a given strain level, or micro-cracking [13]. Each criterion provides different information on the fatigue response of the material; however, like the S-N approach, they are only applicable within the fatigue crack initiation stage, where material continuum remains valid.

Once fatigue crack initiation is superseded by crack propagation, the stress-life and strain-life approaches can no longer be applied. Instead, linear elastic fracture mechanics (LEFM) must be used. This approach allows for quantification of the stress field at the crack tip of a propagating crack. It is a macroscopic approach and makes use of the bulk properties of the material under investigation. The main goal of this approach is obtaining a material's fatigue crack propagation rates, which may then be used in the design of a damage tolerant component, with a finite fatigue life. For this reason, the LEFM approach is often paired with the strain-life approach, which allows for a complete picture of a material's low-cycle fatigue behaviour [13].

Although the strain-life method can predict low-cycle fatigue behaviour, and outperform the stress-life method in evaluating high-cycle fatigue behaviour (where no

endurance limit exists), it is not without its drawbacks. Primarily, strain-life testing is not as straightforward as the simple load-controlled process of S-N testing. As a result, ϵ -N testing equipment will tend to be more costly and operate at lower maximum frequencies, due to the need for additional equipment instrumentation over S-N testing. Thus, strain-life testing can be cost prohibitive and unnecessary if only the high-cycle fatigue behaviour of the material is required. For low-cycle fatigue testing, the strain-life method and related testing equipment must be employed.

2.2.3. Fatigue Life Factors

The fatigue behaviour of a material is a dynamic property that is influenced by many factors. Therefore, the fatigue behaviour of a material cannot be accurately used for design without knowledge of the fatigue testing conditions [13]. Likewise, a structural component cannot be designed without knowledge of its expected working conditions, and how these and other various factors influence the component's fatigue life. To proceed with the investigation on the fatigue behaviour of the structural steel of a multi-piece mining wheel, understanding of factors that would influence its fatigue behaviour was necessary. A discussion of the most relevant factors and testing methods (where appropriate) is presented below.

Loading Type: The type of loading a component experiences relative to laboratory testing can influence the material's endurance limit. In the case of a material tested under pure cyclic bending, the material's endurance limit in practice may be reduced by 15% for axial loading or by 41% for pure torsion [19]. Stress ratio and mean applied stress are also known to influence a material's fatigue behaviour; however, the exact effects are

material dependent. Generally, fully reversed loading ($R=-1$) is considered to be a more severe loading condition [20].

Component Geometry: The presence of notches on a fatigue specimen or in a component design will significantly reduce its high-cycle fatigue life due to the localized stress concentration [13]. Additionally, component size has been empirically found to reduce the endurance limit, presumably due to the higher probability of imperfections in a larger component relative to a test specimen [19].

Temperature: Decreases in temperature relative to the ambient prolong the period in which fatigue is restricted to the crack initiation stage [13]. For low loading conditions, this increases the total fatigue life for a given stress amplitude. At temperatures significantly above the ambient, crack nucleation in slip bands may be facilitated at the grain boundaries. At high temperatures, the effects of creep on fatigue life are also to be considered.

Surface Condition: During discussion of fatigue crack initiation, it was found that the surface is the primary initiation point for material fatigue. Therefore, surface effects have a large influence on high-cycle fatigue behaviour. Surface roughness always reduces the fatigue life of a material relative to the polished condition. An extreme measure of this compares the surface finish of a lathe-formed component to a ground and polished component. The median fatigue life in cycles of the lathe-formed specimens decreased by approximately a factor of 10 relative to the ground and polished specimens [21]. It should, however, be noted that in addition to surface roughness, residual stress effects were also in play. In general, residual compressive stresses improve fatigue life by increasing the minimum required stress for crack initiation to occur. Conversely,

residual tensile stresses promote crack initiation. The high-cycle fatigue life of a material can also be improved through microstructural and chemical surface treatments that inhibit crack nucleation (e.g. surface quenching, protective coatings) [13]. Figure 2.5 illustrates general decreases in fatigue life for various surface conditions.

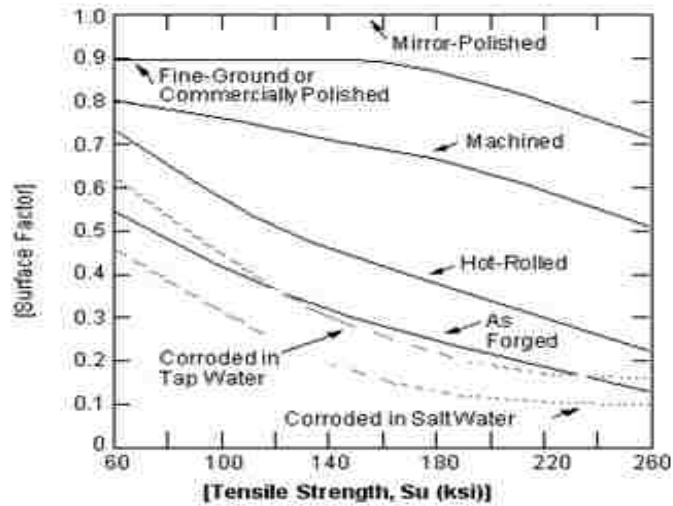


Figure 2.5: Fatigue surface factors for surface conditions as a function of material UTS [22]

Environment: Environmental effects play a large role in fatigue initiation. Generally, a component tested in vacuum exhibits superior high-cycle fatigue behaviour relative to a component tested in the ambient [13]. This behaviour is attributable to the presence of oxygen, which facilitates crack initiation, as discussed in section 2.1; however, the effects of the ambient are normally not considered in fatigue design since most fatigue testing is performed in ambient conditions, and not in a vacuum. While the ambient is not considered in fatigue design, the effects of a corrosive environment must be considered.

The effects of corrosion on fatigue have been investigated extensively for various ferrous and non-ferrous alloys. Common testing methods include cyclic stress/strain

testing in a corrosive chamber and cyclic stress/strain testing of pre-corroded specimens. Fatigue testing in an environmental/corrosive chamber is typically done to replicate highly corrosive service conditions. It promotes the synergistic effects associated with the two processes, and greatly reduces fatigue life. This is especially true for high-cycle low frequency testing, where the specimen is exposed to the corrosive environment over a prolonged period of time.

Pre-corrosion testing is a less severe form of fatigue corrosion testing. Like corrosion chamber testing, it seeks to replicate service conditions; however, the mechanisms of fatigue and corrosion do not interact strongly with this testing scheme. Instead, fatigue specimens are first subjected to corrosion, which may influence surface topology, and generate some degree of microcracking. Then, the specimens are subjected to fatigue loading until failure (or run-out). This type of testing is best employed in conditions where fatigue is a primary failure mechanism, with corrosion playing a small role in overall failure. It is also well suited for full-scale component fatigue testing, where the components have been exposed to corrosion during their service life. Finally, it provides a good first step in corrosion fatigue characterization, since it is relatively simple to implement in comparison to chamber testing and allows for the separate evaluation of a material's corrosion behaviour and resulting fatigue behaviour [23], [24], [25].

Microstructure: Microstructural effects play a large role in the fatigue crack initiation and crack propagation resistance of steels. In the work of Kurita et al. [26], the effect of strengthening mechanisms on ferrite-pearlite steels with similar YS and UTS values was investigated. Strengthening mechanisms investigated were: solid solution,

precipitation, increased dislocation density, grain refinement, and increased pearlite volume fraction. Results found that the high-cycle fatigue behaviour of the steels was governed by crack initiation in the ferrite matrix. Therefore, strengthening mechanisms which improved YS and UTS, but did not strengthen the ferrite matrix (dislocation density, grain refinement, pearlite volume fraction), were reported to have little effect on the high-cycle fatigue life. Conversely, solid solution strengthening and precipitation hardening, which improve the strength of the ferrite matrix, were reported to improve the high-cycle fatigue life.

Sankaran et al. [27] investigated the low and medium cycle fatigue and tensile behaviour of medium carbon steels with differing microstructures (air cooling [AC], quench and temper [QT], and two-step cooling and annealing following forging [TSCA]). It was found that the QT and TSCA steels demonstrated markedly improved YS and UTS over the air cooled steel. Further, the low-cycle fatigue behaviour, where plasticity is significant, for both QT and TSCA steels, was improved over the AC steel. This behaviour is attributable to the improved bulk material properties of the former two steels, which is critical in low-cycle fatigue, where crack propagation dominates. In the medium cycle fatigue testing ($<3 \times 10^5$ cycles), all steels demonstrated similar behaviour. This was attributable to the presence of ferrite in all microstructures.

Investigations similar to those previously discussed are also documented in references [28] and [29]. In the former, it was found that if a ferrite-pearlite microstructure was replaced with a primarily bainitic microstructure, the high-cycle fatigue life of the steels investigated was improved. In the latter work, the low cycle

fatigue crack propagation resistance of a low carbon steel was improved by a fine dispersal of bainite along prior austenite grain boundaries, as opposed to pearlite.

2.3. Statistical Analysis of Fatigue Data

In fatigue testing, there is always scatter in the acquired data. This scatter is generally caused by the cumulative effects of various factors. Some common factors include the testing environment, specimen geometry, and specimen loading conditions [30]. Scatter associated with these factors can generally be minimized through regulation of the testing environment, regular calibration of the testing equipment, and careful preparation of testing specimens. Other factors associated with fatigue data scatter include specimen surface finish and microstructure [30]. These factors are much more difficult to control.

In the case of specimen surface finish, even with a vigorous polishing regime, surface roughness varies between specimens. Since it would be impractical to measure the roughness of each specimen, especially for large datasets, some variance in surface conditions is generally accepted. Likewise, for fatigue scatter associated with material microstructure, little can be done beyond extracting all specimens from the same material, with the same heat treatment, at the same extraction depth, and so some scatter in material microstructure is accepted. In fact, while surface effects are minimized when practical, often, variances in microstructure will be encouraged, to an extent [31]. This is especially true in the fatigue testing of structural components. The reasoning behind this philosophy is that it would be more prudent to have a fatigue data set with more scatter that encompasses the entire family of microstructures within a component, than to have a dataset with no scatter that may not accurately reflect fatigue behaviour. Of course, this

approach is limited to microstructures with similar effects on fatigue, and could not be usefully applied to significantly different microstructures (e.g. pearlite versus martensite in steel).

Given that scatter in fatigue data is both expected, and sometimes encouraged, it is critical that appropriate statistical tools be used during evaluation of the data. Therefore, a brief overview of statistical methods of fatigue data analysis is presented below. Focus is made primarily on the regression analysis of fatigue data, and generating appropriate confidence bands. Furthermore, discussion is limited to analysis of fatigue data associated with specimen failure. Only S-N analysis is discussed, however, general procedures are equally applicable to ϵ -N datasets. Evaluation of fatigue run-out (specimens that do not fail) is not addressed and was beyond the scope of this study. All information presented below originates from references [30], [31], [32], [33] unless otherwise stated.

2.3.1. Testing and Data Sampling

Grouping and randomization of fatigue test samples are essential features of a well-planned fatigue test program. Randomization ensures that variability of testing conditions (e.g. humidity) is spread among all test data, ensuring no bias in datasets is developed. Grouping ensures that in the event of a testing equipment malfunction, a small subset of fatigue specimens over a range of conditions are affected, as opposed to all specimens for one specific testing condition. This is important if one is performing fatigue testing on various materials of different expected fatigue behaviour, or if a limited number of fatigue specimens are available.

The validity of a fatigue analysis is largely dependent on the data sampling size, relative to the number of loading conditions. ASTM E739 offers guidance for the minimum number of S-N fatigue data points that should be acquired for statistical analysis, based on the type of fatigue testing being performed. The recommendations assume the data are based on random sampling, and that no run-out data points are included. This is summarized in Table 2.1.

In addition to the minimum number of fatigue test specimens, the ASTM guideline offers minimum percent replication values. The percent replication is calculated using Equation (2.1), where l is the number of loading conditions, n is the total number of test specimens, and R is the percent replication. For example, under the design allowable condition, a minimum of 12 specimens is required, which would allow for 6 loading conditions if the minimum of 50% replication is desired. For the reliability criterion, with a minimum of 12 specimens, only 3 loading conditions would be possible to achieve a minimum percent replication of 75%.

$$R = 100 \times \left[1 - \frac{l}{n} \right] \quad (2.1)$$

Table 2.1 ASTM E739 fatigue test sampling recommendations

Type of Test	Minimum Number of Specimens	Minimum Percent Replication
Preliminary & Exploratory	6 to 12	17 to 33
Research and Development	6 to 12	33 to 50
Design Allowable	12 to 24	50 to 75
Reliability	12 to 24	75 to 88

2.3.2. Curve Fitting

In S-N fatigue curve fitting, a linear fit of the form of Equation (2.2) is typically applied. In Equation (2.2), X is the independent variable, Y is the dependent variable, m is the slope of the linear fit, and A is the intercept. During analysis, the stress is taken as the independent variable, and the cycles to failure is taken as the dependent variable. This is in contrast to a typical S-N plot, which presents the stress as the dependent variable.

$$Y = A + mX \quad (2.2)$$

Equation (2.2) cannot be directly applied to raw S-N data. First, the data must be linearized. Fatigue data typically demonstrates a logarithmic relationship over certain stress ranges. Therefore, to utilize Equation (2.2), the cycles to failure, N , are commonly transformed using a logarithmic function. When this approach is utilized, the S-N data is said to be log-linear. If the stress values, S , are also transformed logarithmically, the S-N data is said to have a log-log relationship. The type of transformation applied to a fatigue dataset for linearization should be performed based on a visual evaluation of the plotted data. This also helps in determining the range in which the fit is applicable.

Once the fatigue data has been linearized, a curve fitting technique capable of generating a best-fit straight line should be selected. Linear regression analysis using the least-squares method is a good example of an approach that works well for this purpose. Equation (2.3) and Equation (2.4) may be used for calculating the sample population values of the intercept (\hat{A}) and the slope (\hat{m}), respectively. In these equations, \bar{X} and \bar{Y} represent the mean values of the independent and dependent test data, respectively. For

fatigue testing, this corresponds to the applied stress levels, and the cycles to failure. These equations are recommended by ASTM E739 and are based on the method of least-squares.

$$\hat{A} = \bar{Y} - \hat{m}\bar{X} \quad (2.3)$$

$$\hat{m} = \frac{\sum_{i=1}^n (X_i - \bar{X})(Y_i - \bar{Y})}{\sum_{i=1}^n (X_i - \bar{X})^2} \quad (2.4)$$

Upon completion of the least-squares regression analysis, care should be taken to ensure that the calculated fit is statistically relevant. Simple methods of evaluating the legitimacy and accuracy of a fit include performing an F-test and calculating the R^2 value. Additionally, a t-test of the fit's slope and intercept can be performed. Before each of statistical tests is described, several key definitions relevant to their understanding are presented.

The regression sum of squares (SSR) (Equation (2.5)) is the sum of the squares of the deviations of predicted values relative to the mean of the test data. It represents the explainable variance associated with a fit. The residual sum of squares (SSE) (Equation (2.6)) is the sum of squares of the deviations of predicted values from test values. It represents the unexplainable variance associated with a fit, and is also commonly known as error sum of squares. The total sum of squares (SST) is the sum of SSR and SSE and represents the total variance associated with a fit. The standard error of the dataset is denoted as S_{YX} , and is used in the calculation of the standard error (deviation) of the slope and intercept. Equation (2.7) shows the S_{YX} in terms of the SSE and the degrees of freedom (denominator; $n =$ sample size).

$$SSR = \sum_{i=1}^n (\hat{Y}_i - \bar{Y})^2 \quad (2.5)$$

$$SSE = \sum_{i=1}^n (Y_i - \hat{Y}_i)^2 \quad (2.6)$$

$$S_{YX} = \sqrt{\frac{SSE}{n-2}} \quad (2.7)$$

The F-test is a measure of a regression fit's significance. In the test, a null hypothesis is presented which states that all regression coefficients are insignificant (i.e. $= 0$). The alternate hypothesis states that at least one coefficient is significant (i.e. $\neq 0$). Evaluation is performed by calculating the observed F value. Equation (2.8) is the F-value formula for simple linear regression. The observed F value must exceed the critical F value for the alternate hypothesis to be valid. Critical F values are widely available for a range of degrees of freedom and confidence levels. A 95% confidence interval is commonly used in S-N fatigue data analysis.

The R^2 value (Equation (2.9)), or the coefficient of determination, is a measure of how well the regression analysis fits the dataset. It can be thought of as the ratio of the explained variation of the fit, and the total variation of the fit. Mathematically, it is described as ratio of the SSR and SST (SSR + SSE). Therefore, as the SSE is minimized (dependent on testing conditions), the R^2 value approaches unity, indicating a perfect fit between the curve and test data.

The T-test is similar in nature to the F-test; however, instead of assessing the significance of the entire fit, the T-test evaluates the significance of individual

coefficients. Thus, the null hypothesis of the T-test is that a coefficient (slope, intercept) is insignificant, while the alternate hypothesis is that the coefficient is significant (different from zero). Equations (2.10) and (2.11) provide the calculation schemes for the observed t-value of the slope and the intercept, respectively. If the observed t-value is greater than the critical t-value (easily accessible from t-tables), the coefficient under investigation is deemed significant.

$$F = \frac{SSR}{SSE/(n-1)} \quad (2.8)$$

$$R^2 = \frac{SSR}{SSR + SSE} \quad (2.9)$$

$$S_{\hat{m}}^2 = \frac{S_{YX}^2}{\sum_{i=1}^n (X_i - \bar{X})^2} \quad (2.10)$$

$$t_{obs, \hat{m}} = \hat{m} / S_{\hat{m}}^2$$

$$S_{\hat{A}}^2 = \frac{S_{YX}^2 \sum_{i=1}^n X_i^2}{n \sum_{i=1}^n (X_i - \bar{X})^2} \quad (2.11)$$

$$t_{obs, \hat{A}} = \hat{A} / S_{\hat{A}}^2$$

2.3.3. Confidence Bands

In fatigue data analysis, confidence bands are often used to graphically represent the uncertainty associated with the regression fit of a fatigue dataset (Figure 2.6). On an S-N curve, an upper band and a lower band are plotted about the fit. The area encompassed by these two bands represents the expected upper and lower limits of the fatigue behaviour of the material for a desired confidence interval (typically 95%).

Therefore, in fatigue design, the lower confidence band of a fatigue fit should always be used as the bare minimum in fatigue life calculations.

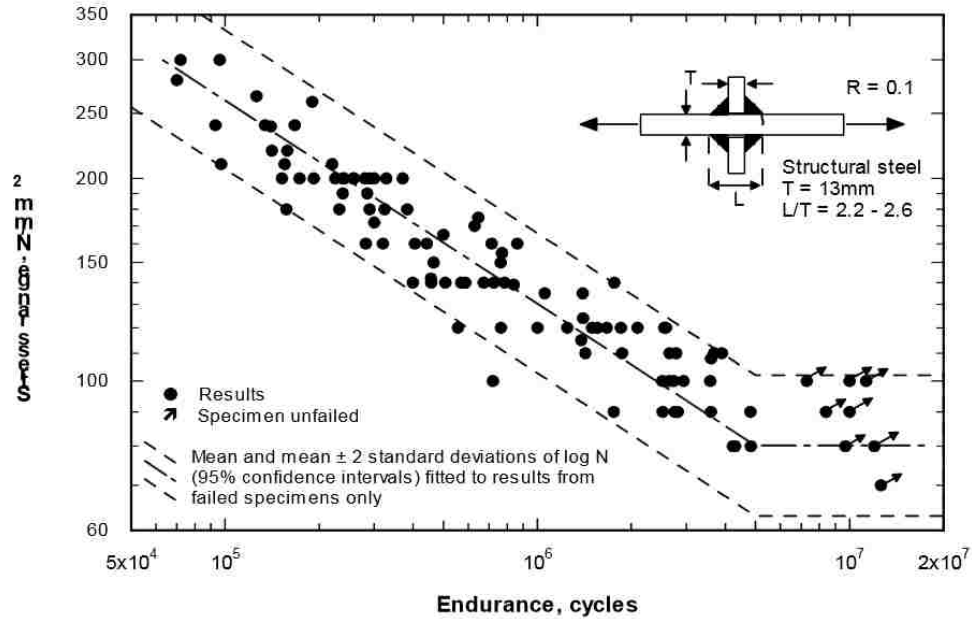


Figure 2.6: Sample S-N plot demonstrating application of confidence bands [34]

Equation (2.12) is used to calculate the upper and lower confidence bands for the regression fit of an S-N dataset. If a greater degree of certainty is desired, Equation (2.13) may also be used. This equation functions very similar to Equation (2.12), however, it calculates the uncertainty bands associated with a single response from a selected loading condition, instead of the uncertainty associated with the overall response of the fit over all loading conditions. A modified version of Equation (2.13) was used in [34], where the stress term within the root was removed. The purpose was to generate uncertainty bands parallel to the regression fit, which would be more easily applicable in fatigue design (Figure 2.6). The decrease in uncertainty from removing the stress term was reported to be mostly negligible, except near stress conditions distant from the mean

stress tested. In both equations, t_{crit} is the critical t value, discussed in 2.3.2, S_{YX} is the standard error of the dataset, n is the total number of data points, and X is the stress.

$$Cl = fit \pm t_{crit} S_{YX} \sqrt{\left[\frac{1}{n} + \frac{(X_i - \bar{X})^2}{\sum_{i=1}^n (X_i - \bar{X})^2} \right]} \quad (2.12)$$

$$Cl = fit \pm t_{crit} S_{YX} \sqrt{\left[1 + \frac{1}{n} + \frac{(X_i - \bar{X})^2}{\sum_{i=1}^n (X_i - \bar{X})^2} \right]} \quad (2.13)$$

2.4. Corrosion Testing of Steels

Corrosion in metals, notably steels, has been shown to cost as much as \$300 billion dollars annually in the U.S. alone [35]. This material degradation mechanism is often the life limiting factor for many in-service structural components. Worst still, corrosion assisted failures often occur without warning, putting the safety of those nearby in danger [35].

To counter the effects of corrosion, several factors must be considered. These include operating conditions, expected loading and desired component lifetime [35]. Once these factors have been determined, initial design and alloy selection can be completed. From there, corrosion testing should be conducted if the environmental conditions are known (or unknown) to negatively interact with the selected alloy under the anticipated loads.

Corrosion testing under expected service conditions can often exceed the time allocated to component design. This is especially true for components with long service lives and, consequently, longer exposure times to corrosion. Therefore, accelerated

corrosion testing is often implemented as a means of evaluating a component's resistance to corrosion. Under the right conditions, this type of testing can yield data beneficial in the selection and evaluation of a corrosion resistant material [35].

Generally, accelerated corrosion testing is used for qualitative assessment of a material's capacity to handle corrosive media. For component testing, if several tests are performed and correlated with actual service lives, the data can be used in a more quantitative way to estimate the effects of corrosion on future components. In this latter approach, standardized testing is often used, for which there exists a wide selection of standards to implement.

In most standards, the mechanism of corrosion should not change between accelerated corrosion testing, and in service corrosion. For example, use of a bolt and test specimen during corrosion testing may create a galvanic couple, which can lead to inaccurate results. ASM [36] broadly classifies corrosion into five categories to facilitate development of corrosion testing schemes: general corrosion (e.g. atmospheric), localized corrosion (e.g. pitting), metallurgically influenced corrosion (e.g. intergranular), mechanically assisted degradation (e.g. fretting corrosion) and environmentally induced cracking (stress-corrosion cracking).

To facilitate the corrosion testing of this study, a summary of data from the open literature on atmospheric and ground water corrosion in the mining industry is presented. Additionally, a review of several common accelerated corrosion standards is completed.

2.4.1. Corrosion in the Mining Environment

Atmospheric and ground water corrosion within the mining industry is a common issue for the longevity of structural and non-structural components. While corrosion is cited as a cause in failure analyses of different mining components (e.g. support systems, bolts, and mining wheels), it is not often given strong consideration during the design stage [37]. Instead, application and reapplication of superficial coatings (paint, galvanization) is the preferred route, if corrosion is addressed at all [37]. This approach can have varying degrees of effectiveness in mitigating corrosion assisted failures. For components that experience wear and relative motion, superficial coatings offer little benefit after a short time in service. Conversely, components exposed to stagnant conditions may be completely protected from corrosion, if strong preventative maintenance schedules are implemented and followed [37].

To properly assess the impact of atmospheric and ground water corrosion within a mining environment, certain factors must be known. These include humidity, temperature and ground water ion content, among other factors [38], [39]. Knowledge of these conditions can improve the reliability of data acquired from accelerated corrosion testing of mining components by ensuring testing closely emulates the in service corrosion mechanisms. Unfortunately, these factors vary widely between different mines, and are affected by geographic location, mine depth, mined material and processing conditions, among other factors. This makes developing an accelerated corrosion testing scheme difficult for multi-piece wheels, which are used in various types of mines. To circumvent this issue, various studies addressing the corrosive conditions of

a mining environment have been reviewed and summarized below. Key corrosion variables from each study are summarized in Appendix A.

The corrosive and erosive effects of acid mine waters on metals and alloys for pumping equipment and draining facilities was investigated by Ash et al [40]. Acid mine waters were sampled from various anthracite (coal variant) mines in Pennsylvania, USA. The pH, alkalinity as CaCO_3^{-3} , and total acidity as $\text{H}_2\text{SO}_4^{-3}$, were reported, among other factors for mine-pump and drainage-tunnel discharges (Figure 2.7). Average pH, alkalinity as CaCO_3^{-3} , and acidity as $\text{H}_2\text{SO}_4^{-3}$ across all mines were reported as 3.0, 6.6 ppm, and 552 ppm, respectively.

Mine-pump and drainage-tunnel discharges											
Field	Volume of water, g. p. m.	Average pH	Weight of water, short tons per day	Load							
				Alkalinity as CaCO_3^{-2}		Alkalinity as CaCO_3^{-3}		Free acidity as $\text{H}_2\text{SO}_4^{-2}$		Total acidity as $\text{H}_2\text{SO}_4^{-3}$	
				P.p.m.	Short tons per day	P.p.m.	Short tons per day	P.p.m.	Short tons per day	P.p.m.	Short tons per day
Northern.....	137, 867	3. 1	827, 204	7	5. 56	5	4. 50	197	162. 68	458	378. 69
Lackawanna Basin.....	67, 421	3. 2	404, 525	0	. 02			174	70. 41	439	177. 47
Eastern Middle.....	45, 822	3. 1	274, 937					464	127. 62	693	190. 52
Western Middle.....	54, 210	2. 9	325, 256	11	3. 71	7	2. 39	258	83. 78	694	225. 77
Southern.....	63, 387	3. 0	380, 322	13	4. 88	9	3. 24	187	71. 21	392	149. 02
All fields.....	301, 286	3. 0	1, 807, 719	8	14. 15	6	10. 13	246	445. 29	522	944. 00
Northern, Western Middle, and Southern.....	255, 464	3. 0	1, 532, 782	9	14. 15	7	10. 13	207	317. 67	492	753. 48

Figure 2.7: Summary of ground water conditions in various Pa, USA anthracite mines [40]

In the work of Higginson and White [38], the corrosivity of water in a South African gold mine was examined. Factors including pH level, total dissolved solids, chloride and sulfate levels, and concentration of dissolved oxygen were quantified (Figure 2.8). Certain factors were then correlated with corrosion rates, measured in

mm/year of a mild steel. Results found that above a pH level of 5, the single greatest factor affecting the corrosion rate of the mild steel was dissolved oxygen content, with higher levels increasing corrosion rates. For pH levels below 5, corrosion rates were primarily dictated by the pH level, with a negative correlation between corrosion rate and water pH level.

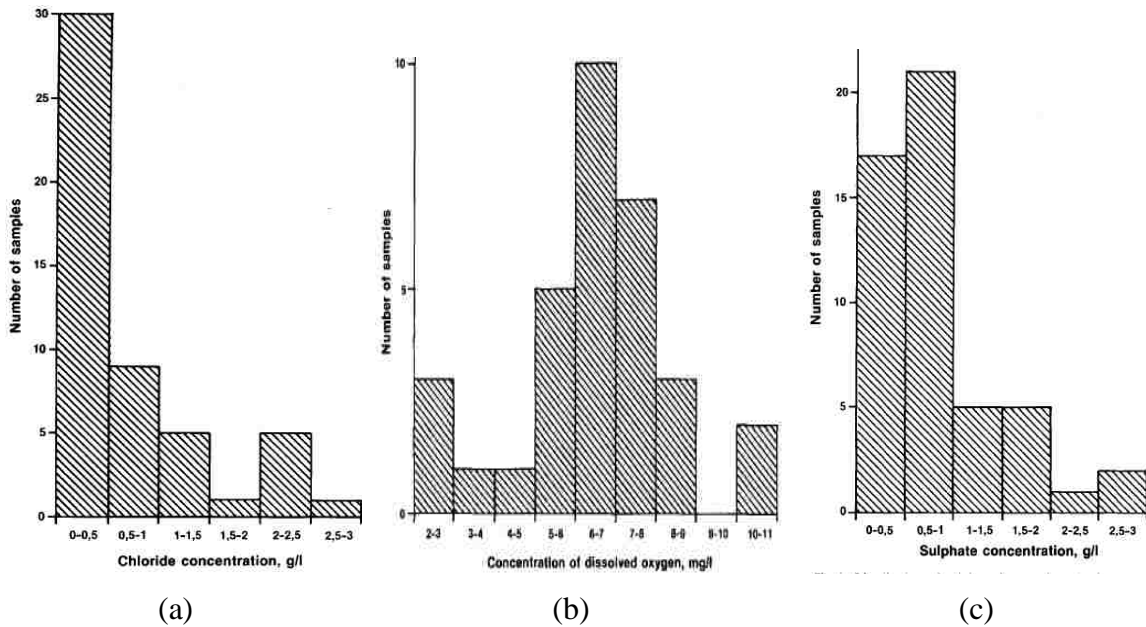


Figure 2.8: (a) Chloride, (b) oxygen and (c) sulfate levels in the ground water of a South African gold mine [38]

Nana et al. [41] investigated the environmentally assisted cracking of a martensitic stainless steel used in South African gold mines. The stainless steel was a type 431 plate steel. Specimens included pre-cracked compact tension specimens, and C ring specimens, hardened to 44-46 HRC and 34 HRC, respectively. Corrosion was induced in laboratory settings based on mine water conditions extracted from the mine. Two water conditions were used for testing, with pH levels of 6.5 and 2.7, respectively (Figure 2.9). The higher pH water contained 4600 ppm total dissolved solids, 1250 ppm chloride, and 1075 ppm sulfate. The lower pH water contained 3800 ppm total dissolved

solids, 28 ppm chloride, and 1829 ppm sulfate. The pre-cracked specimens were tested under constant load and exposure to both corrosive waters until failure occurred. The C-ring specimens were tested in-situ under constant nominal stresses up to $720 \text{ MN}\cdot\text{m}^{-2}$ in stagnant and running water conditions similar to those of the higher pH water. Results from pre-cracked compact testing found the stainless steel was much more likely to fail in the lower pH level, with a minimum failure of 0.5 hours when the stress-intensity in the crack was $32 \text{ MN}\cdot\text{m}^{-3/2}$. Pre-cracked specimens loaded in the higher pH water had a significantly higher average life, with a minimum failure time of 35 hours under a stress intensity of $45 \text{ MN}\cdot\text{m}^{-3/2}$, and roughly half of all specimens not failing after 1000 hours of testing. The C-ring specimens had not yet failed after 740 days of testing. Overall, it was concluded that high hardness levels were detrimental for the corrosion resistance of the stainless steel tested. Furthermore, it was found that low pH sulfate solutions can more easily corroded the stainless steel tested; however, even the higher pH high chloride solution had the capacity to cause corrosion assisted failure.

Condition	Mine water		In situ environments	
	B	C	OFS mine	FWR mine
	pH	6.5	2.7	5.1
Total dissolved solids, ppm	4600	3800
Total suspended solids, ppm	45	76
Ca hardness, ppm CaCO_3	730	561
Mg hardness, ppm CaCO_3	275	1440
Cl^- , ppm	1250	28	1828	100
SO_4^{2-} , ppm	1075	1829	1376	461
Fe, ppm	2.5	37
Conductivity, mS m^{-1}	640	350	775	140

Figure 2.9: Analysis of two groundwater conditions from a South African gold mine [41]

In reference [42], a summary of typical corrosive conditions in a deep level South African gold mine is presented. It is stated that chloride levels can vary between 200-800 mg·L⁻¹ and can be as high as 2500 mg·L⁻¹. Sulfate levels were found to be between 50-200 mg·L⁻¹, with values as high as 600 mg·L⁻¹. Hardness levels, expressed in calcium carbonate, varied between 700 and 500 mg·L⁻¹. At depths of 1000-3000 m, ambient temperatures were recorded between 30-45°C, with the relative humidity varying between 75-95%. Abrasion of mining components and structures was noted as a common occurrence that has synergistic effects with corrosion.

Singh [43] determined the mass-loss corrosion rates of a mild steel submerged in the mine waters of two Indian coal mines. Several water samples across the two mines were acquired to evaluate the variability of the chemical composition of the mine waters and how it affects corrosion rates. Steel plate specimens were immersed in the stagnant mine waters for 15 days for near neutral waters and for one day for highly acidic waters to evaluate their mass-loss due to corrosion. The approximate average chemical composition of the neutral waters contained approximately 900 ppm dissolved solids, 250 ppm sulfate, and 40 ppm chloride, with an average pH of 7.8. This water resulted in an approximate average corrosion rate of 0.21 mg·m⁻²·day⁻¹. The approximate average chemical composition of the highly acidic waters contained 2500 ppm sulfate, and 30 ppm chloride, with an average pH of 2.9. This water resulted in an approximate average corrosion rate of 10.9 g·m⁻²·day⁻¹.

In the work of Hadjigeorgiou et al. [39], the corrosion conditions of various Canadian mines from historical data and in-situ testing were presented to evaluate the performance of mining support systems. From historical data, it was reported that

Swellex bolts in low to moderate and moderate to high corrosion environments had corrosion rates of 0.04 mm/year to 0.07 mm/year and 0.15 mm/year to 0.70 mm/year, respectively. If these bolts were made of a steel alloy, as they often are, this would correspond to average corrosion rates of $1.18 \text{ g}\cdot\text{m}^{-2}\cdot\text{day}^{-1}$ and $9.15 \text{ g}\cdot\text{m}^{-2}\cdot\text{day}^{-1}$, respectively. For in-situ testing, measurements were taken of the mine waters and mine atmospheres of gold and niobium mines. Water measurements included pH, chemical composition, temperature, dissolved oxygen and salinity. Some atmospheric measurements included testing depth, dry temperature, and relative humidity. Data on the water measurements is summarized in Figure 2.10, and data on the atmospheric measurements is summarized in Figure 2.11, both extracted from [39]. Additionally, the maximum chloride and sulfate levels within the tested mine waters are summarized in Appendix A. Evaluation of mine support systems at excavation ages ranging from 3 to 180 months found that the degree of corrosion ranged from “localised staining” to “advanced to very advanced”. All observations were visual in nature.

PARAMETERS	NIOBEC			MOUSKA			GÉANT-DORMANT		DOYON			LARONDE	
	1150-GA-17	1150 ventilation 1-E	1450-GA-34-PS44	Level 8- access shaft 2	Level 8-drilling bay	Level 11- drilling west	60-8-275-PS105	60-3-370-PS134	8-2(8-3)- principal ventilation access	9-4-access-2.08	10-0- access -1.33	158-20-57	203-20-52
Temperature (°C)	13.5°	15.0°	14.2°	9.7°	9.0°	11.6°	8.0°	7.9°	15.7°	14.6°	16.8°	27.0°	28.4°
pH	7.8	8.0	7.7	7.6	7.6	6.9	7.2	7.1	2.9	4.0	5.9	3.4	4.4
Dissolved Oxygen (ppm)	7.4	8.8	8.7	8.2	9.0	5.9	11.2	9.3	8.0	8.8	9.0	6.5	7.4
Salinity (ppt)	6.7	-	10.1	0.2	0.6	4.9	2.2	1.0	3.5	8.2	1.9	17.9	5.0
Conductivity (µS)	9150	6530	13630	282	860	6540	2743	1301	5240	11250	3045	30800	9650

Figure 2.10: Summary of mine water properties for various Canadian mines [39]

LOCATION	NIOBEC			MOUSKA			GÉANT-DORMANT			DOYON			LARONDE		
	1150-GA-17	1150 ventilation 1-E	1450-GA-34-PS44	Level 8- access shaft 2	Level 8- drilling bay -6450E	Level 11- drilling bay West	60-30-292-PS43	60-8-275-PS105	60-3-370-PS134	8-2(8-3)- principal ventilation access	9-4-access-2.08	10-0-access-1.33	149-20 West	158-20-57	203-20-52
Depth (m)	350	350	442	435	435	610	605	605	605	460	500	635	1490	1580	2030
Temperature dry (°C) ¹	15.0	20.0	16.0	12.0	9.0	11.6	9.0	9.0	9.0	16.0	15.0	19.0	26.0	28.0	30.0
Temperature humid (°C) ¹	12.5	20.0	13.5	12.0	9.0	(11)	9.0	8.7	9.0	16.0	15.0	18.0	26.0	28.0	28.0
Relative Humidity (%) ¹	70-80%	100%	79%	100%	100%	>80-100%	100%	95%	100%	100%	100%	90%	100%	100%	(85%)
Condensation Point (°C)	11.2	20.0	11.5	12.0	9.0	10.5	9.0	8.5	9.0	16.0	15.0	17.5	26.0	28.0	27.0
Air Flow (pcm)	45000	65000-200000	47000	42000	0-20000	0-20000	500-16000	5000-22500	2000-12000	0-40000	0-25000	0-20000	0-50000	0-50000	0-50000

Figure 2.11: Summary of atmospheric properties for various Canadian mines [39]

2.4.2. Accelerated Corrosion Testing Standards

Accelerated corrosion testing is meant to induce levels of corrosion similar to those seen in practice, in a fraction of the time. It can be suitable for qualitative and quantitative evaluation of different materials or designs. It can also be used as a means of simple and quick corrosion of a metal, alloy or component, to then be used for other testing purposes. Many accelerated corrosion standards exist to facilitate selection of a testing scheme; however, due to the nature of corrosion testing, testing schemes can also be devised for specific needs. Listed below are four common accelerated corrosion standards relevant to the testing of ferrous alloys and coatings.

ASTM G31 Standard Guide for Laboratory Immersion Corrosion Testing of Metals [44]: This guide provides insight into best practices for immersion corrosion testing of metals. Testing recommendations are not meant to be inflexible, but instead guide users away from common errors that reduce the reliability of acquired data. It is

stated that full corrosion testing is meant to test general corrosion only, and specific testing should be done with another testing standard. Further, solution agitation and oxygen content are both mentioned as factors which would affect corrosion of certain alloys, and so both factors should be controlled accordingly.

The submersion solution should be based on the test environment being investigated. Temperature and pH level can be regulated as necessary. Test specimen geometry can be selected for whatever testing needs are required. Test specimens should include finishing with a minimum of No. 120 abrasive paper or cloth, unless the surface is to be used in a mill-finished condition. Test specimens should be scrubbed with a bleach-free power or suitable solvent. Acetone or methanol can serve this purpose. Ultrasonic polishing is an acceptable alternative. After testing is complete, specimens should be cleaned to remove any corrosive products while minimizing removal of sound metal. This will permit more accurate weight loss measurements. Test duration may be established based on the scope of testing. Corrosion rates may be calculated if no localized or internal corrosion is present. Corrosion rates for specimens under identical testing conditions should be within $\pm 10\%$, otherwise repeat testing is encouraged.

Testing equipment should consist of an enclosure of suitable size (typically 500 to 5000 ml). A reflux condenser with or without an atmospheric seal, a sparger for controlling atmosphere or aeration, and temperature regulating and heating devices may be used depending on test conditions. A test specimen support system should also be in place. All equipment materials should be inert relative to the testing material and corrosion solution. Open-enclosure tests should not be used over longer periods of time due to the potential for evaporation and contamination.

ISO 9227: Corrosion tests in artificial atmospheres – Salt spray tests [45]: Useful to evaluate the quality of different metallic materials with or without corrosion protection in a qualitative way. Salt spray tests are particularly useful in detecting discontinuities such as pores and other defects in certain metallic materials and coatings. This approach can be applied to metallic materials and coatings. Some comparative conclusions can be drawn for similar coatings; however, long term corrosion predictably from these tests is seldom reflective of actual long term corrosion.

Test conditions involve continuous exposure to a salt containing mist or fog under constant temperature conditions. Three different mists are commonly used: neutral salt spray (NSS), acetic acid salt spray (AASS), and copper acetic acid salt spray (CASS). All mists use a $50 \text{ g}\cdot\text{l}^{-1}$ aqueous sodium chloride solution. The AASS includes enough glacial acetic acid to reduce the pH to 3.2. In the CASS solution, copper chloride dehydrate is added to the AASS solution until a concentration of $0.26 \text{ g}\cdot\text{l}^{-1}$ of CuCl_2 is present. Mass-loss of steel reference specimens from the three mists are $70 \text{ g}\cdot\text{m}^{-2}$ after 48 hours, $40 \text{ g}\cdot\text{m}^{-2}$ after 24 hours, and $55 \text{ g}\cdot\text{m}^{-2}$ after 24 hours for the NSS, AASS, and CASS mists, respectively.

Test equipment consists of a fully enclosed cabinet with no less than 0.4 m^3 of test space. Upper cabinet areas must be designed to ensure droplets do not form/fall on testing specimens. Air filters must be used to remove all traces of oil and solid matter. Fog atomization must occur at overpressures of 70 kPa to 170 kPa. Collection devices should be included to collect condensed spray solution. Cabinets used for CASS cabinets can never be used for AASS or NSS testing. AASS cabinets can never be used for NSS testing.

ISO 11130: Corrosion of metals and alloys – Alternate immersion test in salt solution [46]: Useful as a quality control test during the manufacture of aluminum and ferrous alloys, as well as other metals. Also used for assessment purposes during alloy development. Alternate immersion tests in salt solutions can be used with and without application of stress. This testing scheme can sometimes be used to simulate the corrosive effects of marine splash zones, de-icing fluids and acid salt environments.

Testing consists of immersion, withdrawal and drying of test specimens. Immersion solutions include an NSS solution, various de-icing solutions including sodium sulfite, sodium sulfate, and AASS and CASS variants, an acidic salt solution (NSS with a pH of 3.5), and ocean water. Use of the sulfite and sulfate based solutions is sometimes done to promote more aggressive pitting. Testing cycles typically involve 10 minutes of immersion followed by 50 minutes of drying. Test cycles are repeated continuously throughout the duration of testing, unless prior failure occurs. Test duration normally ranges from 20-90 days, and is normally conducted at temperatures of 25°C.

Testing equipment includes a system capable of automatically and continuously removing and drying specimens to ensure reproducible cyclic patterns are maintained. All fabrication materials that come in contact with test specimens must be inert relative to the specimen and the corrosive solution. Tested specimens should be held such that they remain electrically insulated from each other and other bare metals. Uniform drying should be maintained using a suitable air circulation system.

ISO 14993: Corrosion of metals and alloys – Accelerated testing involving cyclic exposure to salt mist, “dry” and “wet” conditions [47]: This accelerated corrosion standard is similar to that discussed in ISO 9227; however, it has reportedly better

replication rates for corrosion that occurs in outdoor salt-contaminated environments. It is meant for comparative testing of different metallic alloys with similar features. It is noted that conclusions do not fully reflect the whole range of environmental corrosion conditions.

Testing is done using an NSS solution at 35°C. Dry conditions are specified as a temperature of 60°C and a relative humidity below 30%. Wet conditions are specified as a temperature of 50°C and a relative humidity greater than 95°C, but such that no condensation on test specimens occurs. Cyclic exposure consists of 2 hours in the NSS spray, 4 hours in the dry conditions and 2 hours in the wet conditions. Additionally, transition times between conditions are stated as 30 minutes for NSS to dry, 15 minutes for dry to wet, and 30 minutes for wet to mist. Average mass-loss of reference steel specimens under these testing conditions is 200 g·m⁻² after 48 hours.

Testing apparatus' are similar to those stated in ISO 9227. Additional equipment includes a heating device and fan to supply dried air during the dry periods. The air exhaust system is made such that it is not influenced by atmospheric back pressure.

2.5. Properties of Mining Wheel Fabrication Material

Multi-piece mining wheels are fabricated from HSLA structural steel. The steel used commonly originates from China, and is often referenced under the names 16Mn or Q345. The ASTM equivalent of this steel is ASTM A572 Gr. 50. The steel is qualitatively described to have good weldability and decent corrosion resistance [48].

Table 2.2 lists the primary alloying elements in weight percent of Q345 and the ASTM equivalent. Minimum yield strength, tensile strength, and % elongation of the

steel are 345 MPa, 450 MPa and 21% (over 50 mm), respectively, as stated in the ASTM A572 G50 standard [49].

Table 2.2: Chemical composition of Q345 and A572 G50

	C (wt%)	Mn (wt%)	Si (wt%)	P (wt%)	S (wt%)	Al (wt%)	V (wt%)	Ti (wt%)
Q345	≤0.2	≤1.7	≤0.5	≤0.035- ≤0.3	≤0.035	≤0.015	≤0.15	≤0.2
A572 G50	≤0.23	≤1.3	≤0.4	≤0.04	≤0.05	-	0.01- 0.15	-

2.5.1. Tensile Studies

The tensile properties of 16Mn/Q345 are reported extensively in the literature. In the work of Wang et al. [50], tensile tests of notched specimens fabricated from Q345 were performed. In their work, the effects of notch ratio, depth, and ratio on fracture mode and fracture strength are investigated. Most results are presented as a function of load and displacement, and so they are not necessarily relatable to stress and strain; however, a true-stress true-strain plot of the unnotched Q345 material reveals YS, TS and percent elongation (%E) to be 400 MPa, 632 MPa, and 18%, respectively. Furthermore, they note that specimens with a sharper notch radius and larger notch ratio show poor ductility, but greater fracture strength.

The dynamic mechanical behaviour of Q345 was investigated under ambient and elevated temperatures [51]. Testing was conducted using both compressive and split-Hopkinson pressure bar testing apparatuses, with appropriate temperature regulation hardware. Results show that at normal temperatures, Q345 displays strain-rate sensitive strengthening between quasi-static and dynamic testing conditions, but no such rate sensitivity was present in the separate quasi-static and dynamic conditions. From

ambient temperature and quasi-static testing, the YS, TS and %E were found to be approximately 380 MPa, 700 MPa, and 23%, respectively. At dynamic strains ($>2000\text{-}4000\cdot\text{s}^{-1}$), the YS, TS and %E were respectively found to be approximately 500 MPa, 850 MPa, and 30%.

A deformation and heating process was used on Q345 to refine the microstructure of the alloy in reference [52]. The treatment process consisted of multi-pass deformation, followed by rapid heating to 900°C , followed by single-pass deformation, and finally air cooling. This process achieved YS, TS and %E of 602 MPa, 656 MPa, and 21%. Grain refinement of ferrite grains was measured as $1.5\ \mu\text{m}$, and grain refinement was stated as the primary strengthening mechanism.

2.5.2. Fatigue Studies

The fatigue behaviour of 16Mn/Q345 is moderately studied in the open literature. The effects of microstructure on fatigue crack growth in Q345 steel were investigated by Xiong and Hu [53]. The purpose of the work was to simulate fatigue crack growth seen in Q345 weld joints. The study consisted of applying different heat treatments to the Q345 specimens, which represented the base metal (BZ) zone, the weld metal zone (WZ), the recrystallized (RZ) zone, and the fusion zone (FZ). Subsequently, the microstructures were observed. The BZ zone consisted of coarse-grained ferrite and colony pearlite, the WZ and RZ zones consisted of fine-grained ferrite and pearlite, and the FZ consisted of widmanstatten, reticular and acicular ferrite. Microstructures are shown in Figure 2.12. Fatigue testing was conducted at 0.1 and 0.5 load ratios. Results show that the base metal zone was not affected by the load ratios tested, but the fusion and weld zones are both sensitive to the fatigue load ratio. For the 0.1 ratio, fatigue crack growth rates are higher

in the BM than other regions, but similar at the 0.5 ratio. Scanning electron microscopy analysis reveals that for all specimens, the fatigue cracks propagate along the ferrite grains, evading the widmanstatten ferrite, and pearlite colonies. A similar investigation is conducted in the work of Baotung et al. [54], with comparable conclusions.

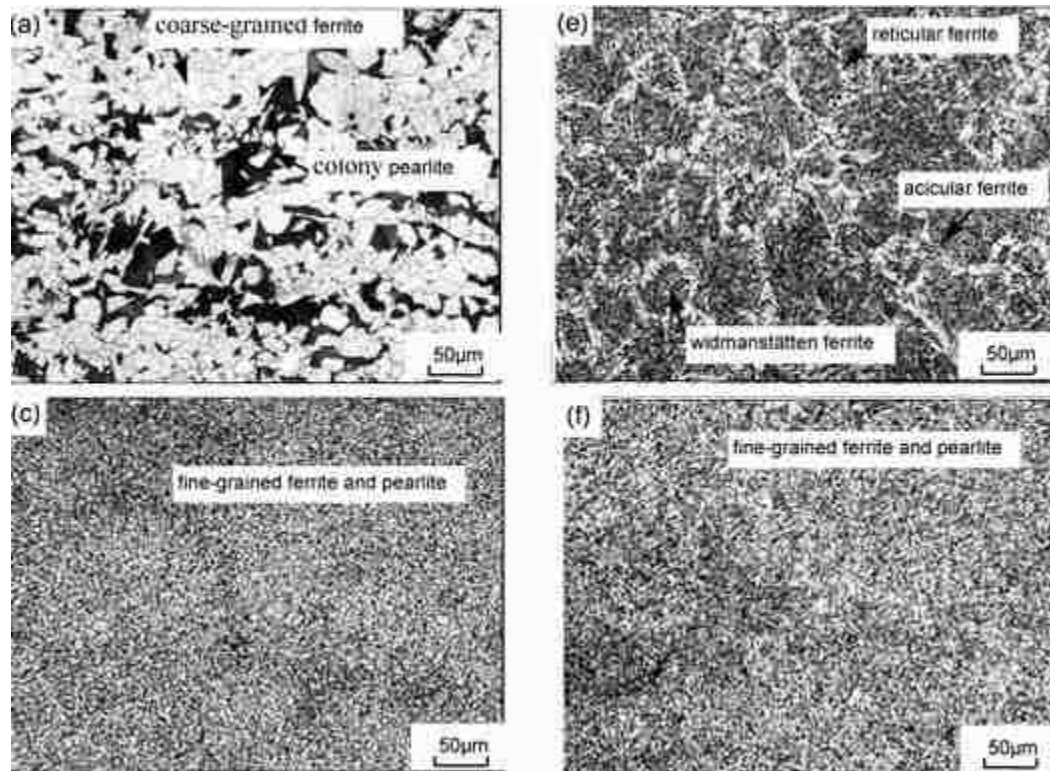


Figure 2.12: Microstructure of Q345 for different heat treatments: (a) base metal zone, (c) recrystallized zone, (e) fusion zone, (f) weld metal zone [53]

Fatigue data on 16Mn steel is discussed by Liu and Mahadevan [55]. Stress amplitudes presented were 394 MPa, 373 MPa, and 344 MPa. The associated $\log(N)$ fatigue lives were stated as 5.05 (112,201 cycles), 5.29 (194,948 cycles), and 5.85 (707,945 cycles), respectively. Figure 2.13 shows the fatigue life of the 16Mn steel tested.

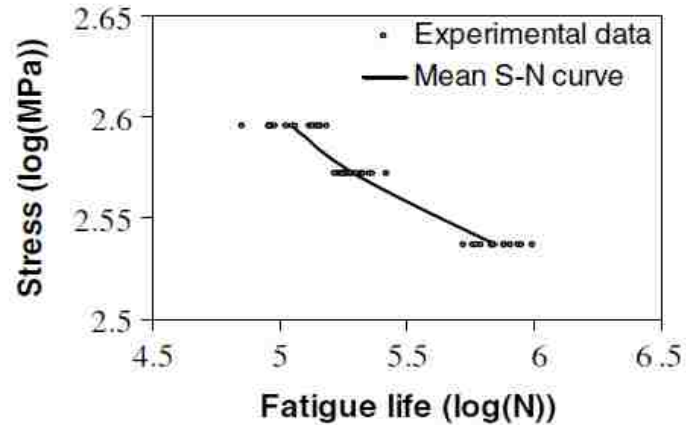


Figure 2.13: High-cycle fatigue life of a 16Mn steel [55]

2.5.3. Corrosion Studies

Corrosion studies on 16Mn/Q345 are moderately available in the open literature. However, there are no studies available documenting the effects of corrosion on the steel for the high-cycle fatigue regime.

Ji-xiong et al. [56] investigated the anti-weathering performance of different construction steels, including Q345. This was achieved by in-door cyclic corrosion tests. Testing consisted of exposure to a salt spray fog for 2 hours, followed by 4 hours of dry conditions and 2 hours of wet conditions (similar to ISO 14993). Test durations ranged from 360 hours to 1800 hours. Mass-loss of the Q345 steel after 1800 hours was recorded as approximately $7000 \text{ g}\cdot\text{m}^{-2}$. Similar testing was also conducted in reference [57], where Q345 was exposed to a 5 wt% NaCl solution in cyclic wet/dry accelerated corrosion testing conditions. This was done to simulate a marine environment. In their testing, specimens were mechanically ground using 800-grit silicon carbon paper, followed by ultrasonic cleaning in acetone and rinsing in distilled water. Full corrosion cycles were 80 minutes in length, with 18 minutes in the wet condition followed by 62

minutes in the drying condition. Testing lasted for 480 hours, with intermittent pauses to weigh specimens. Results from corrosion testing found the Q345 steel had a mass-loss of approximately $12.5 \text{ mg}\cdot\text{cm}^{-2}$ after 480 hours. Figure 2.14 shows a plot of the mass-loss behaviour of all steels tested as a function of testing time.

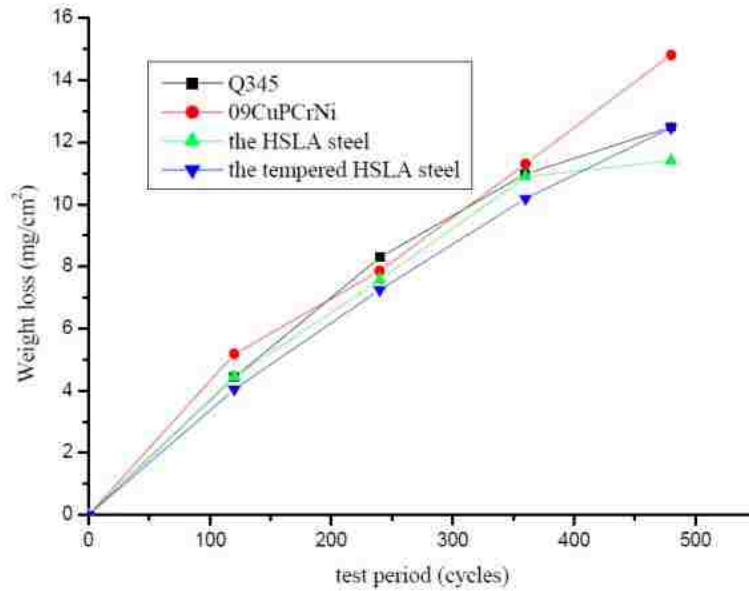


Figure 2.14: Mass-loss corrosion behaviour of Q345 and other HSLA steels after wet/dry cyclic corrosion testing [57]

The stress corrosion cracking (SCC) susceptibility of 16Mn steel in a nitrate solution was investigated by Wu et al. [58]. Their work found that there were significant differences in the electrochemical performance of ferrite and pearlite based samples. Under corrosion, pearlite preferentially corroded under the action of a galvanic cell. Microstructural observations found that corrosion began at phase boundaries between ferrite and pearlite, and then the pearlite gradually corroded until it disappeared. Corrosion then crossed into the ferrite phase. Pearlite was explained as preferentially corroding quicker than ferrite due to its microstructure. Ferrite consists of a single phase with low electrochemical potential. Conversely, pearlite is made of two dissimilar phases

(ferrite and cementite), which have different electrochemical potentials. The dissimilarity of the two phases creates a galvanic cell in the pearlite microstructure, which increases its corrosion rate in corrosive environments.

2.6. Summary of Literature Review

From studies on multi-piece wheel failures, it can be seen that many wheel failures are attributable to the combined effects of corrosion and fatigue. Wheel components are fabricated from the Q345 alloy, a HSLA structural steel, with primary alloying elements of carbon, manganese, and silicon. The fatigue behaviour of this alloy is not well documented in the literature, and no studies are available which show the effects of corrosion on the fatigue behaviour of this alloy. Some corrosion studies have been conducted on the Q345 alloy that provides corrosion rates which may be used for comparison during experimental testing.

The mechanisms of fatigue failure have been thoroughly reviewed to facilitate in the development of a fatigue testing plan and in the evaluation of fatigue testing results. Similarly, methods of statistical analysis of fatigue data have been discussed. Corrosion testing schemes have also been reviewed to facilitate preparation of a simple and effective corrosion testing scheme for this study. A summary of corrosive mining environments is also presented to develop an accelerated corrosion testing scheme more reflective of actual mining conditions.

3. EXPERIMENTAL PROCEDURES

Tensile and stress-based fatigue testing on the structural steel extracted from the components of a five-piece mining wheel was performed (BS Band, Lock Ring, Flange, Gutter, Rim Base). Testing was conducted in the as-extracted and pre-corroded conditions. The as-extracted condition represents material extracted from new five-piece mining wheels. The pre-corroded condition represents material extracted from new five-piece wheels, and subjected to a corrosive solution. The pre-corroded condition was used to simulate the corrosive environment mining wheels are exposed to over prolonged durations. It was not possible to directly use worn mining wheels because any sign of corrosion or wear on a used mining wheel would be removed during the specimen extraction process. Fully submerged mass-loss based accelerated corrosion testing in an aerated saltwater solution was completed to induce pre-corrosion on the tensile and fatigue specimens. Mass-loss was measured during the process, and surface roughness measurements were taken following completion of corrosion testing.

Prior to extensive tensile and fatigue testing, preliminary testing was conducted on all wheel components to estimate variations in material properties between wheel components. This was done to reduce the number of required testing conditions, notably for fatigue testing, in recognition of the machining resources and testing time associated with the scope of fatigue testing of this study. Initial testing included EDS analyses, cross-sectional hardness measurements, microstructural analyses, and some preliminary tensile and fatigue testing. Based on initial testing, it was found that the BS Band, Flange

and Rim Base all had similar hardness, microstructural, tensile and fatigue behaviour. Hence, testing sometimes omitted one or more of these components, notably for pre-corrosion fatigue testing, without affecting the overall scope of the study. Nevertheless, all data, including initial testing data, are presented and discussed in Chapter 4.

3.1. Specimen Extraction

Steel specimens were extracted from all components of a five-piece mining wheel. For the BS Band, Lock Ring, and Flange, specimen extraction was performed entirely in-house. For the Rim Base and Gutter subsection, the components were first sectioned off-site into smaller pieces, to facilitate processing. During off-site sectioning, reciprocating saw kits were used to separate the Rim Base and Gutter into thirds. Subsequently, these pieces were cut in half using a bandsaw. No liquid cooling was used during this sectioning process; as such, some heat induced microstructural changes were expected within the vicinity of all cutting zones. Therefore, specimen extraction was done at a minimum distance of 50 mm from any cutting region.

Specimen extraction from a component was first completed using a Hyd Mech DM-10 2.5 HP bandsaw with liquid cooling. Specimens were cut into various rectangular sizes, based on the intended specimen geometry, e.g., tensile, fatigue. Following this process, specimens were centred in preparation for lathe cutting.

Once specimens had been centred, they were lathe cut using a Trak TRL 1745P lathe and carbide tip. Two separate lathe cutting processes were used. First, the rectangular specimens were turned down into cylindrical specimens. Following this, they were cut into their final shape. During the lathe cutting process, coolant was used to

minimize the potential for thermally induced hardening or softening of specimen surfaces. Over 150 specimens were generated following these procedures.

3.2. Energy Dispersive Spectroscopy Analysis

The 16 Mn/Q345 is stated to be the structural steel used in fabrication of all components of the five-piece wheels examined in this study. The nominal composition of this steel is listed in Table 2.2. To verify that the composition of the steel was within nominal ranges, energy dispersive X-ray spectroscopy (EDS) analysis was performed on samples extracted from all wheel components. This technology functions on the principle that each element emits a unique X-ray spectrum when a solid sample is bombarded with a focused beam of electron, thus allowing for chemical analysis of various materials and alloys. Using EDS analysis, elements with atomic numbers 4 to 92 can be detected; however, not all machines are equipped for analysis over this elemental range.

All EDS analyses were conducted using a FEI Quanta 200 FEG Scanning Electron Microscope equipped with an EDAX Energy Dispersive Spectroscopy X-Ray Detector. A voltage of 10 kV was used during testing. Analyses were performed at magnifications of ranging from 100x to 500x, to ensure general compositional levels were acquired.

Energy dispersive X-ray spectroscopy is not suitable for detection of trace amounts of alloying elements. Instead, it is recommended for detecting elements consisting of at least 0.5-1 weight % of the alloy [59]. Therefore, EDS analysis was only used for confirmation of the approximate content of manganese and silicon in the steel.

3.3. Accelerated Corrosion Testing

Accelerated corrosion testing was conducted to generate corrosion damage onto the surfaces of tensile and fatigue specimens intended for testing in the pre-corroded condition. The degree of corrosion was selected based on two specifications: (1) a total specimen mass-loss exceeding 1%, and (2) a specimen surface condition similar to in service mining wheels.

3.3.1. Mass-Loss

Corrosion based mass-loss was accomplished using a fully submerged accelerated corrosion testing scheme. This scheme was selected based on its ease of implementation. It is recognized that a testing scheme more similar to that of ISO 9227 or ISO 11130 might better reflect the mining environment; however, this is not necessarily the objective of the corrosion testing. Instead, the objective of the accelerated corrosion testing is to induce levels of surface corrosion onto the pre-corroded specimens similar to those of long-term in service mining wheels. As long as the corrosion mechanism is similar between laboratory testing and in-service conditions, e.g., general versus pitting or chloride versus sulphate, the testing scheme used should not be of great concern [35].

From section 2.4.1, it was found that a majority of mining environments surveyed contain levels of chloride and sulphate. One or both of these two elements may be present in large concentrations. Overall, the ground-water composition of a mine can be dictated by the type of mine, level of processing, and geographical location. For this study, a saltwater solution of 3.5 wt% NaCl was used for accelerated corrosion testing. This solution was selected to induce a general and more uniform level of corrosion onto the surfaces of the pre-corroded specimens, as opposed to the use of a sulphate based

solution, which may lead to unpredictable pitting. The chloride based solution was also selected based on the metallurgical analysis of a cracked rim gutter, discussed in section 2.1.2, in which only chloride levels are stated to be present in the gutter cracks [11].

During submerged testing, the NaCl solution was aerated using an off-the-shelf air pump. The air pump generated a maximum air flow of 10.67 litres per minute, and provided a small amount of agitation to the solution. Use of the air pump was done to ensure consistent levels of oxygen were present throughout testing, thus maintaining more consistent rates of corrosion.

From recommendations made in ASTM G31, pre-corroded fatigue and tensile specimens were polished using 120-grit silicon carbide paper, and cleaned using an acetone solution prior to corrosion testing. Test specimens were individually suspended in the NaCl solution, avoiding contact with other specimens. Specimens were suspended using non-reactive polycarbonate mounting strips. The corrosion solution was contained in non-reactive polypropylene containers. A container was used for each wheel component tested. Figure 3.1 shows the test setup.



Figure 3.1: Accelerated corrosion test setup: (a) all corrosion containers, and (b) top view of one corrosion container

Mass-loss was tracked for two specimens per wheel component over the course of submerged corrosion testing. Mass measurements were taken every three days using a 0.01 g precision scale. Tracked specimens were cleaned of any debris prior to recording the mass. Specimen cleaning generally consisted of exposure to warm running water for five or more minutes, followed by air drying.

Mass-loss was calculated using Equation (3.1) and Equation (3.2). Equation (3.1) calculates mass-loss as percent mass loss relative to the initial mass of the tracked specimens. In Equation (3.2), mass loss is computed as the mass-loss relative to the initial mass, divided by the surface area of the tracked specimens. The second mass-loss calculation approach was done to facilitate comparison with mass-loss data of Q345 in the literature. In both equations, M_f and M_i represent initial and final mass loss values. In Equation (3.2), SA denotes specimen surface area.

$$\% \text{ Mass Loss} = \left| \frac{(M_f - M_i)}{(M_i)} \right| \times 100\% \quad (3.1)$$

$$\text{Surface Area Mass Loss} = \left| \frac{(M_f - M_i)}{SA} \right| \quad (3.2)$$

3.3.2. Surface Roughness

After submerged corrosion testing was complete, specimens were allowed to dry. Specimens were then periodically re-exposed to the NaCl solution over the course of two weeks, or until a layer of corrosion consistent with in-service mining wheels had developed on the surface of the specimens.

The level of surface corrosion was evaluated based on surface roughness. A Mitutoyo SurfTest SJ-201 contact surface profilometer was used to measure surface roughness. With this tool, a diamond stylus is moved vertically in contact with a sample, and then moved laterally across the sample over a predefined distance and contact force. The surface roughness profile is generated over the duration of this process. Surface roughness values such as the arithmetic average roughness (R_a), and the surface roughness depth (R_z) are then automatically calculated from the surface profile. R_a roughness represents the mean surface roughness from the generated surface profile. R_z roughness represents the surface roughness depth as taken from a local maximum peak to a local minimum valley. The R_z value is calculated from the mean of five sampling lengths over the total length of the surface roughness profile. Figure 3.2 shows an example surface roughness profile, with five equally spaced sample readings for calculation of the R_z surface roughness.

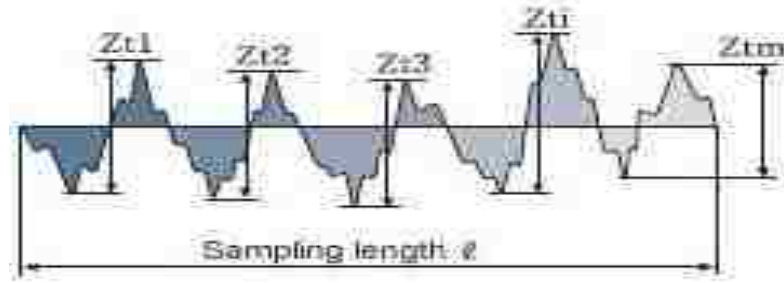


Figure 3.2: Roughness profile with equally spaced roughness readings for calculation of R_z

Roughness measurements were also taken from used wheel components for comparison with sample corrosion specimens. Additionally, surface roughness measurements of new wheels and polished fatigue testing specimens were taken for reference purposes.

3.4. Optical Microscopy

Optical microscopy was used to observe the microstructure of the steel of each wheel component. The presence of significant variations in microstructures was later used as a first step in establishing testing plans for fatigue and tensile testing. For example, if no significant differences in microstructure between the Flange and Rim base existed, fatigue testing of both components may not be necessary, given that they are fabricated from the same structural steel.

Microscopy samples for each wheel component were mounted in diallyl phthalate using a Buehler Simplimet mounting press. Each specimen was then ground using progressively finer silicon carbide papers, ranging from 320 to 600-grit. Grinding was performed on a Buehler Handimet 2 grinder. Specimens were then polished using 1.0 μm and 0.05 μm aluminum polishing suspensions. Between all grinding and polishing stages, each sample was washed and dried to ensure that all suspended particles

from the previous operation were removed, thereby preventing specimen scratching. After polishing, specimens were etched in a 2% nital solution to reveal microstructural features. Specimens were exposed to the etchant for no longer than 6 seconds, after which they were washed in water and then alcohol, and air dried.

Specimen microstructures were evaluated using qualitative and quantitative methods. Qualitative evaluation consisted of identifying different microstructure features, such as different phases, e.g., ferrite or martensite; potential inclusions; and grain boundary orientations. Microstructures were observed at magnifications from 100x - 500x. In initial observations, it was found that all microstructures consisted of ferrite and an unresolved phase. To determine the unresolved phase, scanning electron microscopy was used to observe the microstructure at higher resolutions.

A scanning electron microscope uses a focused beam of high-energy electrons to generate a variety of signals at the surface of solid specimens. The signals that are derived from interaction between the electrons and material sample are used to reveal information about the sample. Types of information revealed include surface topology, chemical composition, and crystalline structure and orientation. For most cases, SEM analysis consists of collecting data over a selected area of the surface of the sample, which is then used to generate a 2-dimensional image of the surface. Magnifications using SEM can range from 20x to 30,000x, far exceeding conventional optical microscopy magnification ranges.

From studies in the literature on Q345/16MN [52] - [54], a microstructure consisting primarily of ferrite and pearlite was expected for all wheel components. Based on component thickness, and differing cooling rates during fabrication, volume fractions

of ferrite and pearlite were expected to vary between components. To quantify this variance and evaluate its impact, area fractions of ferrite and pearlite in all component microstructures were calculated.

Calculation of area fractions of ferrite and pearlite were performed using ImageJ [60], a public domain Java image processing program. Using ImageJ, micrographs were converted to binary black and white images, with black areas representing pearlite and light areas representing ferrite. Following conversion, the software automatically calculated area fractions of black and white areas. Sometimes, further preprocessing of an image was necessary prior to analysis to remove shadows and other artifacts which might artificially influence area fraction calculations. Figure 3.3 shows an example conversion of a micrograph from colour into binary using ImageJ.

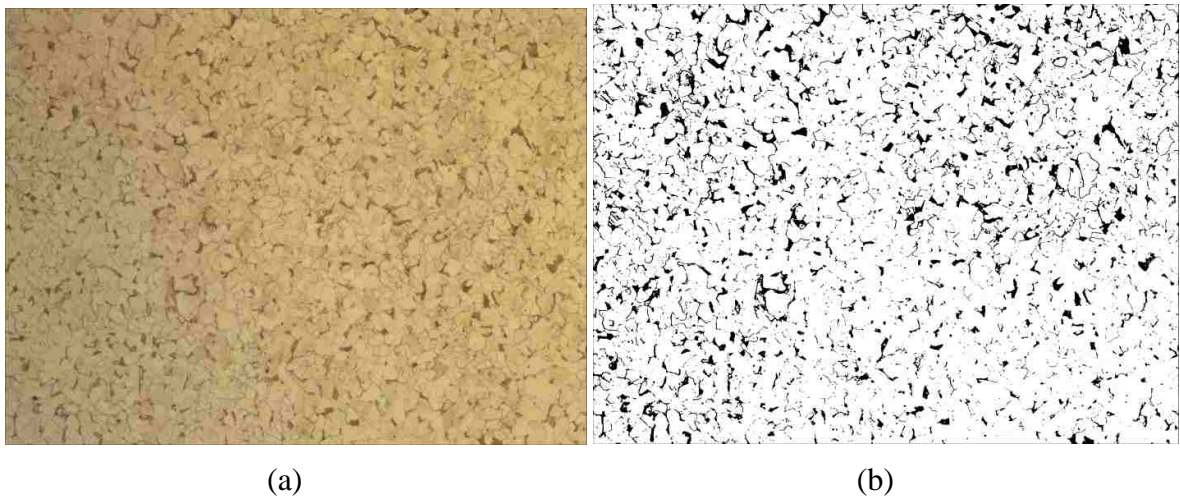


Figure 3.3: (a) 100x micrograph of specimen extracted from the flange, (b) binary image of (a) created using ImageJ

3.5. Cross-Sectional Hardness Measurements

Indentation hardness measurements typically correlate linearly with tensile strength for metallic materials [61]. Hence, hardness measurements can provide insight

into how wheel components vary in material strength. Indentation hardness testing can also reveal variations in hardness as a function of depth. For specimen extraction from wheel components, this information is essential because tensile and fatigue specimens generally could not be not extracted near wheel component surfaces due to machining constraints. Therefore, if there are variations in hardness across component cross-sections, tensile and fatigue data might not accurately reflect bulk wheel component material properties, and will require correction. For these reasons, cross-sectional hardness measurements were recorded for all wheel components.

Cross-sectional hardness testing was done using a Wilson Rockwell hardness tester. The machine was verified in accordance with ASTM E18 [62], which details standard testing methods for Rockwell hardness testing of metallic materials. Rockwell B measurements were taken using a 1.588 mm steel sphere with a 100 kgf load. Measurements were recorded across the thickness of each wheel component at intervals of 3-4 mm. Measurements were performed three times at each depth, and average values were used to plot hardness as a function of component depth. Surfaces for all hardness testing samples were machined to be flat, i.e., parallel with the sample mounting surface of the Wilson machine. Furthermore, they were ground up to 600-grit to remove any surface irregularities that might affect hardness testing. Figure 3.4 shows the testing setup with a tested lock ring sample.



(a)



(b)

Figure 3.4: (a) Wilson Rockwell Hardness tester and (b) sample Lock Ring hardness specimen

3.6. Tensile Testing

Quasi-static tensile testing was conducted to determine the mechanical properties of the steel used in fabrication of all wheel components. Properties determined from testing included yield strength, ultimate tensile strength, modulus of elasticity, and percent elongation.

Tensile testing was conducted on steel specimens extracted from all wheel components to evaluate any differences in mechanical properties due to microstructural variations. Tensile specimens were tested in the as-extracted and pre-corroded conditions. Pre-corrosion testing was conducted to evaluate its effect on tensile strength.

A reduced-size, round tensile specimen geometry was used for all tensile tests, in accordance with ASTM E8/E8M [63]. This geometry was selected based on wheel component dimensions, which prevented extraction of sufficient material for manufacture of standard-sized specimens. Overall, tensile specimens had a diameter of 6.35 mm, a fillet radius of 1.68 mm, a holding diameter of 9.52 mm, a gauge length of 51.25 mm, and a total length of 105.41 mm. Figure 3.5 shows the specimen geometry with relevant dimensions.

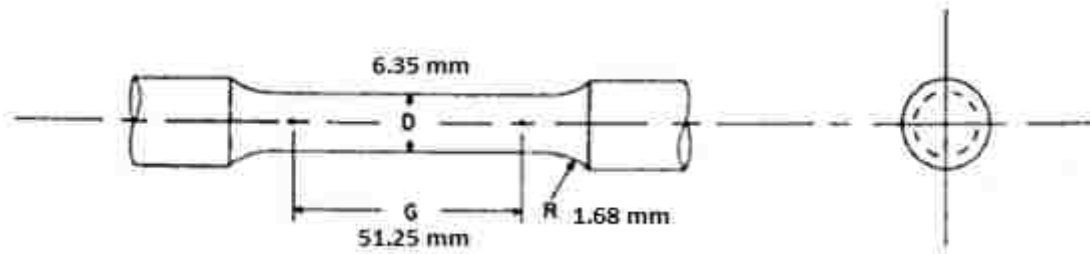


Figure 3.5: Tensile specimen geometry with gauge length, G, of 51.25 mm, fillet radius, R, of 1.68 mm, and gauge diameter of 6.35 mm

All tensile specimens were prepared using identical cutting and machining parameters. Additionally, all tensile specimens were ground with silicon carbide papers up to 320-grit to ensure an even surface finish, free of stress concentrators that would otherwise increase the potential for premature specimen failure.

Tensile testing was carried out on a MTS servo-driven universal testing system, with a ± 50 kN capacity, under ambient room conditions. A crosshead extension rate of $0.01 \text{ mm}\cdot\text{s}^{-1}$ was prescribed to tensile specimens, in an effort to minimize dynamic effects. The MTS machine was controlled using a computer, which was also used to save acquired data. A data acquisition rate of 16.67 Hz was used to acquire load-elongation data.

During testing, an extensometer was placed on the gauge region of the specimens to track specimen strain. Data output from the testing machine computer included the 0.2% offset yield strength, modulus of elasticity, tensile strength, and percent elongation to failure. Additionally, load-elongation measurements were recorded. As a precautionary check, all load-elongation data was processed using suitable software, to ensure testing values output from the MTS computer were accurate. Figure 3.6 shows the test setup with application of the extensometer onto a pre-corroded tensile specimen.

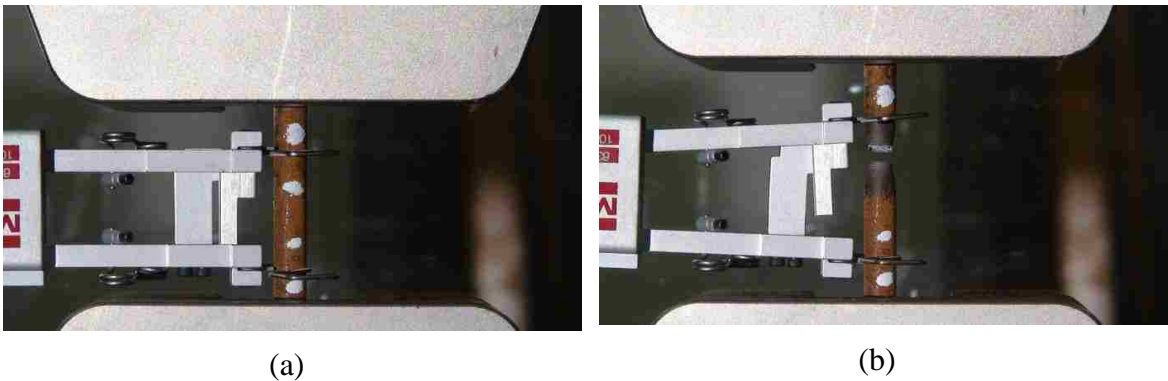


Figure 3.6: Tensile testing of pre-corrosion tensile specimen equipped with extensometer for strain tracking: (a) before testing), and (b) after testing

3.7. Fatigue Testing and Analysis

Fatigue assisted failure is a primary mode for which multi-piece mining wheels fail, as reported in the literature and discussed in section 2.1. To evaluate how fatigue contributes to wheel failures, fatigue testing of steel samples extracted from all components of a five-piece mining wheel was conducted. Testing consisted of stress-based rotating bending fatigue testing, statistical analysis of the acquired fatigue data, and fracture surface evaluation of a select number of fatigue specimens.

3.7.1. Fatigue Testing Procedures

Multi-piece wheels are typically in service for prolonged periods of time (>1 year) prior to fatigue failure [2]. This is indicative that fatigue failure of the wheels occurs primarily in the high-cycle fatigue regime. Thus, material fatigue behaviour was evaluated in the high-cycle fatigue regime (10^4 to 10^6 cycles) in this study. Given that this regime of fatigue is governed by crack initiation mechanisms, both stress-based and strain-based fatigue evaluation methods are acceptable. However, it is anticipated that the steel tested has an endurance limit [13], making only the stress-based testing scheme applicable [13], as discussed in section 2.2.2. Therefore, stress-based fatigue testing was used in this study.

There is strong evidence that wheel failures are influenced by mechanisms of fatigue and corrosion. As a first step to investigate the combined effects of these two aspects, fatigue testing was conducted on pre-corroded fatigue specimens. The fatigue behaviour of Q345 was compared between the pre-corroded and as extracted conditions.

Stress-based fatigue testing was conducted on an Instron R.R. Moore rotating-bending fatigue testing machine. Figure 3.7 shows the machine under operation. Testing was performed under ambient atmospheric conditions. The R.R. Moore machine was operated at frequencies ranging from 83 hz to 117 hz (5000 rpm to 7000 rpm). Specific operating frequencies were adjusted for each specimen and loading condition in an effort to minimize machine vibration. Machine vibration would become an issue if operating frequencies approached machine resonant frequencies, which are influenced by loading and specimen imperfections, e.g., non-uniform specimen mass distribution.

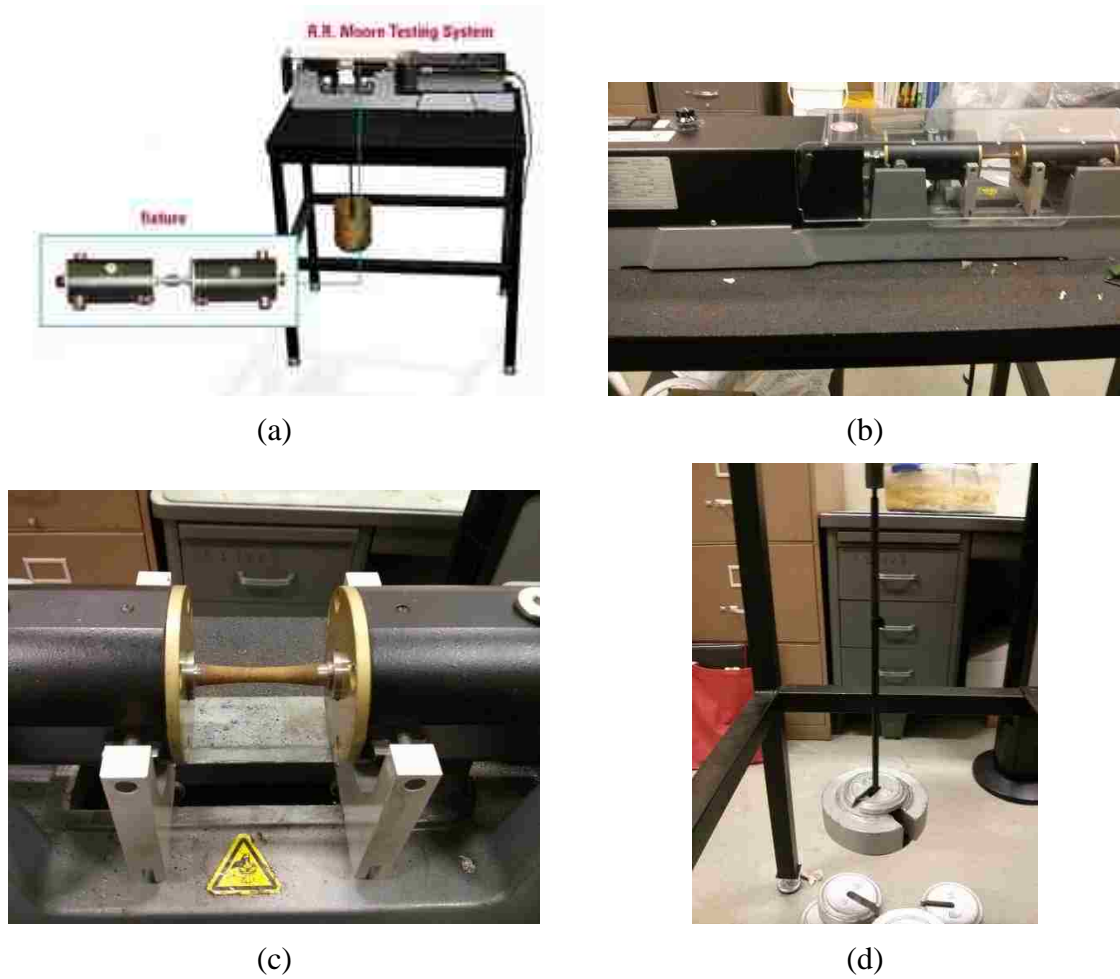


Figure 3.7: (a) Instron illustration of RR Moore system, (b) RR Moore machine in operation, (c) up close image of image machine with pre-corroded specimen, and (d) weights used to adjust specimen stress

A straight shank fatigue specimen geometry was used during fatigue testing. With this geometry, the specimen has an hourglass shape with straight ends to be held by collets during operation. This geometry was selected based on ease of manufacturing versus a tapered-end specimen, which requires additional fabrication time. Fatigue specimen dimensions are illustrated in Figure 3.8. Dimensions consisted of an end diameter of 9.27 mm, a minimum diameter, located at the centre of the specimen, of

approximately 5.75 mm, an hourglass section length of 49.21 mm, and a total length of 87.31 mm. Surface area of the fatigue specimen was approximately 23.19 cm².

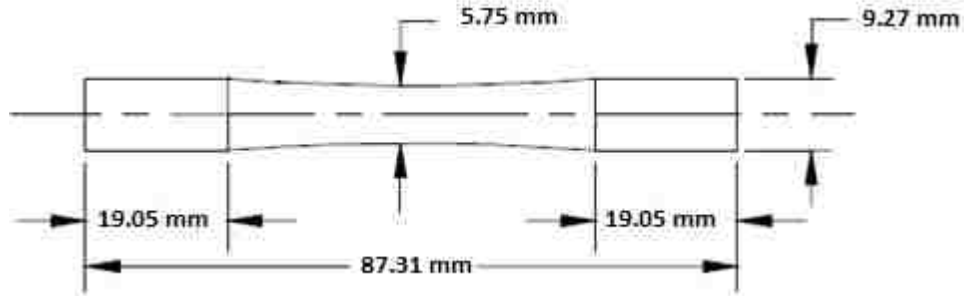


Figure 3.8: Fatigue specimen geometry and dimensions

Fatigue specimens were ground using a drill press operated at 1500 rpm. Fatigue specimens were mounted on the drill press and ground using progressively finer silicon carbide grit papers, ranging in grit from 120-grit to 600-grit. A minimum of three minutes was allocated to grinding for each grit paper for each specimen. Following grinding, the surface roughness of one or two fatigue specimens was measured in an effort to maintain some degree of quality control during the grinding process. Overall, fatigue surface roughness was maintained at or below 0.4 μm , measured using R_a roughness, described in section 3.3.2. A sample roughness profile of a fully ground Rim Base fatigue specimen is included in Figure 3.9.

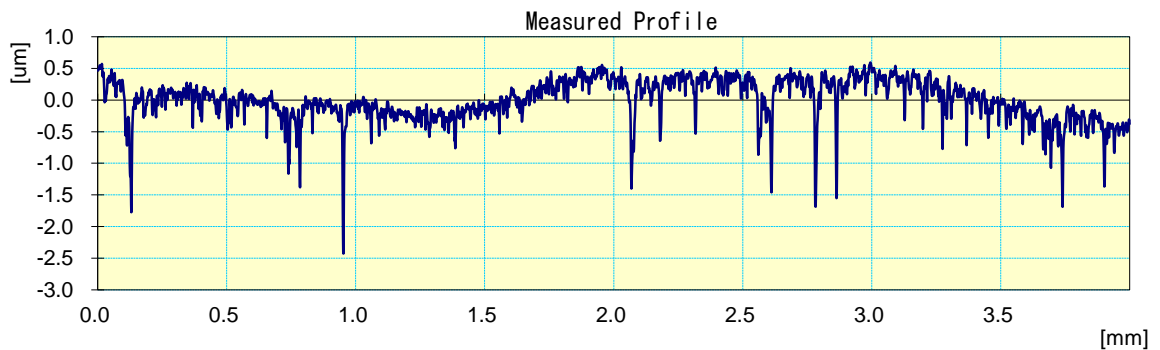


Figure 3.9: Sample roughness profile of fully ground Rim Base fatigue specimen

Fatigue loading conditions were selected to encompass failure cycles between 10^4 to 10^6 cycles. In total, five failure loading conditions were selected in addition to an infinite life condition. Failure conditions were meant to reflect cycles to failure of approximately 50,000 cycles, 125,000 cycles, 315,000 cycles, 792,000 cycles, and 1,999,000 cycles. The infinite life, or endurance limit, was selected as 5,000,000 cycles. Loading conditions are summarized in Table 3.1.

Initial loads for each fatigue condition were established based on the historical fatigue performance of low alloy steels [19], in which the endurance limit is specific as 50% of the UTS. Of course, some variations were expected between historical data and the specific alloy under investigation, resulting in the potential for fatigue loads to over or undershoot desired failure cycles. To overcome this discrepancy, the first fatigue load was conducted at the estimated 792,000 cycles to failure condition. Based on the actual cycles to failure recorded for the first test, previously calculated loads were adjusted to better align with desired failure cycles; however, even using this practice, failure cycles were sometimes unpredictable, given the stochastic nature of fatigue testing. Consequently, desired failure cycles were not always practically achievable with the limited pool of fatigue specimens fabricated for testing. Thus, in some instances of fatigue testing, a trial-and-error testing approach was used in favour of the pre-determined fatigue conditions testing approach. This was especially prominent during pre-corroded fatigue testing, where fatigue performance was expected to significantly decrease relative to the as-extracted testing condition.

Table 3.1: Estimated cycles to fatigue failure and corresponding loads

Estimated Failure Cycles	Estimated Load (MPa)	Time Required per Test (hrs)
50,000	334	0.14
125,000	311	0.35
315,000	290	0.88
792,000	270	2.20
1,999,000	251	5.53
5,000,000	234	13.89

From initial material testing described throughout Chapter 3, it was found that all wheel components exhibited similar properties, consistent with the minimum mechanical requirements of the Q345/16Mn alloy, with the exception of the Lock Ring. Nevertheless, fatigue testing in the as-extracted condition was conducted for steel specimens extracted from all wheel components. This decision was made in the event that some variation in fatigue behaviour was found, despite the consistency of other material properties for the wheel components. If fatigue behaviour between components was consistent, the data could be combined to form a more statistically relevant dataset of the steel alloy. Fatigue testing of pre-corroded conditions was limited to the Lock Ring and Gutter regions. This was decision was made based on observations from fatigue testing of as-extracted components, as well as the consistency of other material properties between components.

Two to four fatigue specimens were used to test each loading condition for material extracted from each wheel component. Loading conditions were tested at random to eliminate bias produced from sequential testing. Given that all components were tested in the as-extracted condition, and two components were tested in the pre-corroded condition, roughly 84 to 168 fatigue specimens were tested in total. Under the

average of three specimens per loading condition, the fatigue testing is classified as “Design Allowable” or “Reliability”, as per ASTM E739 [31], summarized in Table 2.1.

3.7.2. Statistical Analysis of Fatigue Data

Analysis of fatigue data was consistent with the procedures discussed in section 2.3. A summary of analysis procedures is presented below.

The percent replication of data collected for each fatigue dataset (wheel component, material condition) was calculated using Equation (2.1), as per ASTM E739 [31] recommendations. Fatigue specimens which did not fail (run-out) were not included in the calculation. The number of loading conditions was approximated from visual inspection of the fatigue curve under analysis.

A log-linear regression analysis was conducted on each dataset. Applied stress was taken as the independent variable. The cycles to failure was taken as the dependent variable. The logarithm of cycles to failure for each dataset was taken. A straight line of the form of Equation (2.2) was then fit to each modified data set. Maximum likelihood values of the slope and intercept of each equation were calculated using Equation (2.4) and Equation (2.3), respectively. Equations (2.2), (2.3) and (2.4) are reproduced below for convenience.

$$Y = A + mX \quad (2.2)$$

$$\hat{A} = \bar{Y} - \hat{m}\bar{X} \quad (2.3)$$

$$\hat{m} = \frac{\sum_{i=1}^n (X_i - \bar{X})(Y_i - \bar{Y})}{\sum_{i=1}^n (X_i - \bar{X})^2} \quad (2.4)$$

Following regression analysis, the statistical relevance of each fit was evaluated using three different criteria. The F-test, Equation (2.8), was used to evaluate the significance of each fit. T-tests, Equations (2.10) and (2.11), were used to evaluate the significance of the slope and intercept of each fit. The effectiveness of a fit at representing its corresponding dataset was measured by calculating the coefficient of determination (R^2) using Equation (2.9). In depth discussion of these analysis techniques is provided in section 2.3.2; however, for the convenience of the reader, equations for the F-test, T-test and coefficient of determination are reproduced below.

$$F = \frac{SSR}{SSE/(n-1)} \quad (2.8)$$

$$R^2 = \frac{SSR}{SSR + SSE} \quad (2.9)$$

$$S_{\hat{m}}^2 = \frac{S_{YX}^2}{\sum_{i=1}^n (X_i - \bar{X})^2} \quad (2.10)$$

$$t_{obs, \hat{m}} = \hat{m} / S_{\hat{m}}$$

$$S_{\hat{A}}^2 = \frac{S_{YX}^2 \sum_{i=1}^n X_i^2}{n \sum_{i=1}^n (X_i - \bar{X})^2} \quad (2.11)$$

$$t_{obs, \hat{A}} = \hat{A} / S_{\hat{A}}$$

Confidence bands were calculated for each dataset fit. The purpose of the confidence bands were to graphically represent the upper and lower limits for which each fit is valid on an S-N curve. Additionally, the lower confidence band provides a more conservative estimate of fatigue behaviour. Therefore, the lower confidence limit of each

fit was used to quantitatively evaluate the lower limit endurance strength of each fatigue dataset, determined by the stress at 5,000,000 cycles. Confidence bands were calculated using Equation (2.13). Additionally, confidence bands were calculated using Equation (3.3). Equation (3.3) is a modified version of Equation (2.13), with all stress terms removed. As a result, confidence bands calculated using (3.3) are simply linear shifts in the fit, along the stress-axis, as depicted on an S-N curve. The primary benefit of using Equation (3.3) is that the bands generated are of the form of Equation (2.2), which allows for easy implementation within fatigue design problems.

$$Cl = fit \pm t_{crit} S_{YX} \sqrt{\left[1 + \frac{1}{n} + \frac{(X_i - \bar{X})^2}{\sum_{i=1}^n (X_i - \bar{X})^2} \right]} \quad (2.13)$$

$$Cl = fit \pm t_{crit} S_{YX} \sqrt{\left[1 + \frac{1}{n} \right]} \quad (3.3)$$

3.7.3. Surface Analysis

Surface analysis of fractured fatigue specimens was performed using scanning electron microscopy. The purpose was to qualitatively evaluate different failure regions, such as the crack initiation region, the crack propagation region, and the failure region. Specifically, variance in these regions was investigated based on variations in fatigue behaviour, such as that expected between as-extracted and pre-corroded fatigue specimens. Furthermore, fracture surface features were observed for low-cycle and high-cycle loading conditions to determine if any differences were present.

Scanning electron microscopy was conducted using a FEI Quanta 200 FEG Scanning Electron Microscope. Scanning electron microscopy analysis was done under a voltage of 15 kV in high vacuum. Magnifications ranged from 25x to 2000x, based on the feature being observed.

3.7.4. Fatigue Testing Matrix

Table 3.2 provides a summary of the planned fatigue testing in this study.

Table 3.2: Initial fatigue testing matrix

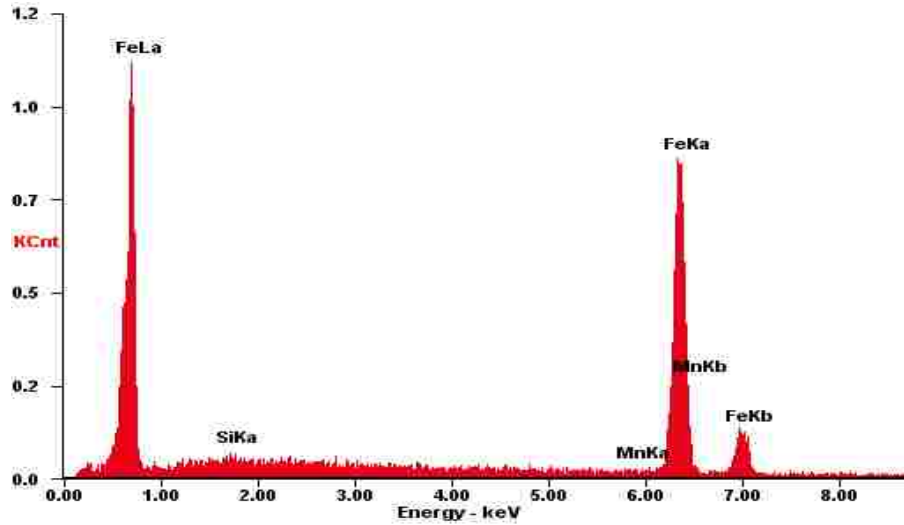
As-Extracted Fatigue Testing												
Load Estimates			Rim Base		BS Band		Flange		Gutter		Lock Ring	
Estimated Failure Cycles	Estimated Failure Loads (MPa)	Time per Test (hours)	Planned Testing Specimen	SEM Analysis	Planned Testing Specimen	SEM Analysis	Planned Testing Specimen	SEM Analysis	Planned Testing Specimen	SEM Analysis	Planned Testing Specimen	SEM Analysis
50000	334	0.14	3		3		3		3	x	3	x
125000	311	0.35	3		3		3		3		3	
315000	290	0.88	3		3		3		3		3	
792000	270	2.2	3		3		3		3		3	
1999999	251	5.53	3		3		3		3	x	3	x
5000000	234	13.89	3		3		3		3		3	
Pre-Corroded Fatigue Testing												
Load Estimates			Rim Base		BS Band		Flange		Gutter		Lock Ring	
Estimated Failure Cycles	Estimated Failure Loads (MPa)	Time per Test (hours)	Planned Testing Specimen	SEM Analysis	Planned Testing Specimen	SEM Analysis	Planned Testing Specimen	SEM Analysis	Planned Testing Specimen	SEM Analysis	Planned Testing Specimen	SEM Analysis
50000	334	0.14							3	x	3	x
125000	311	0.35							3		3	
315000	290	0.88							3		3	
792000	270	2.2							3		3	
1999999	251	5.53							3	x	3	x
5000000	234	13.89							3		3	
Total Planned Testing Specimens		Total Estimated Machine Runtime (hours)										
126		482.79										

4. RESULTS AND DISCUSSION

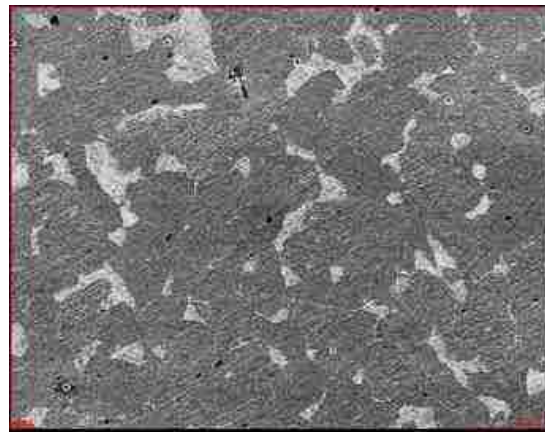
In this chapter, the experimental results of the mechanical and material testing discussed in Chapter 3 are presented. Material testing consisted of EDS analysis, microstructural analysis, and cross-sectional hardness measurements of steel samples extracted from all components of a five-piece mining wheel assembly. Tensile and fatigue tests were conducted on specimens in the as-extracted and pre-corroded conditions, to reflect new wheels and wheels subjected to corrosion over time in the mining environment. Pre-corroded specimens were generated using submerged corrosion testing, in which mass-loss and surface roughness measurements were noted for some specimens. Based on observed variations in material and tensile properties between wheel components, a fatigue testing scheme was developed. Fatigue testing was conducted on specimens from all wheel components in the as-extracted condition, and on specimens from the Lock Ring and the Gutter regions in the pre-corroded condition. Wheel components demonstrated consistent tensile properties, with the exception of the Lock Ring, which showed superior yield and tensile strength properties. Fatigue behaviour of as-extracted specimens was consistent for most components, with the exception of the Gutter region, which demonstrated slightly improved fatigue behaviour. In the pre-corroded condition, fatigue behaviour was consistent between Lock Ring and Gutter region specimens. In both instances, pre-corroded fatigue behaviour was significantly reduced relative to the fatigue behaviour in the as-extracted condition.

4.1. Energy Dispersive Spectroscopy Analysis

The HSLA structural steel used in fabrication of all wheel components is known as Q345 or 16Mn. Alloying elements in this steel are carbon, manganese, silicon, phosphor, vanadium, and sulfur. To verify that all components of the five-piece wheels in this study were fabricated using the Q345/16Mn alloy, energy dispersive spectroscopy analysis was conducted on steel samples extracted from all components. Elements quantified using the EDS technique were iron, manganese, and silicon. Other alloying elements were too low in concentration to be accurately detected using EDS analysis. Corrections in measurements were made to include a nominal Carbon content of 0.2 wt%, consistent with the Q345 alloy.



(a)



(b)

Figure 4.1: (a) EDS Spectrum of BS band at 500x magnification, (b) BSE image of the sample analyzed

Figure 4.1(a) is an EDS spectrum taken from a BS band sample at 500x, while Figure 4.1(b) is the back-scattered electron (BSE) image of the sample. From Figure 4.1(a) it can be seen that peaks are readily observable for iron and manganese. Additionally, a rise in energy is observable near the silicon peak, indicative of some presence of silicon. This peak is less prominent than those of iron and manganese, indicative of a lower overall amount of silicon. In Figure 4.1(b), the light regions represent pearlite, while the dark regions represent ferrite.

EDS results are summarized in Table 4.1. Average manganese and silicon contents, in weight percent, between all wheel components, were 1.23 wt% and 0.49 wt%, respectively. These values both fall within allowable alloying element ranges for Q345, included in Table 2.2. Three instances of silicon content measurements were found to exceed the allowable amount in Q345 and are in bold text. These amounts do not significantly exceed the maximum allowable Silicon content of the alloy, and are likely attributable to some non-uniformity in the material composition. Additionally, errors introduced from EDS analysis of the low silicon energy peaks may also have contributed to the overly high silicon values.

Table 4.1: EDS analysis of all components of a five-piece mining wheel with corrections made to include a nominal carbon content of 0.2 wt%

Wheel Component	Percent	Alloying Element			
		Iron	Manganese	Silicon	Carbon
BS Band	Weight Percent	98.04	1.25	0.51	0.20
	Atomic Percent	96.83	1.26	1.00	0.91
Gutter	Weight Percent	97.76	1.45	0.60	0.20
	Atomic Percent	96.46	1.45	1.17	0.91
Flange	Weight Percent	98.37	1.07	0.37	0.20
	Atomic Percent	97.29	1.08	0.72	0.91
Lock Ring	Weight Percent	98.24	1.11	0.44	0.20
	Atomic Percent	97.10	1.12	0.87	0.91
Rim Base	Weight Percent	97.99	1.25	0.56	0.20
	Atomic Percent	96.74	1.26	1.09	0.91
Average	Weight Percent	98.08	1.23	0.49	0.20
	Atomic Percent	96.89	1.23	0.97	0.91

4.2. Corrosion Behaviour

Accelerated corrosion testing was conducted on tensile and fatigue samples extracted from the BS Band, Lock Ring, Gutter, and Flange of a five-piece wheel assembly. The purpose was to induce onto all specimens a level of mass-loss and surface

corrosion representative of the long term corrosion in a mining environment. To verify that the level of corrosion was similar to a mining environment, mass-loss and surface roughness measurements of a sample group of fatigue specimens were recorded and compared with historical corrosion data.

4.2.1. Mass-Loss

Mass-loss based accelerated corrosion testing was conducted on tensile and fatigue specimens extracted from the BS Band, Lock Ring, Gutter, and Flange of a five-piece mining wheel assembly. Rim Base specimens were not subjected to corrosion testing due to a lack of specimen availability. Furthermore, EDS, microstructural, hardness, and tensile testing of as-extracted Rim Base specimens showed the material behaviour to be consistent with other components; thus tensile and fatigue testing in the pre-corroded condition was not necessary.

The mass-loss of two fatigue specimens per wheel component was recorded over the duration of submerged corrosion testing. Results from mass-loss tracking are included in Figure 4.2. The average mass-loss of the two tracked fatigue specimens for each wheel condition was used for plotting purposes. In Figure 4.2, mass-loss is displayed as percent mass-loss, which was calculated using Equation (4.1). As can be seen from Figure 4.2, mass-loss measurements are consistent for the Flange, BS Band and Gutter. Mass-loss measurements are higher for the Lock Ring, with an increase in percent mass-loss of approximately 41% relative to the BS Band after 30 days of submerged corrosion testing, calculated using Equation (4.1).

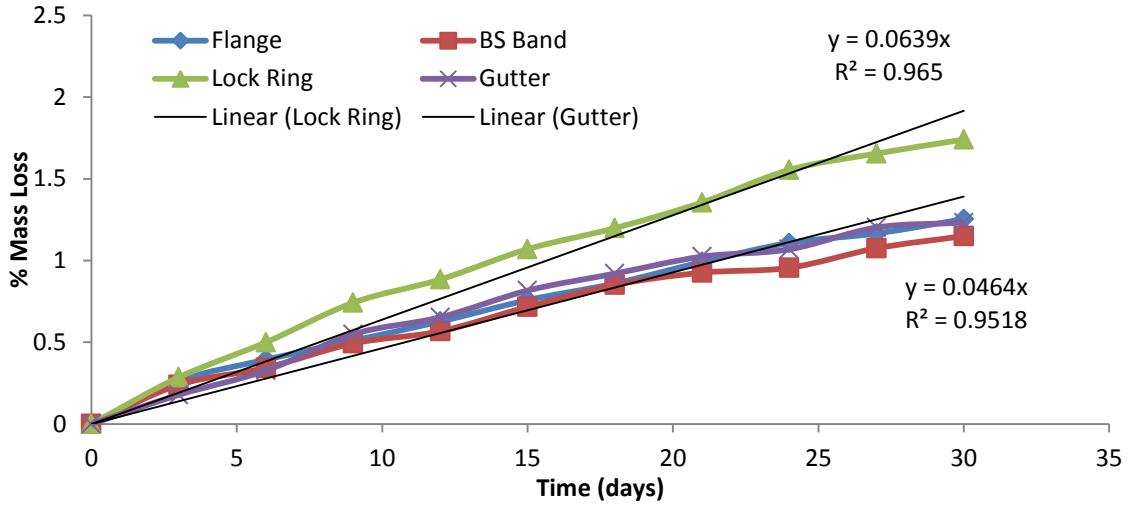


Figure 4.2: Percent mass-loss over time of fatigue specimens submerged in 3.5 wt% NaCl solution

The Lock Ring percent mass-loss increase was calculated using (4.1). This equation was used to evaluate various differences in mechanical and material performance throughout the remainder of Chapter 4. In (4.1), A represents a numeric value and B represents the numeric value for which A is being compared against.

$$\text{Percent Difference} = \left(\frac{(A - B)}{B} \right) \times 100\% \quad (4.1)$$

From Figure 4.2 it can be seen that the percent mass-loss corrosion behaviour over time for material extracted from all wheel components is approximately linear. If a linear fit through the intercept is included for the Lock Ring corrosion performance and the Gutter corrosion performance, their slopes are 0.0639 and 0.0464, respectively, measured in percent mass-loss per day. These fits have correlation coefficients of 0.965 and 0.952, respectively, which is indicative of a strong linear correlation between time and percent mass loss.

To compare the mass-loss of Q345 under fully submerged corrosion testing with data in the literature, Equation (3.2) was used. In this equation, mass-loss is calculated as the difference in initial and final specimen mass divided by specimen surface area. This method of reporting mass loss is commonly used in the literature for corrosion tracking. Figure 4.2 is re-plotted as Figure 4.3, using Equation (3.2). In Figure 4.3 it can be seen that the surface area mass-loss (SAML) rates as a function of hours for the Lock Ring and Gutter regions are 0.0402 and 0.0281, respectively, measured in $\text{mg}\cdot\text{cm}^{-2}\cdot\text{hrs}^{-1}$. Converted to days, these rates become 0.9648 and 0.6744, respectively, measured in units of $\text{mg}\cdot\text{cm}^{-2}\cdot\text{day}^{-1}$.

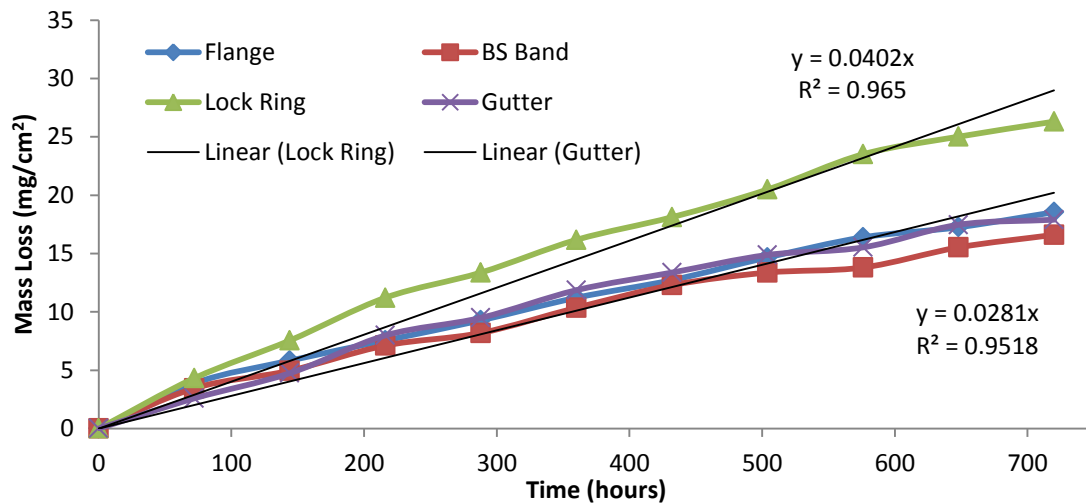


Figure 4.3: Surface area mass-loss over time of fatigue specimens submerged in 3.5 wt% NaCl solution

In the study of [57], a SAML of the Q345 alloy was reported as $12.5 \text{ mg}\cdot\text{cm}^{-2}$ after 480 hours of testing. In their work, a 5 wt% NaCl solution was used in cyclic accelerated wet/dry corrosion testing. From Figure 4.3 it can be seen that most wheel components had this degree of SAML after approximately 400 hours of testing, while the Lock Ring experienced this degree of SAML after approximately 250 hours. This

observation indicates that fully submerged corrosion testing in a 3.5 wt% NaCl solution had a similar, if not slightly more aggressive effect on the SAML corrosion of the Q345 alloy.

Some surface area mass-loss measurements of mild steels in mining environments are summarized in section 2.4.1 and Appendix A. Converted to units of $\text{mg}\cdot\text{cm}^{-2}$, a select range of aggressive rates of corrosion reported in the literature ranged from $4.31\cdot 10^{-1} \text{ mg}\cdot\text{cm}^{-2}\cdot\text{day}^{-1}$ [38] to $9.15\cdot 10^{-1} \text{ mg}\cdot\text{cm}^{-2}\cdot\text{day}^{-1}$ [39] for mild steel, for different gold mine environments. The SAML rate for the gutter in this study was $6.74\cdot 10^{-1} \text{ mg}\cdot\text{cm}^{-2}\cdot\text{day}^{-1}$. This rate falls between the two rates previously stated. In 30 days of testing, the surface area mass-loss corrosion for the gutter was approximately $17.89 \text{ mg}\cdot\text{cm}^{-2}$. It would take 42 days and 20 days, respectively, for the same level of surface-area mass-loss to occur using the corrosion rates of $4.31\cdot 10^{-1} \text{ mg}\cdot\text{cm}^{-2}\cdot\text{day}^{-1}$ [38] and $9.15\cdot 10^{-1} \text{ mg}\cdot\text{cm}^{-2}\cdot\text{day}^{-1}$ [39], for mild steel. The corrosion testing in this study reflects normal rates of corrosion for some aggressive mining environments, despite being considered accelerated. Of course, these aggressive corrosion rates might not reflect those of wheel components or other structural members in a mine, which are normally equipped with superficial coatings (e.g. paint) and are maintained somewhat regularly.

The high rates of corrosion in some mines are likely attributable to lower pH, higher humidity, the presence of sulfur, and the synergistic effects of wear and corrosion, none of which were simulated in the corrosion testing in this study. Nevertheless, the rates of corrosion in this study were similar to those of some mining conditions. Furthermore, the submerged corrosion testing in this study was shown to be reflective of

cyclic wet/dry corrosion testing, which is a better representation of the mining environment. Thus, it can be stated with some degree of confidence that the fully submerged corrosion testing in this study was fairly representative of the corrosion conditions in a mining environment, at least, from a mass-loss perspective. Additionally, mining wheels likely corrode at a slower rate than the rates of uncoated mild steels discussed in the literature, and so it is not unrealistic to consider the corrosion testing in this study to be somewhat aggressive relative to normal mining wheel corrosion rates. A summary of various corrosion rates and values discussed throughout this section is included in Table 4.2.

Table 4.2: Summary of surface area mass-loss corrosion data discussed in 4.2.1

	Gutter	Lock Ring	[38]	[39]
Surface Area Mass-Loss Rate ($\text{mg}\cdot\text{cm}^{-2}\cdot\text{day}^{-1}$)	0.674	0.964	0.431	0.915
30 Day Surface Area Mass-Loss ($\text{mg}\cdot\text{cm}^{-2}$)	17.890	26.304	12.930	27.450

4.2.2. Surface Roughness

Following mass-loss corrosion testing, fatigue and tensile specimens were periodically re-exposed to the corrosion solution. The purpose was to generate a level of surface corrosion onto the specimens similar to the level of surface corrosion on in-service wheel components. To verify that specimen surface corrosion was consistent with in-service wheel components, surface roughness measurements were taken of sample fatigue specimens, and worn wheel components.

Figure 4.4 shows the surface roughness profile of a pre-corroded fatigue specimen, while Figure 4.5 shows the surface roughness profile of an in-service wheel

component. From the two figures, it can be seen that the two roughness profiles are of the same magnitude. Furthermore, qualitatively, the two profiles have similar shapes.

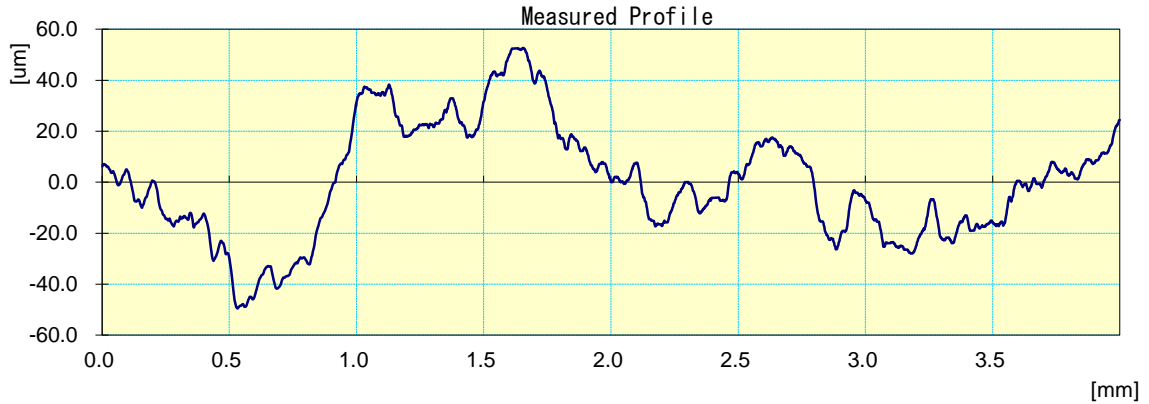


Figure 4.4: Surface roughness profile of pre-corroded fatigue specimen

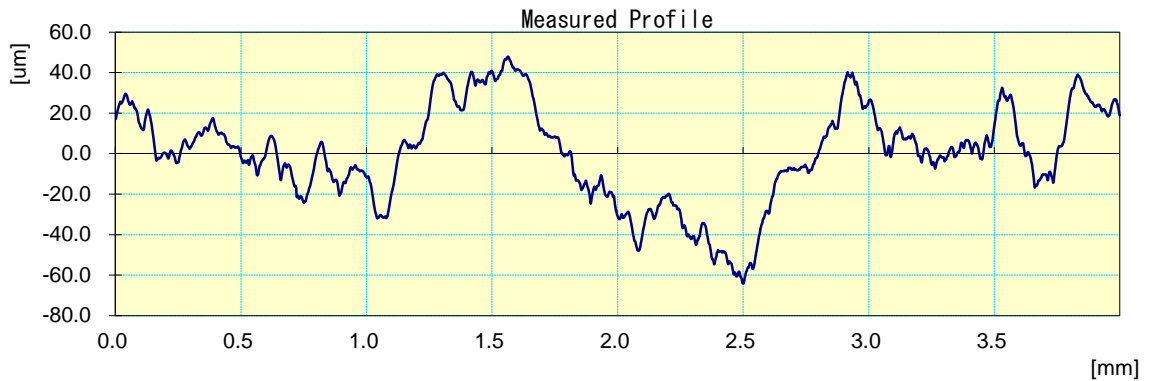


Figure 4.5: Surface roughness profile of in-service corroded wheel component

The R_a roughness value of the sample pre-corroded fatigue specimen was $14.73 \mu\text{m}$, while the R_z was $85.40 \mu\text{m}$. Measured roughness values for other pre-corroded sample specimens were consistent in magnitude with these measurements, but some variation was present due to the nature of the corrosion process. The R_a roughness value of the used wheel component was $16.59 \mu\text{m}$, while the R_z value of the used wheel component was $98.49 \mu\text{m}$.

From roughness values of the sample pre-corroded fatigue specimen and used wheel component, it can be seen that R_a and R_z values of the worn wheel component are 12.6% and 15.3% higher, respectively, calculated using Equation (4.1). While these values are higher, they are of the same order of magnitude as the pre-corroded specimen. Furthermore, these roughness values are much higher than the R_a roughness of as extracted fatigue specimens, maintained as $0.4 \mu\text{m}$ or lower (section 3.7.1). Therefore, the surface condition of pre-corroded specimens can be stated to be representative of in-service wheel components, as measured using the criterion of surface roughness. It is expected that this level of surface corrosion would greatly reduce the high-cycle fatigue behaviour of the pre-corroded specimens, relative to fatigue specimens in the as-extracted condition.

Surface roughness measurements were also taken of new wheel components. A sample roughness profile taken from a new painted flange is presented in Figure 4.6. From the profile, it can be seen that the roughness measurements range from approximately $-3.0 \mu\text{m}$ to $3.0 \mu\text{m}$. In contrast, worn wheel and pre-corroded specimen roughness measurements ranged in values from approximately $-60.0 \mu\text{m}$ to $60.0 \mu\text{m}$ as shown in Figure 4.4 and Figure 4.5. The new wheel roughness range is approximately 20 times lower than that of the measured worn wheel, and is representative of the overall degradation that occurs to in service wheels exposed to wear and corrosion. This degradation in surface roughness is detrimental to the high-cycle fatigue behaviour of wheels, as discussed in section 2.2. The R_a and R_z roughness values for the new wheel profile of Figure 4.6 are $1.02 \mu\text{m}$ and $4.67 \mu\text{m}$, respectively. A summary of all roughness values discussed in this section is included in Table 4.3.

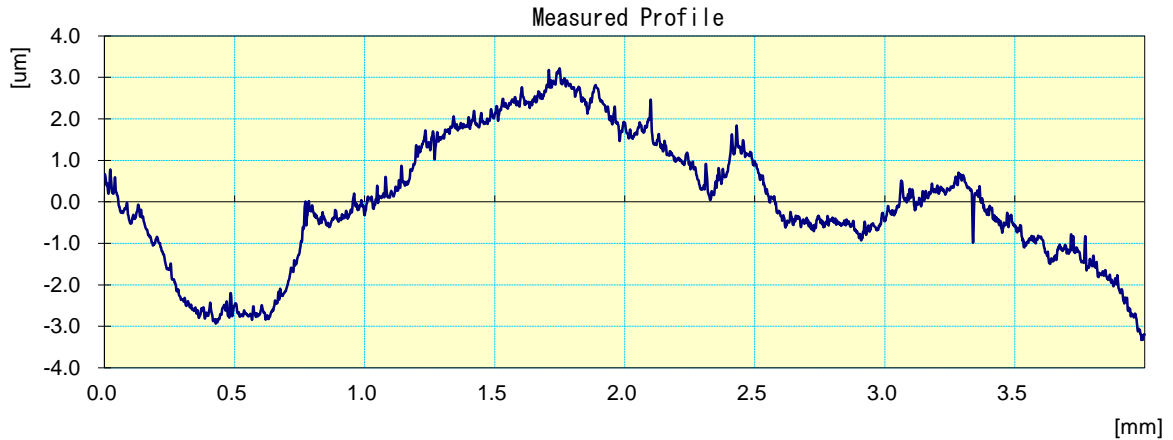


Figure 4.6: Roughness profile of new painted flange

Table 4.3: Summary of surface roughness measurements of a sample pre-corroded specimen, a sample worn wheel component, and a sample new wheel component

	Pre-Corroded Fatigue Specimen	Worn Wheel Component	New Wheel Component
Ra (µm)	14.73	16.59	1.02
Rz (µm)	85.40	98.49	4.67

4.3. Microstructure

Optical microscopy and SEM analysis was conducted to evaluate microstructural variations between different wheel components. Results from this analysis were used to facilitate development of a fatigue testing matrix. Further, knowledge of variations in wheel component microstructures was used to assist in explanation of discrepancies in wheel components observed in other testing schemes.

Low and high magnification micrographs taken from material samples of each component are included in Figure 4.7 - Figure 4.11. In each figure, colour micrographs are included, as well as black and white micrographs. The black and white micrographs were used to evaluate area fractions of ferrite and pearlite in each microstructure.

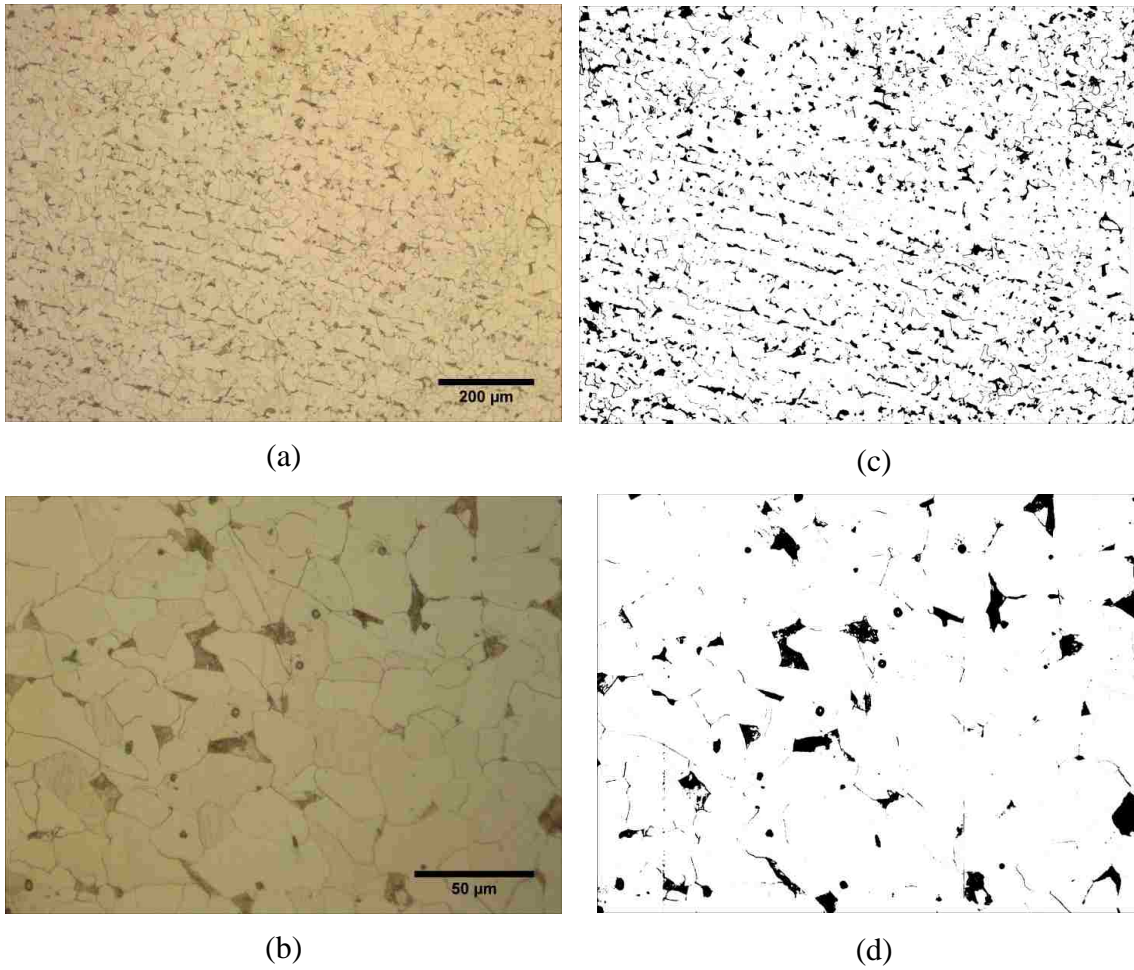


Figure 4.7: Micrographs of Rim Base at (a) 100x, (b) 500x, and in binary at (c) 100x, (d) 500x

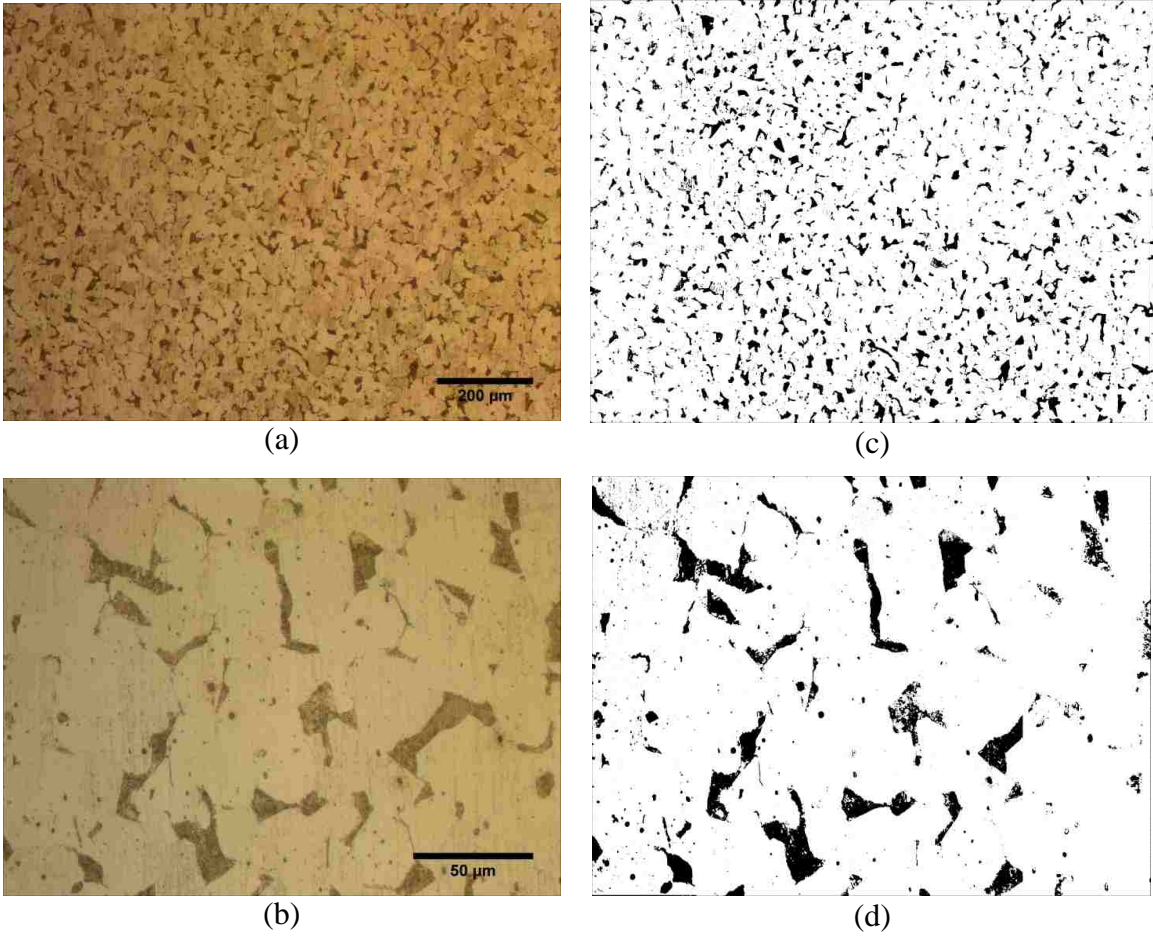


Figure 4.8: Micrographs of BS Band at (a) 100x, (b) 500x, and in binary at (c) 100x, (d) 500x

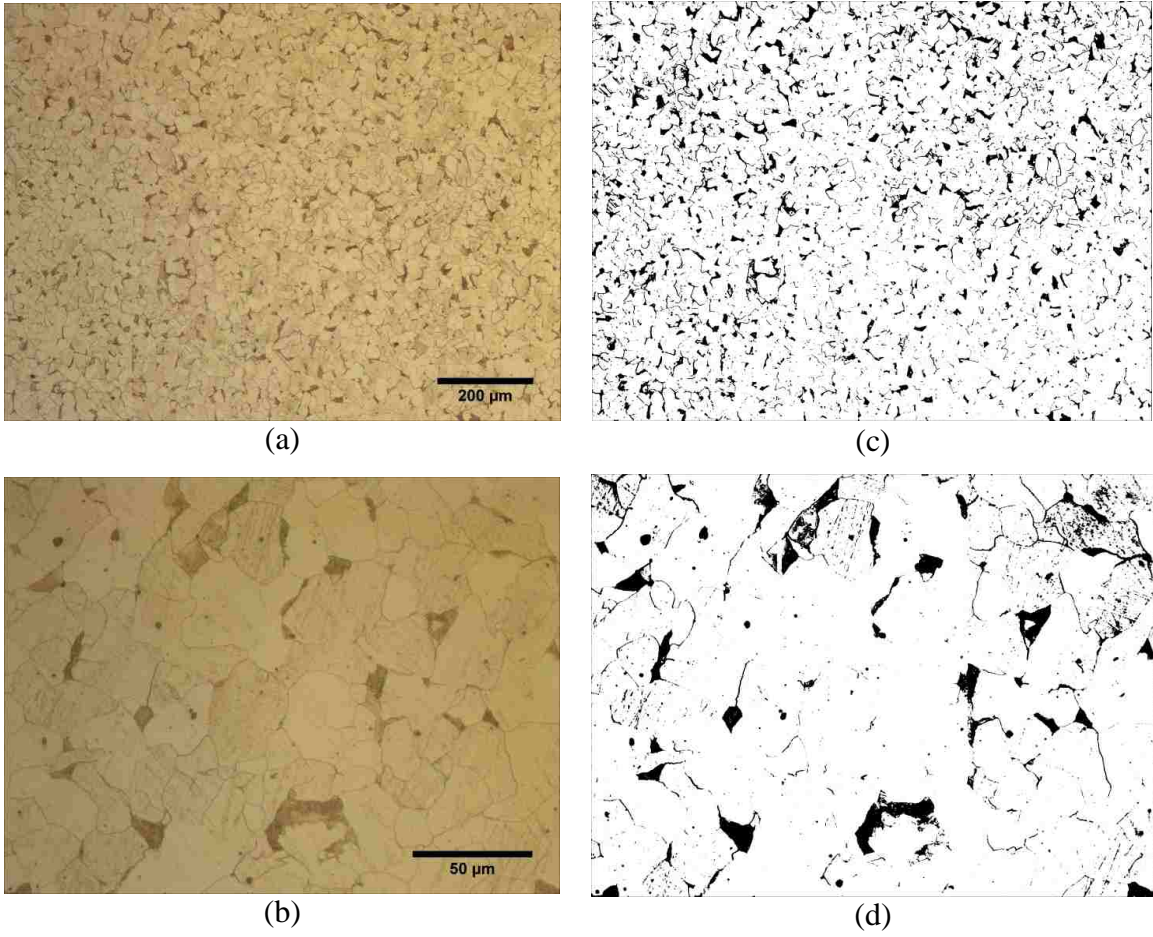


Figure 4.9: Micrographs of Flange at (a) 100x, (b) 500x, and in binary at (c) 100x, (d) 500x

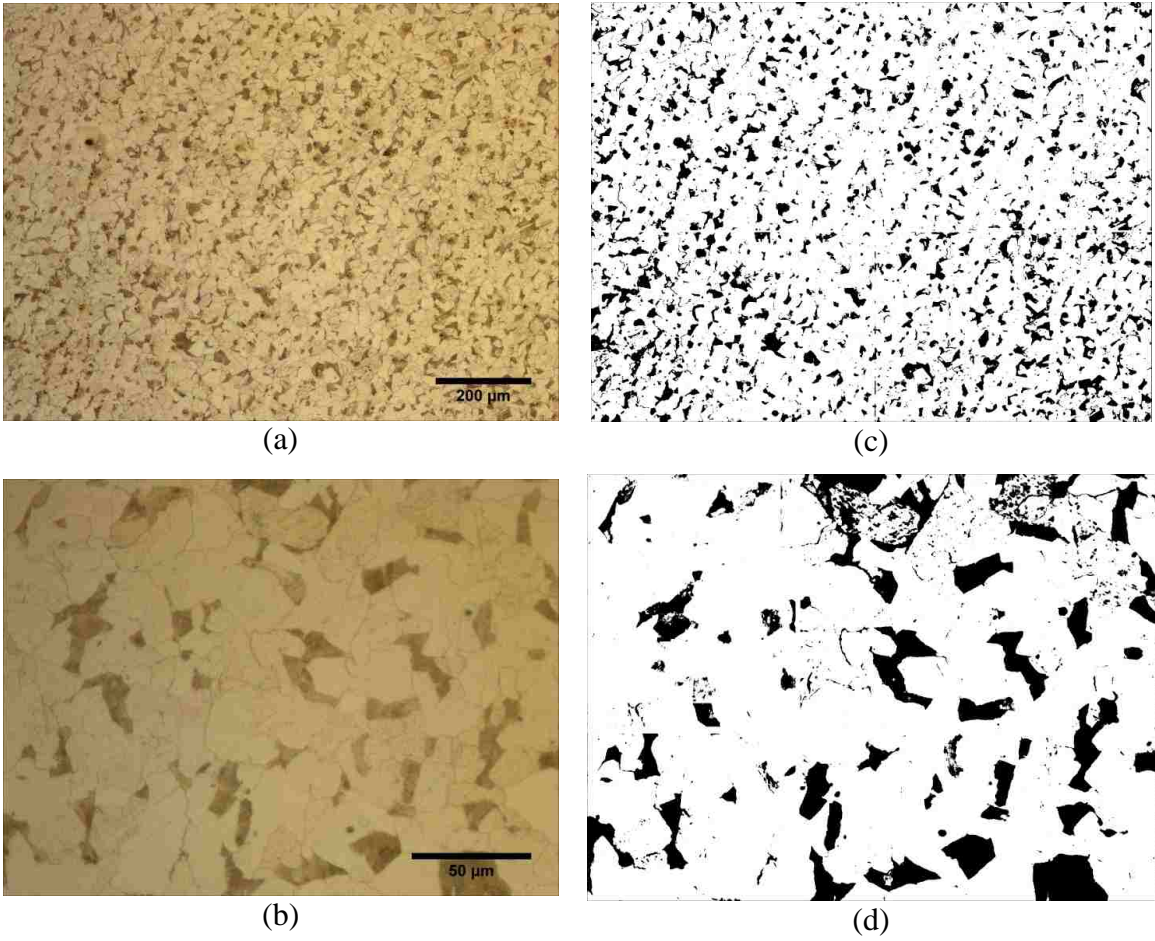


Figure 4.10: Micrographs of Gutter at (a) 100x, (b) 500x, and in binary at (c) 100x, (d) 500x

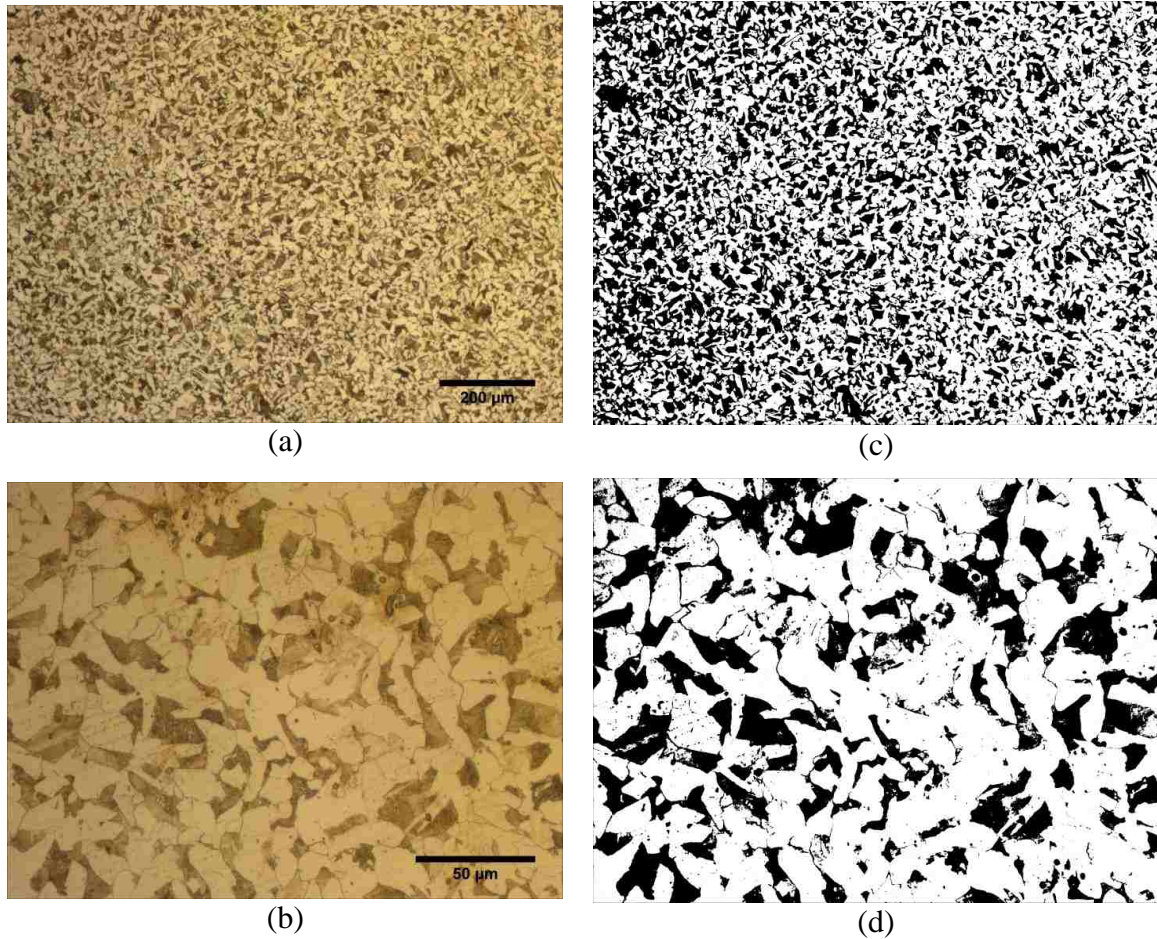


Figure 4.11: Micrographs of Lock Ring at (a) 100x, (b) 500x, and in binary at (c) 100x, (d) 500x

In the component micrographs, it can be seen that all microstructures are composed of two constituents, characterized by the light and dark areas. Visually, the light areas in all micrographs appear to occupy a larger portion of the component microstructures. These areas represent the alpha-iron phase, ferrite. This phase is characterized as relatively soft and ductile, and is the primary phase in most low carbon steels, such as the Q345 alloy.

From the literature [52] - [54], the Q345 alloy is expected to consist primarily of ferrite and pearlite. Therefore, it was suspected that the dark regions of the micrographs, which could not be resolved using optical microscopy, were pearlite. Before moving

forward in the analysis of the micrographs, the material samples were observed under high magnification using a scanning electron microscope to verify the microstructure of the dark regions.

Figure 4.12 shows the Lock Ring sample evaluated under low and high magnifications using a scanning electron microscope. From the high magnification SEM micrographs, it can be seen that the unresolved consist of a lamellar (layered) type microstructure. This is the typical microstructure of pearlite. The layers are thin phases of ferrite, and cementite, the two phases present in low-carbon steels. The pearlite microstructure is much stronger and harder than the ferrite phase. This strength increase is attributable to the presence of the hard cementite phase, and the small layer spacing. The presence of pearlite in steel should improve yield and UTS properties, but reduce ductility. The presence of pearlite in the microstructure is consistent with the work of other microstructural studies of the Q345 alloy [52] - [54]. SEM analysis conducted on other wheel components also found the unresolved regions to be pearlite; however, micrographs of these components have been omitted to avoid repetition.

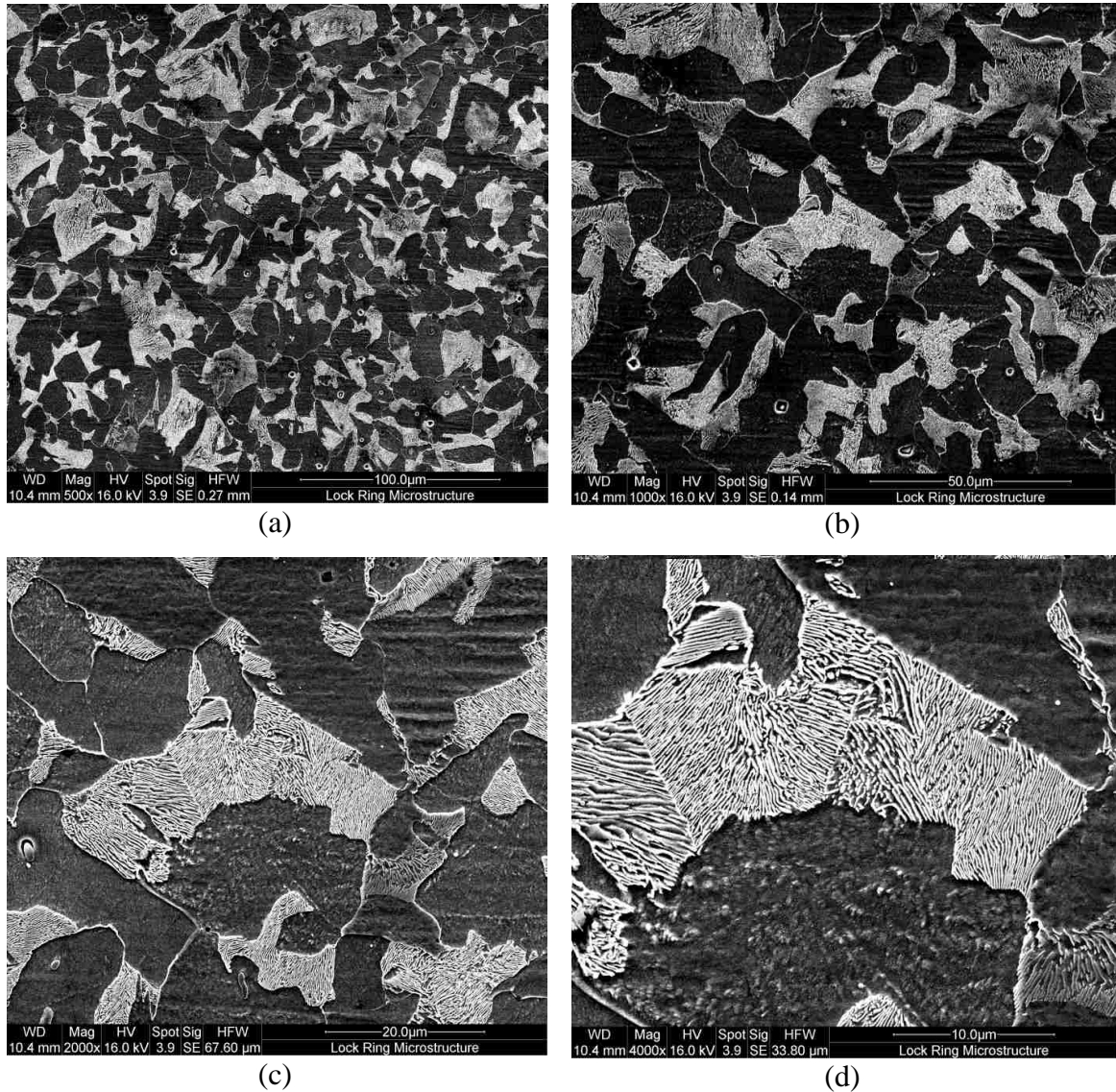


Figure 4.12: SEM micrographs of Lock Ring (a) 500x, (b) 1000x, (c) 2000x, and (d) 4000x

All wheel components have similar microstructures, consisting primarily of ferrite, with pearlite colonies dispersed throughout the microstructure. It can be visually observed that there are differences in pearlite concentrations between wheel components, notably for the Lock Ring. These differences can lead to variations in mechanical properties. Thus, area fractions of ferrite and pearlite were calculated from the low and high magnification optical micrographs.

Table 4.4 summarizes pearlite area fraction results for all microstructures. From the 100x magnification data, it can be seen that the Rim Base, BS Band, and Flange have fairly consistent pearlite levels, with values of 8.53%, 9.26%, and 10.24%, respectively. The Gutter region had a pearlite area fraction of 14.92%, while the Lock Ring had a pearlite area fraction of 41.06%. The elevated level of pearlite in the Lock Ring indicates that this component experienced higher rates of cooling, or some degree of forming. Higher levels of pearlite in the Lock Ring correlate with the higher levels of mass-loss in Lock Ring specimens, observed in section 4.2.1. These results are consistent with the literature, which showed that the pearlite microstructure will preferentially corrode over the ferrite phase in 16Mn steel [58].

Table 4.4: Summary of wheel component microstructure pearlite area fractions

Magnification	Microstructure	Rim Base	BS Band	Flange	Gutter	Lock Ring
100x	Percent Ferrite (%)	91.47	90.74	89.76	85.08	58.94
	Percent Pearlite (%)	8.53	9.26	10.24	14.92	41.06

The Lock Ring is the smallest wheel component in terms of mass and cross-sectional geometry. This, in turn, means it has the lowest thermal inertia of all wheel components. Therefore, under identical cooling conditions, the Lock Ring should cool the fastest and, in turn, have the highest pearlite content. From a mechanical standpoint, the Lock Ring must have a spring-like quality, since it is used to stretch around other components and act as an engaging mechanism. Since pearlite acts to improve spring-like behaviour by increasing strength and reducing ductility, higher levels of pearlite are expected to be present in the Lock Ring.

In summary, the Lock Ring should have consistently higher tensile properties relative to other wheel components, due to the higher pearlite levels within the Lock Ring microstructure. Similarly, the Lock Ring should have the highest average hardness of all wheel components. The Rim Base, Flange, and BS Band should display similar mechanical properties, while the Gutter may be somewhere between the Lock Ring and other wheel components.

The effect of pearlite content on the high-cycle fatigue behaviour of the Lock Ring cannot be determined from microstructure alone; however, no significant differences from the other wheel components are expected. In the high-cycle regime, crack initiation is the dominant mechanism which governs fatigue life. In this regime, cracks initiate and propagate at ferrite grains due to their lower strength. Given that all wheel component microstructures consist of a base ferrite matrix, crack initiation and propagation should not be strongly controlled by pearlite content. Therefore, despite the higher levels of pearlite in the Lock Ring, the presence of ferrite should control the high-cycle fatigue behaviour of the Q345 alloy.

4.4. Cross-Sectional Hardness

Cross-sectional hardness measurements were taken of each wheel component. Measurements were taken from one free surface of the component to the other free surface. Figure 4.13 contains an example illustration of a specimen being tested, with the dotted line representing hardness measurements.

The purpose of hardness testing was to evaluate how hardness varies as a function of component depth. This information was helpful in confirming that tensile and fatigue specimens were representative of actual component behaviour. Specimens were

generally not extracted near component surfaces due to machining constraints, and so variations in hardness would potentially require corrections to fatigue results.

Results from cross-sectional hardness testing are plotted in Figure 4.13. All hardness values are in the Rockwell B Hardness scale. From Figure 4.13, it can be seen that the Flange, BS Band, Rim Base, and Lock Ring show no significant variations in hardness across their thickness. The Gutter had variations in cross-sectional hardness, with surface hardness readings being more consistent with Lock Ring measurements, and core hardness readings being more consistent with Flange measurements.

Similar trends in Gutter region hardness were also reported in the work of Zhang & Fleek [11], discussed in section 2.1.2. In their work, surface hardness readings were near 99 HRB, consistent with the findings of the present hardness testing (~97 HRB). Conversely, core hardness readings in their work were near 90 HRB, while core hardness readings of the Gutter in this study were closer to 80 HRB, as shown in Figure 4.13. Overall, variations in Gutter region hardness are indicative that fatigue and tensile specimens will be more representative of the Gutter core than the Gutter surface.

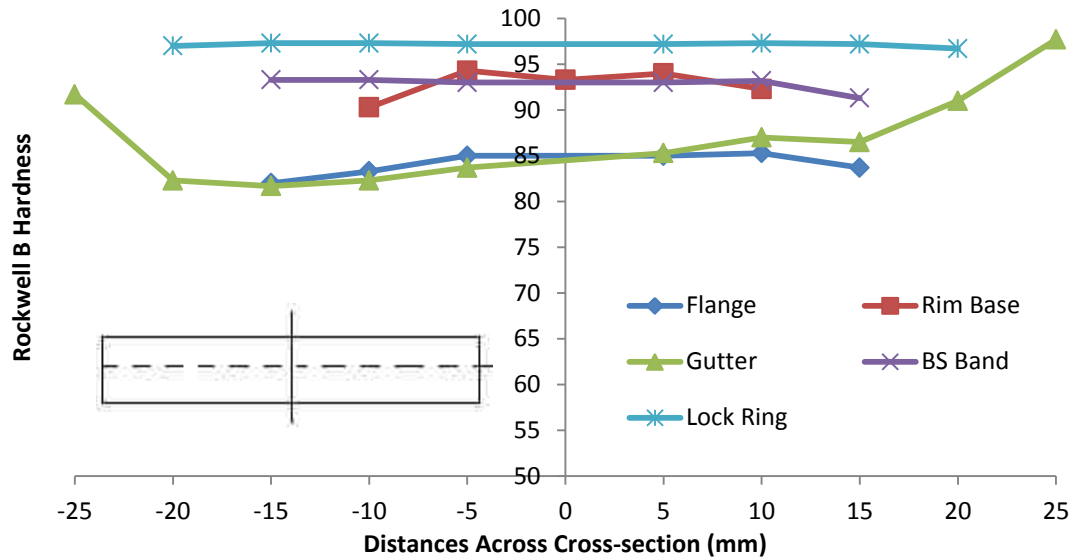


Figure 4.13: Component HRB hardness as a function of depth

The average hardness was calculated for all components with hardness readings that did not vary as a function of measurement depth. Average hardness values were 97.15 HRB, 92.85 HRB, 92.84 HRB and 84.05 HRB, for the Lock Ring, BS Band, Rim Base, and Flange, respectively. Standard deviations for these measurements were ± 0.21 HRB, ± 0.77 HRB, ± 1.62 HRB, and 1.28 HRB, respectively. For the Gutter region, an average core hardness of 84.11 HRB was calculated, as well as an average surface hardness of approximately 93.47 HRB. Respective standard deviations of Gutter hardness values were ± 2.16 HRB and ± 3.68 HRB. These values are summarized in Table 4.5.

Table 4.5: Summary of average HRB hardness measurements of five-piece wheel components

	Flange	Base	Gutter Core	Gutter Surface	BS Band	Lock Ring
Average Hardness (HRB)	84.05	92.84	84.11	93.47	92.85	97.15
Standard Deviation Hardness (HRB)	1.28	1.61	2.16	3.68	0.77	0.21

From Table 4.5 it is apparent that the Lock Ring has a significantly higher average hardness than other wheel components. This finding is consistent with microstructural observations, in which Lock Ring samples had increased levels of pearlite, which acts to harden the microstructure.

4.5. Tensile Properties

Quasi-static tensile testing was conducted on tensile specimens in the as-extracted and pre-corroded conditions. Testing was done for specimens extracted from all wheel components in the as-extracted condition, and all components except the Rim Base in the pre-corroded condition. Rim Base specimens were not tested in the pre-corroded condition due to a lack of specimen availability. Other experimental observations have shown that no significant differences in tensile behaviour should exist between the Rim Base and the Flange and BS Band components. Thus, testing of the Rim Base in the pre-corroded condition was also not necessary.

The primary purpose of the testing was to determine the yield strength and the ultimate tensile strength of material from all wheel components. This information would later be used within the project research group to facilitate numerical modelling and fatigue life analysis of multi-piece wheels. All tensile properties discussed throughout this section refer to engineering stress-strain properties, unless otherwise stated.

The mean and range of 0.2% offset yield strength and UTS results for all wheel specimens tested in the as-extracted condition are summarized in Table 4.6. The Lock Ring had an average yield strength of 681.5 MPa, and an average UTS of 779.8 MPa. In contrast, other wheel components had average yield strengths ranging from 373.2 MPa to 482.4 MPa, and average ultimate tensile strengths ranging from 470.7 MPa to 544.1 MPa.

Lock Ring tensile properties are consistent with microstructural and hardness results, which qualitatively found the Lock Ring would exhibit superior mechanical performance relative to other wheel components. Overall, YS and UTS values from tensile testing of all as-extracted wheel samples meet or exceed minimum requirements of ASTM A572 [49], and are consistent with the literature.

Table 4.6: Mean and range YS and UTS values of specimens in the as extracted condition

	Rim Base	BS Band	Flange	Gutter	Lock Ring
Mean 0.2% Offset Yield Strength (MPa)	373.2	467.9	482.4	379.7	681.5
0.2% Offset Yield Strength Range (MPa)	355.2-391.4	467.9	449.6-515.1	361.7-406.9	679.2-683.8
Mean UTS (MPa)	470.7	531.7	544.1	520.2	779.8
UTS Range (MPa)	461.6-480.7	531.7	527.9-560.3	487.6-571.5	773.6-785.9

Yield strength and UTS for all wheel components in the as-extracted condition are plotted in Figure 4.14 as a function of pearlite content. From Figure 4.14 it can be seen that YS and UTS for the Rim Base, BS Band, Flange, and Gutter are reasonably consistent with their microstructural area fractions of pearlite. The Lock Ring shows the same trend, with elevated YS and UTS values consistent with the high microstructural area fraction of pearlite in the Lock Ring. In general, a linear trend was found to exist between pearlite content and YS, and pearlite content and UTS. YS and UTS trends had slopes of $7.94 \text{ MPa}\cdot\%P^{-1}$ and $8.50 \text{ MPa}\cdot\%P^{-1}$, respectively; however, their intercepts were shifted relative to each other along the stress-axis, with values of 343.57 MPa and 426.48 MPa, respectively. Correlation coefficients for the two fits were 0.77 and 0.94, respectively. Thus, it can be said with a certain degree of confidence that the ultimate tensile strength of the Q345 alloy, extracted from all wheel components, has a linear

relationship with the pearlite content in the alloy, for the ranges observed in this work. To verify if this relationship is truly linear, a wider range of pearlite contents should be examined in future work. The tensile properties of pearlite fractions between extreme values should also be evaluated.

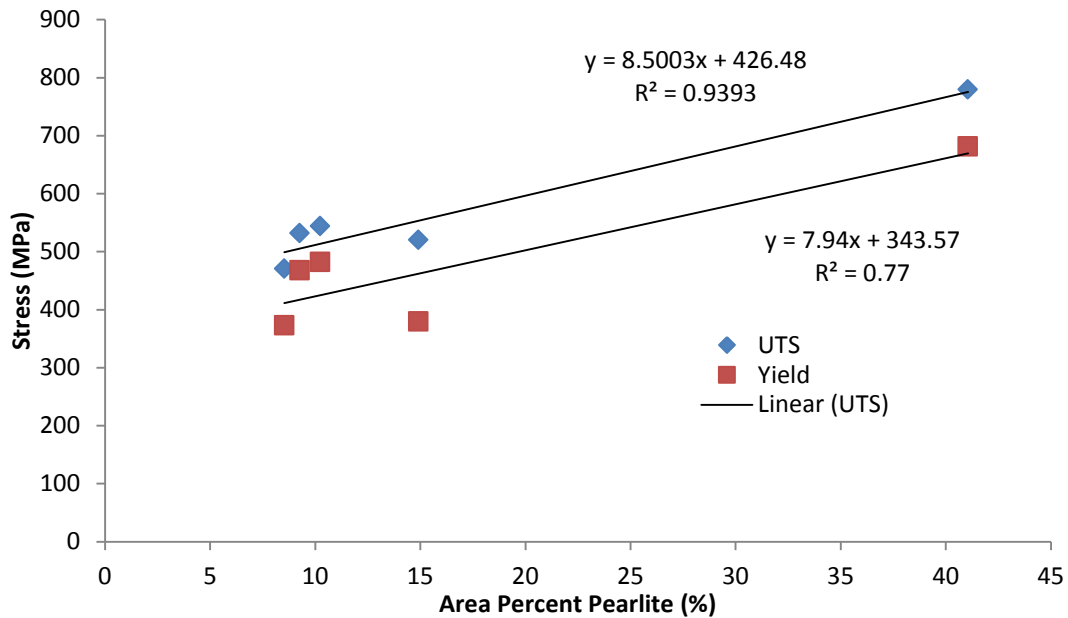


Figure 4.14: Yield strength and ultimate tensile strength as a function of pearlite content for as-extracted wheel component tensile testing

Figure 4.15 shows sample engineering stress-strain curves from tensile testing of Lock Ring and Gutter specimens in the as extracted condition. The curves graphically illustrate differences in yield and tensile properties previously discussed. Moreover, they show the effect of pearlite content on maximum percent elongation before failure. As can be seen, the Lock Ring, with a high pearlite content, has a maximum percent elongation of only 18%, while the Gutter, with a lower pearlite content, has a maximum percent elongation of approximately 23.5%. A decrease in percent elongation as a function of pearlite content is common in low carbon steel when no other strengthening

mechanisms are considered. At low pearlite contents, the ductile alpha-iron phase, ferrite, is the primary phase which controls mechanical properties of low carbon steels.

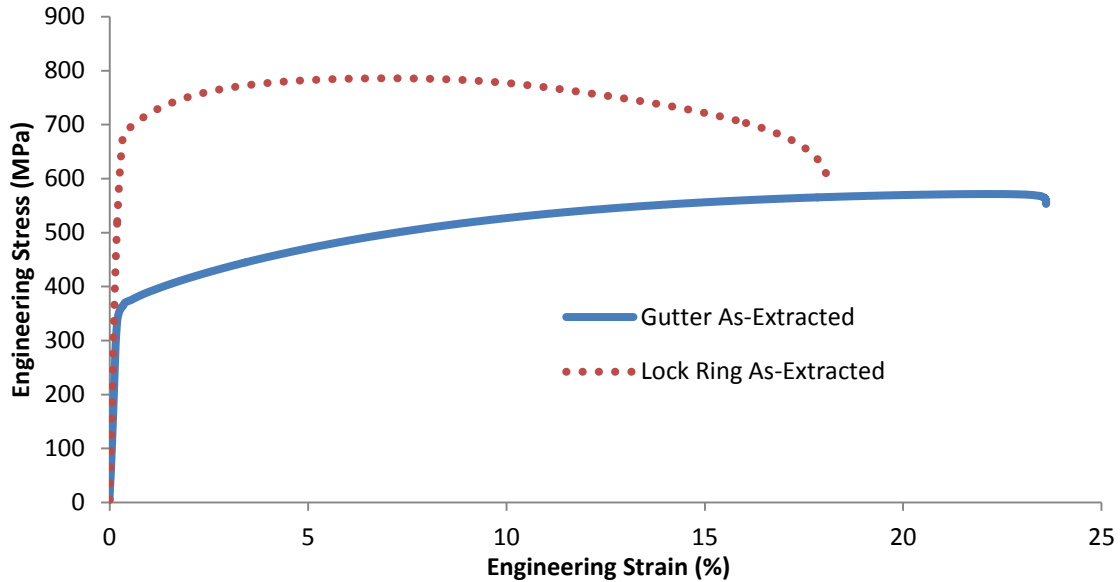


Figure 4.15: Engineering stress-strain behaviour of as-extracted specimens from the Lock Ring and the Gutter

A summary of yield strength and ultimate tensile strength data from quasi-static tensile testing of pre-corroded specimens is included in Table 4.7. It can be seen that the Lock Ring in the pre-corroded condition has a YS of 639.4 MPa, and a UTS of 752 MPa. Other wheel components have similar average YS and UTS relative to each other, with values ranging from 381.8 to 472.3 MPa, and 459.6 to 520.6 MPa, respectively. From these observations, it is evident that in the pre-corroded condition, wheel component specimens maintain similar trends to as-extracted specimens. Specifically, the Lock Ring demonstrates increased material strength relative to other wheel components, and all other wheel components have similar ultimate tensile strengths. These trends are, again, attributable to the greater amount of pearlite in the Lock Ring.

Table 4.7: Mean and range YS and UTS values of specimens in the pre-corroded condition

	BS Band	Flange	Gutter	Lock Ring
Mean 0.2% Offset Yield Strength (MPa)	472.3	416.6	381.8	639.4
0.2% Offset Yield Strength Range (MPa)	472.3	384.3-448.9	336.2-427.4	633.9-644.9
Mean UTS (MPa)	520.6	493.3	479.6	752.0
UTS Range (MPa)	520.6	458-528.6	461.1-498.2	740.5-763.6

To evaluate the effect of pre-corrosion on the yield strength and tensile strength of wheel component specimens, Equation (4.1) was used. With Equation (4.1), the percent difference in mean YS and mean UTS for wheel component specimens tested in both conditions was calculated. Results are summarized in Table 4.8. From Table 4.8 it can be seen that differences in YS and UTS between as-extracted and pre-corroded components were minimal, with only the Flange YS showing a decrease of over 10%. Nevertheless, all wheel components do show minor decreases in UTS in the pre-corroded condition.

The level of pre-corrosion generated through accelerated corrosion testing was primarily superficial, affecting only specimen surface topography. The changes induced in surface topography were expected to result in significant decreases in high-cycle fatigue performance, which has a strong dependence on surface condition. Conversely, in quasi-static tensile testing, surface roughness does not play a large role on tensile behaviour. Thus, the low differences in yield strength and ultimate tensile strength between as-extracted and pre-corroded specimens are not unexpected.

Table 4.8: Percent difference in YS and UTS of as-extracted and pre-corroded wheel specimens

	BS Band	Flange	Gutter	Lock Ring
Percent Difference in Mean YS (%)	0.94	-13.64	0.55	-6.18
Percent Difference in Mean UTS (%)	-2.09	-9.34	-7.80	-3.56

Included in Figure 4.16 are sample stress-strain curves of pre-corroded Lock Ring and Gutter specimens. Additionally, as-extracted stress-strain curves of the same components are included. The form of the pre-corroded Lock Ring stress-strain curve is an artifact of testing, in which specimen failure occurred very near the extensometer limit. Failures near extensometer limits or completely outside of the extensometer (outside of gauge region for measuring strain) were common for corrosion testing, due to the surface condition.

Pre-corroded stress-strain curves of the two components reflect the data presented in Table 4.7 and Table 4.8, showing minimal changes in YS and UTS values between the two specimen conditions. On the other hand, the pre-corroded Lock Ring specimen shows a decrease of 27% in total elongation before failure, while the pre-corroded Gutter specimen only shows a 7.6% decrease in total elongation. These decreases in total elongation may be associated with corrosion; however, they should not play a great role in fatigue performance, which has a stronger dependence on UTS than maximum percent elongation.

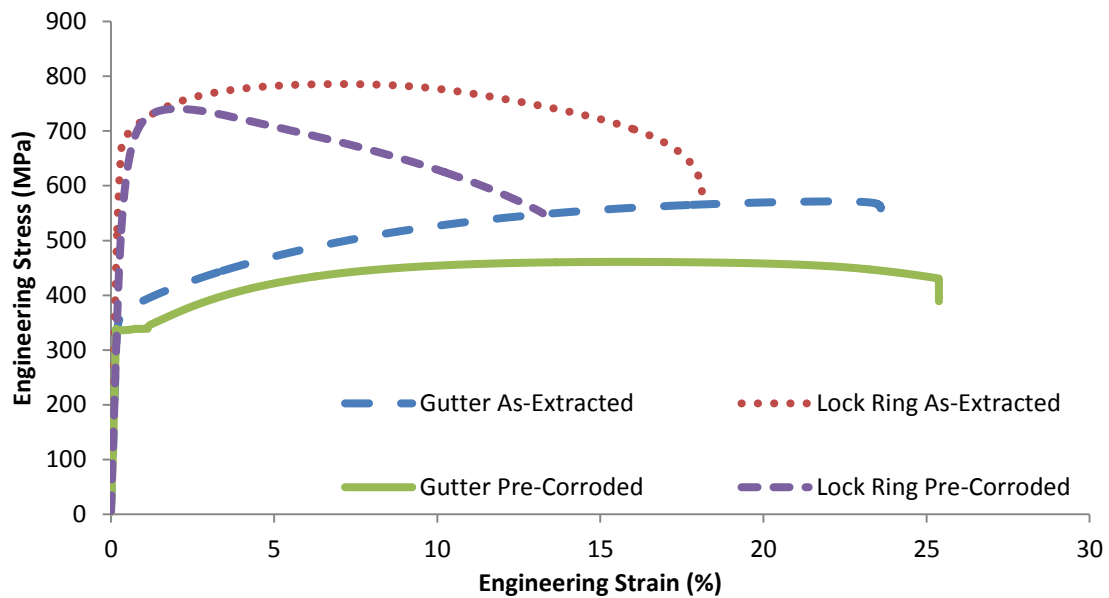


Figure 4.16: As-extracted and pre-corroded stress-strain curves of Lock Ring and Gutter specimens

4.6. Fatigue Properties

Stress-based fatigue testing was conducted on material samples extracted from a five-piece mining wheel assembly. Fatigue specimens were tested in the as-extracted and pre-corroded conditions. In the as-extracted condition, specimens from all wheel components were tested. In the pre-corroded condition, only Gutter and Lock Ring specimens were tested. This decision was made based on results from other experimental tests and observations from as-extracted fatigue testing, which showed little variation in high-cycle fatigue behaviour between components. Results from fatigue testing were used within the research group in the estimation of multi-piece wheel fatigue lives using numerical methods. Fracture analysis of select fatigue specimens was conducted to qualitatively evaluate fatigue behaviour for different test conditions, e.g., as-extracted versus pre-corroded.

4.6.1. As-Extracted Fatigue Behaviour

Results from fatigue testing of specimens in the as-extracted condition are plotted on an S-N curve, in Figure 4.17. The larger data points correspond to fatigue specimens that did not fail after 5,000,000 cycles or more, and provide a rough estimate of the endurance limit for each fatigue dataset.

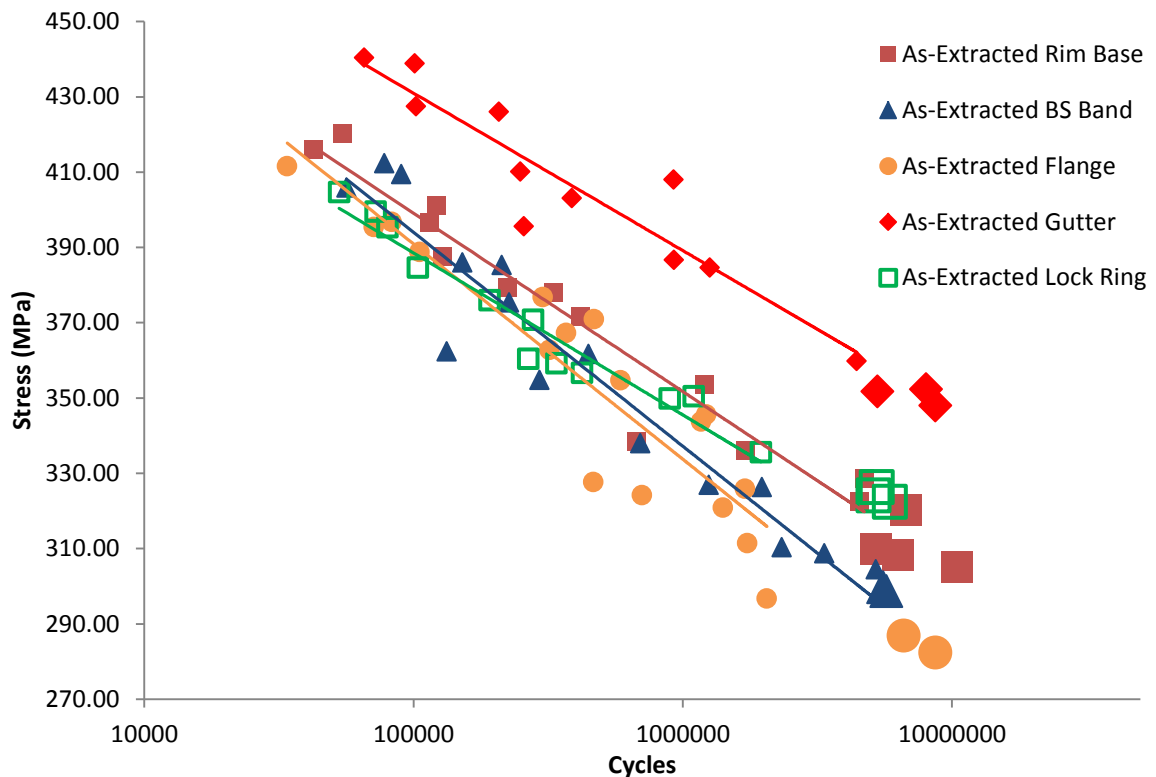


Figure 4.17: High-cycle fatigue behaviour of as-extracted specimens from all wheel components

All as-extracted S-N curves include a base 10 log-linear fit of the form of Equation (4.2), calculated using the principles of section 2.3.2. Slope (a_0) and intercept (a_1) values for each dataset are included in Table 4.9, which also includes stress values at failure cycles of 50,000 and 5,000,000. Failure cycle stress values were included to facilitate interpretation and comparison of fatigue dataset fits. Fits were calculated with

cycles as the dependent variable, despite being plotted as the independent variable, which is standard when generating S-N curves.

$$\log_{10} N = a_0 \times S + a_1 \quad (4.2)$$

Table 4.9: As-extracted fatigue dataset fit coefficients and statistical analysis values of each fit

	Rim Base	BS Band	Flange	Gutter	Lock Ring
Slope ($\log N \cdot \text{MPa}^{-1}$)	-0.0199	-0.0163	-0.0149	-0.0207	-0.0220
Intercept ($\log N$)	12.9634	11.4768	10.9265	14.0019	13.5854
Stress at 5,000,000 Cycles From Fit (MPa)	315.27	292.75	283.36	352.61	312.44
Stress at 50,000 Cycles From Fit (MPa)	415.92	415.30	417.42	449.17	403.18
F-Crit	4.84	4.67	4.54	5.12	4.96
F-Test	175.53	164.74	86.68	58.18	180.41
T-Crit	2.20	2.16	2.13	2.26	2.23
T-Slope	13.25	12.84	9.31	7.63	13.43
T-Intercept	23.19	25.09	19.17	12.64	22.32
Correlation Coefficient	0.94	0.93	0.85	0.87	0.95

Statistical analyses were conducted to verify the relevance of each as-extracted dataset fit. Verification procedures included F-Test, T-Test and correlation coefficient evaluation, as discussed in section 2.3.2. Results from these analyses are included in Table 4.9. F-Crit and T-Crit values were calculated using a 95% probability criterion. All F-Fit, T-Slope, and T-Intercept values for each dataset fit exceeded their respective F-crit and T-crit values. Thus, all fits and fit coefficients were considered statistically

relevant. Correlation coefficients for all dataset fits were also strong, with only the Gutter and Flange having R^2 values below 0.9, at values of 0.87 and 0.85, respectively.

Percent replication values were calculated for each as-extracted fatigue dataset, using Equation (2.1). The number of loading conditions was visually approximated based on stress data points within ± 10 MPa of one another. Variations in stress levels for the same loading condition were attributable to variations in fatigue specimen diameters from the machining process. Percent replication results are included Table 4.10, as well as the classification of each fatigue dataset based on the number of failure specimens and loading conditions, per ASTM E739 [31]. All as-extracted datasets had percent replications between 60% and 70%. Furthermore, all datasets were considered “Design Allowable”, with the exception of the Gutter dataset, which was classified as “Research and Development”. This latter classification signifies a somewhat decreased level of confidence in Gutter data based on the ASTM E739 standard [31]. The Gutter dataset falls within this classification due to a lower number of tested specimens. A lower number of specimens were tested for the Gutter due to a lack of availability at the time of testing. Nevertheless, the data acquired for the Gutter shows consistency and remains useful for the purposes of this study.

Table 4.10: Percent replication of each as-extracted fatigue dataset

	Rim Base	BS Band	Flange	Gutter	Lock Ring
Number of Specimens	13	15	17	11	12
Number of Loading Conditions	5	5	5	4	4
Percent Replication (%)	61.5	66.7	70.6	63.6	66.7
ASTM E739 Dataset Classification	Design Allowable	Design Allowable	Design Allowable	Research and Development	Design Allowable

In Figure 4.17, it can be seen that the Rim Base, BS Band, Flange, and Lock ring demonstrate qualitatively similar high-cycle fatigue behaviour. The Gutter shows the same trend in fatigue behaviour as other components, however, visually, failure points at all cycles are uniformly shifted to higher stresses for the Gutter. These visual observations are confirmed from stress values generated from each fit at failure cycles of 50,000 and 5,000,000, listed in Table 4.9. At 50,000 cycles to failure, as-extracted fits of the Rim Base, BS Band, Flange, and Lock Ring had similar failure stresses of 415.92 MPa, 415.30 MPa, 417.42 MPa, and 403.18 MPa, respectively. For the same cycles to failure, the as-extracted Gutter fit had a failure stress of 449.17 MPa. The same trend is present for the 5,000,000 cycles to failure criterion, with the as-extracted Gutter fit having a failure stress of 352.61 MPa, while other as-extracted fits ranged in failure stress from 292.75 MPa to 315.27 MPa. From these observations, two conclusions may be drawn: (1) the Rim Base, BS Band, Flange, and Lock Ring show similar fatigue behaviour in the as-extracted condition, and (2) initial analysis finds the Gutter material shows improved fatigue behaviour relative to other wheel components in the as-extracted condition.

All wheel components are fabricated from the Q345 alloy. With this in consideration and from microstructural, hardness, and tensile testing results, it was anticipated that the Rim Base, BS Band, and Flange would show similar fatigue behaviour. Thus, the similarities in fatigue behaviour between these components are consistent with previous observations. The Lock Ring showed superior microstructural properties with increased pearlite levels, as well as superior tensile properties, with increased YS and UTS values relative to other components. From these results, it may have been expected that the Lock Ring would show superior high-cycle fatigue behaviour. However, studies discussed in sections 2.2 [26] - [29] and 2.5.2 [53], [54] found the opposite to be true. In these studies, it was found that in a ferrite-pearlite microstructure, high-cycle fatigue behaviour will be controlled by the ferrite phase, which has a lower failure stress relative pearlite. This behaviour is attributable to crack initiation being the controlling fatigue mechanism in the high-cycle regime. Crack initiation in the high-cycle regime allows for sufficient time for crack nucleation to occur at ferrite grains, and subsequent crack propagation to occur along and through ferrite grains. Conclusions from the studies found that to improve the high-cycle fatigue behaviour of ferrite-pearlite steels, strengthening of the ferrite phase was critical, while increases in pearlite content would not provide significant benefits to high-cycle fatigue behaviour. Thus, since no ferrite strengthening agents were included in the Lock Ring alloy, the fatigue behaviour of the Q345 alloy in the Lock Ring is consistent with the fatigue behaviour of other ferrite-pearlite microstructures discussed in the literature.

The Rim Base, BS Band, Flange, and Lock Ring are fabricated from the same alloy, and show consistent fatigue behaviour. Therefore, for simplicity, these

components are collectively referred to as ‘Rim’, unless otherwise stated, for the remainder of this section.

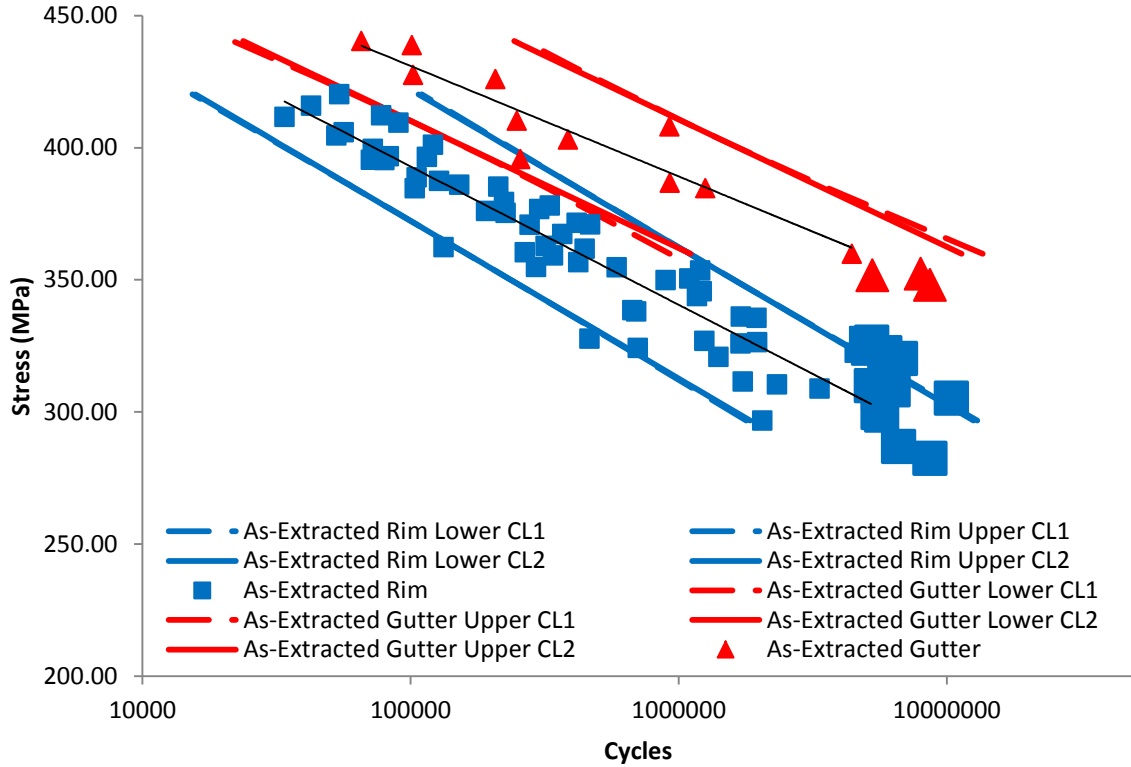


Figure 4.18: As-extracted fatigue data with upper and lower confidence bands

In Figure 4.18, S-N plots of similar as-extracted fatigue behaviour have been replaced by the ‘Rim’, which includes a single log-linear fit. An S-N plot of the as-extracted Gutter is also included, with the previously included fit. For these two datasets, upper and low confidence bands have been included. These bands were calculated using Equation (2.13) and Equation (3.3). In Figure 4.18, Confidence bands generated using Equation (2.13) are described as CL1 and confidence bands generated using Equation (3.3) are described as CL2. The purpose of the confidence bands are to visually illustrate the variance associated with each fatigue fit, and to provide a more conservative estimate of the fatigue behaviour of the material. Confidence bands generated using Equation

(3.3) are of the same form as Equation (4.2) and can therefore be readily used in fatigue design problems.

Several observations can be made from Figure 4.18. First, both types of confidence bands yield identical limits for the as-extracted ‘Rim’, and very similar limits for the as-extracted Gutter. This occurs because the datasets are fairly large, and do not exhibit a large degree of variation. Therefore, for the remainder of the section, only CL2 confidence bands will be discussed. Confidence bands for the as-extracted Gutter have slight overlap with those of the ‘Rim’; however, overall, the as-extracted Gutter dataset remains statistically unique relative to the ‘Rim’. Fatigue run-out data points, indicated by their larger size, encompass the CL2 range of the ‘Rim’, and appear to follow the general trend of the ‘Rim’ fit. Therefore, the endurance limit of the Q345 material from the ‘Rim’ in the as-extracted condition likely falls within the range of run-out data points, between 282 MPa and 327 MPa. Similarly, the as-extracted Gutter endurance limit likely occurs near 352 MPa. Approximate fatigue endurance stresses are summarized in Table 4.11. Fatigue equations for the lower CL2 confidence bands of the ‘Rim’ and Gutter are also included in Table 4.11. These equations yield conservative estimates of the fatigue behaviour, and are further discussed in section 4.6.2.

Table 4.11: Endurance strengths and lower limit fatigue equations for as-extracted ‘Rim’ and Gutter datasets

	As-Extracted ‘Rim’	As-Extracted ‘Gutter’
Approximate Endurance Strength from Experimental Testing (MPa)	~282-327 MPa	~352 MPa
CL2 Lower Limit Fatigue Equation (S in units of MPa)	$\log_{10} N = -0.01675 \times S + 11.2369$	$\log_{10} N = -0.02071 \times S + 13.4965$

The Gutter showed similar corrosion, microstructural, and tensile behaviour as other wheel components. Furthermore, the Gutter had consistent compositional values, with only slightly elevated levels of Silicon relative to other wheel components. Therefore, based on experimental observations throughout Chapter 4, it is difficult to explain with certainty why the as-extracted Gutter specimens showed statistically improved fatigue performance relative to other wheel components. The most likely explanation may be linked to specimen surface finish, which plays a large role in high-cycle fatigue behaviour. While surface roughness was periodically measured to ensure consistency between all specimens, it was not vigorously tracked. It is possible that Gutter specimens had a superior surface finish after completion of polishing relative to other specimens. Furthermore, during machining of Gutter specimens, the machinist indicated machining of Gutter specimens proved more difficult than other wheel components. This latter point may be indicative of some work hardening during the machining process of Gutter specimens that may have artificially improved fatigue life. No matter the cause, the increase in endurance limit of the as-extracted Gutter is only 16.7% relative to the mean 'Rim' endurance limit. Additionally, as-extracted fatigue data is meant only as a reference to pre-corroded data. In the mining environment, surface degradation of wheel components often occurs quickly, and so no wheel component should follow as-extracted fatigue behaviour.

In the literature [55], mean fatigue lives of the 16Mn alloy were reported as 112,201 cycles, 194,498 cycles, and 707,945 cycles, for stress amplitudes of 394 MPa, 373 MPa, and 334 MPa, respectively. From the as-extracted 'Rim' data, corresponding fatigue lives at those stress values are 95,345 cycles, 240,083 cycles, and

1,334,119 cycles, respectively. Percent differences in experimental cycles relative to the literature are -15.0%, 23.4%, and 88.4%, respectively. Differences become high for higher failure cycles because a higher degree variance occurs due to differences in surface finish and because failure cycles increase logarithmically with lower stress amplitudes. A better comparison may be made if the logarithm of failure cycles is used in place of the actual cycles. Under this approach, percent differences are -1.4%, 1.7% and 4.7%, for stresses of 394 MPa, 373 MPa, and 334 MPa, respectively. These differences show that the high-cycle fatigue behaviour of the Q345 alloy extracted from the Rim Base, BS Band, Flange, and Lock ring is consistent with the data given in literature.

4.6.2. Pre-Corroded Fatigue Behaviour

Pre-corroded fatigue results from Lock Ring and Gutter specimens are included as S-N curves in Figure 4.19. Base 10 log-linear fits using Equation (4.2) are included for both datasets. Additionally, upper and lower confidence limits, generated using Equation (3.3) are also included. Results from statistical analysis of each dataset, consistent with the procedures of sections 2.3 and 4.6.1, are included in Table 4.12. Results include reliability and dataset classification, per ASTM E739 [31]. Equations describing each dataset are also included.

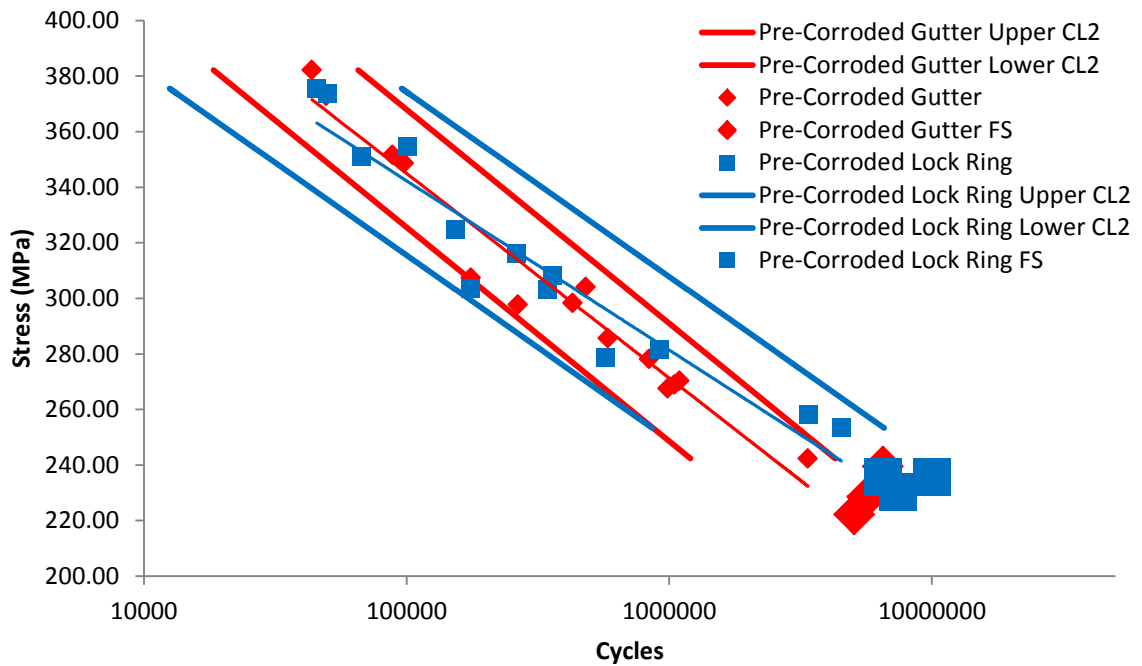


Figure 4.19: S-N fatigue behaviour of pre-corroded Lock Ring and Gutter datasets

Table 4.12: Results of statistical analysis of pre-corroded Gutter and Lock Ring fatigue datasets

	Pre-Corroded Gutter	Pre-Corroded Lock Ring
Equation of Dataset Fit (S in units of MPa)	$\log_{10} N = -0.0130 \times S + 9.5041$	$\log_{10} N = -0.0150 \times S + 10.1838$
Reliability	71.43%	61.54%
Classification	Design Allowable	Design Allowable
F-Crit	4.75	4.84
F-Test	267.71	119.62
T-Crit	2.18	2.20
T-Slope	16.36	10.94
T-Intercept	38.85	23.42
Correlation Coefficient	0.96	0.92

F-Test, T-Slope, and T-Intercept values of each fit were found to significantly exceed respective F-crit and T-crit values for both pre-corroded fatigue datasets. Thus, log-linear fits of each dataset are considered statistically relevant. Reliability of the

datasets, calculated under direction of ASTM E739, were 71.4% for the Gutter dataset, and 61.5% for the Lock Ring dataset. Both datasets were classified as “Design Allowable”, per ASTM E739.

The pre-corroded fatigue behaviour of Lock Ring and Gutter specimens appear qualitatively similar, as shown in Figure 4.19. Almost all fatigue data points between the two tested components are consistent with one another. Furthermore, both confidence bands show similar behaviour; however, pre-corroded confidence bands of the Gutter are narrower than those of the Lock Ring. This difference should be attributable to the lower variability in the Gutter dataset, which had a correlation coefficient of 0.96 for its fit, while the Lock Ring dataset only had correlation coefficient of 0.92 for its fit. Approximate endurance strengths for both datasets are also consistent, as depicted by the larger data points in Figure 4.19, which range in stress values from 222 MPa to 236 MPa.

To quantitatively evaluate the similarity of the two pre-corroded datasets, failure stresses at 50,000 cycles and 5,000,000 cycles were calculated for each dataset using dataset fits. Results are summarized in Table 4.13. Percent differences were calculated using Equation (4.1); however, the denominator was taken as the average of the two measurements. At 50,000 cycles, the Gutter and Lock Ring fits yielded failure stresses of 369.62 MPa and 356.66 MPa, respectively. The percent difference between these two measurements was 1.08%, showing that there is little deviation between the two sets. Similar results were found at 5,000,000 cycles, where the percent difference between the failure stresses of the two fits was only 7.38%.

Table 4.13: Failure stresses of pre-corroded dataset fits at 50,000 and 5,000,000 cycles

	Pre-Corroded Gutter Fatigue Fit	Pre-Corroded Lock Ring Fatigue Fit	Percent Difference (%)
Stress at 50,000 cycles (MPa)	369.62	365.66	1.08
Stress at 5,000,000 Cycles (MPa)	215.78	232.32	7.38

From qualitative and quantitative observations of the similarities between the two pre-corroded fatigue datasets, it can be concluded that they show consistent behaviour and are representative of a larger dataset. Together, the two datasets provide a good representation of the Q345 alloy in the pre-corroded condition of this study. This conclusion reinforces the suggestion that the improved fatigue performance of the as-extracted Gutter specimens was the result of improved surface conditions, which could not exist for pre-corroded specimens. The two datasets are from the same alloy and show similar fatigue behaviour. Thus, for the remainder of this section, they will be combined and referred to simply as ‘Rim’, following the same convention as in section 4.6.1.

The as-extracted ‘Rim’ fatigue behaviour of section 4.6.1 and the previously discussed pre-corroded ‘Rim’ fatigue behaviour are plotted as S-N curves in Figure 4.20. Confidence bands generated using Equation (3.3) for both datasets are denoted by ‘CL2’. Approximate endurance strengths for both datasets are included as the larger data points, denoted by ‘FS’. These points represent specimens that did not fail after five million cycles. Since both ‘Rim’ datasets consist of subsets of fatigue data from other wheel components, the datasets have a large amount of fatigue data points. This improves the rating of each dataset under ASTM E739 guidelines. Replication ratings for as-extracted and pre-corroded ‘Rim’ datasets are 91.2% and 81.5%, respectively. With these

replications and the large number of data points in each dataset, both datasets fall under the classification of “Reliability”, highlighting the reliability of the data.

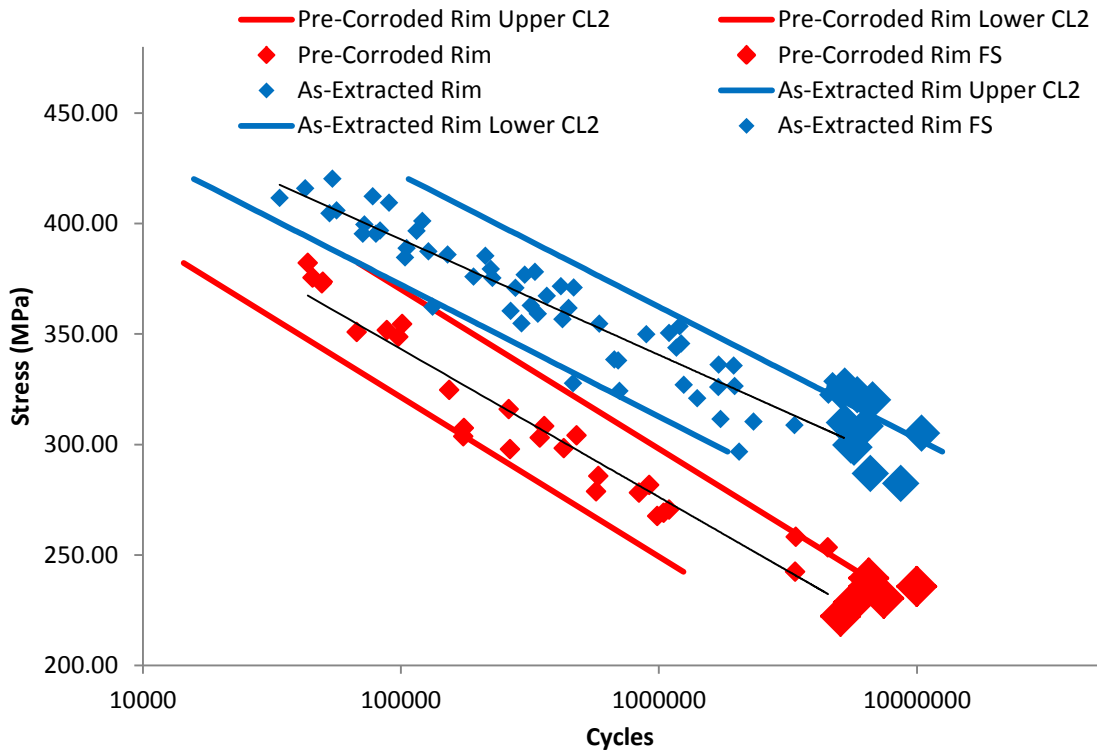


Figure 4.20: S-N curves of as-extracted and pre-corroded 'Rim' fatigue datasets

In Figure 4.20, it can be qualitatively seen that there is a significant decrease in fatigue behaviour between as-extracted and pre-corroded datasets. Log-linear equations representing both datasets are included in Table 4.14. These two equations were used to calculate failure stresses of each dataset at 50,000 cycles and 5,000,000 cycles, respectively, to quantitatively evaluate the fatigue performance decrease of the pre-corroded fatigue specimens.

At 50,000 cycles, the as-extracted ‘Rim’ fit yields a failure stress of 413.97 MPa and the pre-corroded ‘Rim’ fit yields a failure stress of 366.36 MPa. The percent difference between the two failure stresses is 11.50%. This difference, while large, is not

as large as that at failure cycles near 5,000,000. Near the lower cycle regime (50,000 cycles), fatigue crack initiation is the dominant mechanism, but crack propagation still plays a large role in fatigue failure. Therefore, while surface effects are important, they are not as significant as in the high cycle (5,000,000 cycles) regime. For this reason, percent differences at lower cycles between as-extracted and pre-corroded datasets are lower. Additionally, for the same reason, variance in fatigue points at low failure cycles is also lower.

At 5,000,000 cycles, the as-extracted ‘Rim’ fit yields a failure stress of 294.89 MPa and the pre-corroded ‘Rim’ fit yields a failure stress of 222.48 MPa. The percent difference between these two stresses is 24.56%. The decrease in fatigue performance of the pre-corroded specimens at 5,000,000 cycles is over 100% greater than that at 50,000 cycles. This larger percentage decrease is in-line with high-cycle fatigue behaviour, which is controlled by the crack initiation phase, and therefore controlled by surface effects.

Table 4.14: Failure stresses of as-extracted and pre-corroded ‘Rim’ fits at 50,000 and 5,000,000 cycles

	As-Extracted 'Rim' Fit	Pre-Corroded 'Rim' Fit	Percent Difference (%)
Equation of Dataset Fit (S in units of MPa)	$\log_{10} N = -0.0168 \times S + 11.6531$	$\log_{10} N = -0.0139 \times S + 9.7914$	
Stress at 50,000 Cycles (MPa)	413.97	366.36	-11.50
Stress at 5,000,000 Cycles (MPa)	294.89	222.48	-24.56

The infinite life criterion of all tested specimens was set as 5,000,000 cycles. All specimens that did not fail after 5,000,000 cycles are considered “run-out”, and are representative of the approximate endurance strength of each dataset. Approximate endurance strengths of the as-extracted ‘Rim’ specimens range from 282 MPa to 327 MPa, while pre-corroded endurance strengths of ‘Rim’ specimens range from 222 MPa to 236 MPa. Failure stresses calculated using both ‘Rim’ dataset fits were 292.89 MPa and 222.48 MPa, for the as-extracted and pre-corroded datasets, respectively. These two failure stresses fall within the range of endurance strengths from experimental testing of each material condition. This shows that both fits provide a good estimate of endurance strength.

In fatigue design, conservative estimates of fatigue life are generally used, notably for designs intended to have an infinite fatigue life. In such instances, lower confidence bands of fatigue behaviour should be used in place of actual fatigue dataset fits for more conservative fatigue life estimates. Given that multi-piece mining wheels are intended to have an infinite fatigue life, lower confidence bands should be used in fatigue life estimates of the wheels. Lower confidence band equations of as-extracted and pre-corroded ‘Rim’ fatigue datasets are included in Table 4.15. These estimates are meant to be used within the research group to facilitate fatigue analyses of multi-piece wheel assemblies. Failure stresses at 5,000,000 cycles are also included in Table 4.15, and represent conservative endurance strength estimates.

Using the CL2 equations of each dataset, the as-extracted ‘Rim’ dataset has a fatigue failure stress of 270.12 MPa at 5,000,000 cycles, and the pre-corroded ‘Rim’ dataset has a fatigue failure stress of 198.15 MPa at 5,000,000 cycles. The percent

decrease in failure stress of the pre-corroded dataset relative to the as-extracted dataset when using the CL2 equations is 26.7%. This decrease is consistent with the decrease in fatigue stress when using the actual ‘Rim’ dataset fits, summarized in Table 4.14. When designing for infinite fatigue life using the Q345 alloy, the stress of 198.15 MPa should be taken as the endurance limit when some degree of corrosion is expected; however, if the level of corrosion is severe, a further reduction in endurance strength should be anticipated.

Table 4.15: Lower confidence band equations of as-extracted and pre-corroded ‘Rim’ datasets

	As-Extracted ‘Rim’	Pre-Corroded ‘Rim’
Lower Confidence Band (CL2) Equation of Fatigue Dataset	$\log_{10} N = -0.0168 \times S + 11.2369$	$\log_{10} N = -0.0139 \times S + 9.4533$
Failure Stress at 5,000,000 Cycles Using CL2 Equation (MPa)	270.12	198.15

The fatigue strength of the as-extracted ‘Rim’ calculated using the CL2 equation at 5,000,000 cycles is 270.12 MPa. Using this stress level with the pre-corroded ‘Rim’ CL2 equation, the pre-corroded ‘Rim’ material would fail at approximately 499,611 cycles. This represents a decrease in fatigue life of approximately 900%. This observation is critical in demonstrating that corrosion must be accounted for in the fatigue life assessment of multi-piece wheel designs, otherwise, wheel life expectancies will be dramatically decreased.

4.6.3. Fracture Surface Analysis

Fracture surfaces of fatigue specimens were examined using a scanning electron microscope. The purpose was to observe variations in fracture surfaces cause by

different parameters. Parameters examined included low and high loading conditions for as-extracted specimens and pre-corroded specimens. All examined fracture surfaces originated from Gutter specimens; however, similar traits were also noted to be present on specimens from other wheel components during initial SEM observations.

SEM fracture surfaces of low-load as-extracted and pre-corroded fatigue specimens are shown in Figure 4.21. For both low-load fractographs, it can be seen that the majority of the fracture surface is flat, with many fatigue striations or ripples. This portion of the fracture surface is linked to the crack initiation and micro-crack propagation phases, which dictate the majority of low-load, high-cycle fatigue behaviour. Crack initiation sites are indicated by red circles on each SEM image. The elevated areas of each image represent the macro-crack propagation and fatigue failure phases. For low-load, high-cycle fatigue, these mechanisms occur over a relatively small duration and have an overall minimal effect on the fatigue life of the material in the high-cycle regime. Observations of low-load fracture surfaces are consistent with the fatigue analyses previously conducted, which stated crack initiation as the dominant mechanism in the fatigue behaviour of high-cycle fatigue specimens.

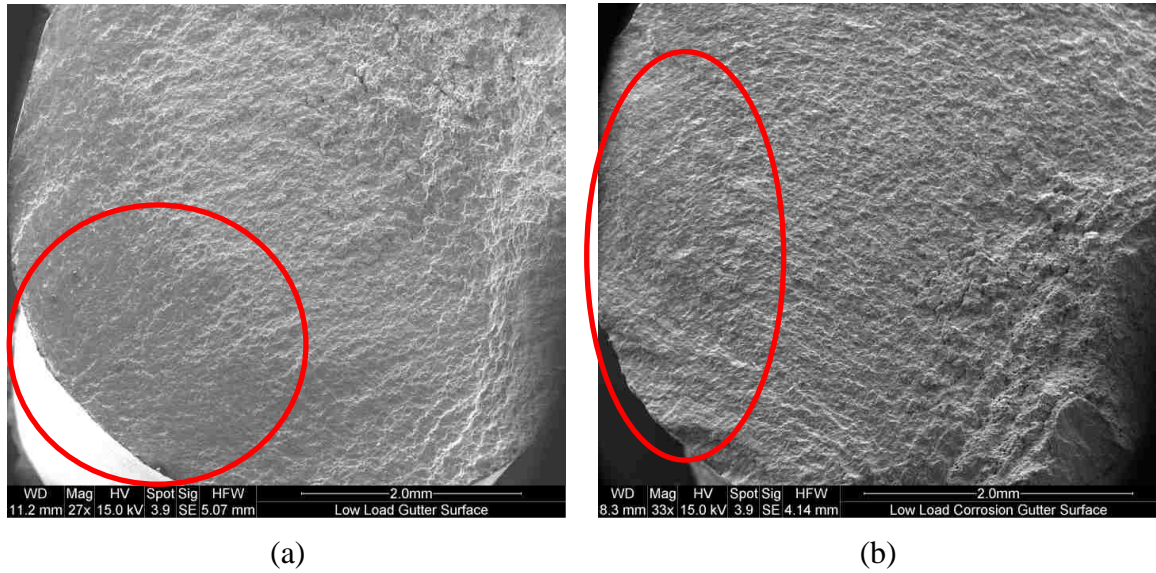
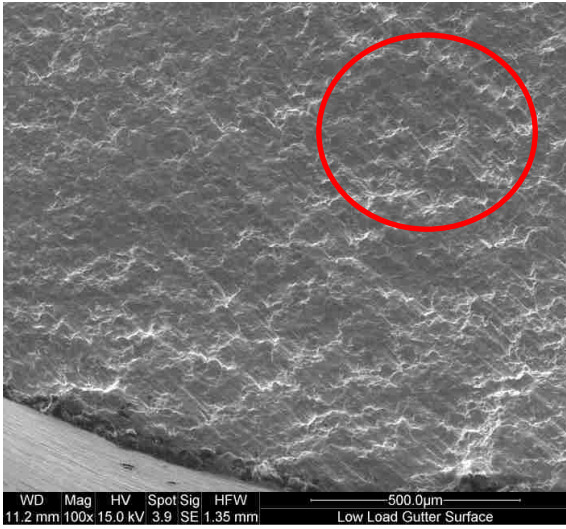
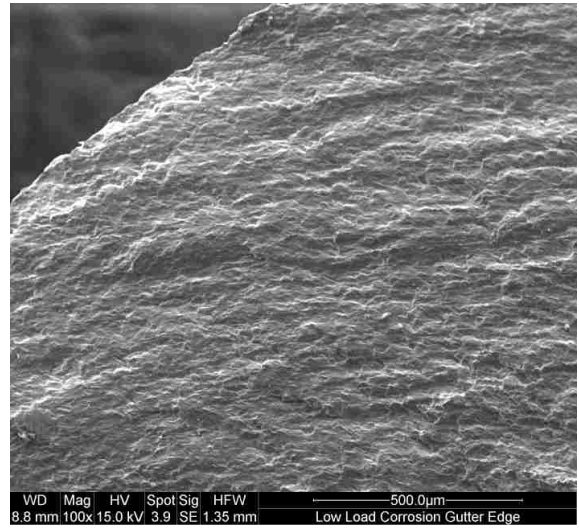


Figure 4.21: Fracture surfaces of low-load Gutter fatigue specimens (a) as-extracted and (b) pre-corroded

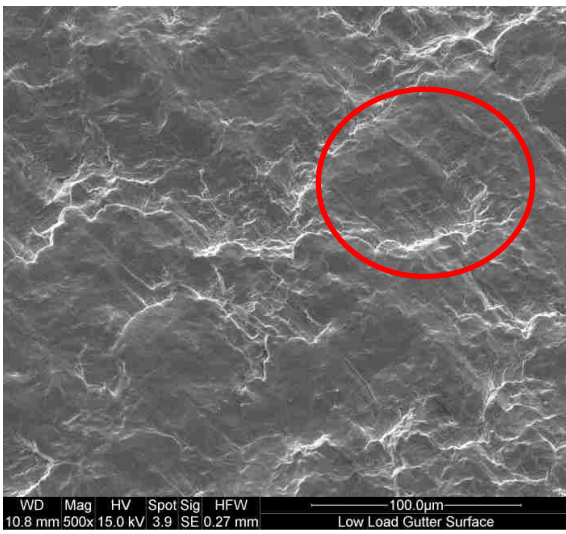
Higher magnification fractographs of crack initiation and failure regions of low-load as-extracted and pre-corroded Gutter fatigue specimens are included in Figure 4.22. For the fractographs of the initiation zones, both fatigue surfaces show similar features, with striations and ripples, indicative of the opening and closing of micro-cracks during cyclic loading. Striations are indicated by red circles on each SEM image. Fractographs of failure zones also have similar features between the low-load failure regions of the as-extracted and pre-corroded specimens. In both fractographs, signs of plastic deformation and ductile fracture are present in the form of void coalescences, which have a cup-cone structure. Cup-cone structures are indicated by red circles on each SEM image. Additionally, some flat facets, which may depict quasi-cleavage fracture, are present. These facets are indicative of brittle failure. The majority of the fracture regions for both specimens contain the ductile cup-cone features. Therefore, final fracture of both low-load specimens was primarily ductile in nature.



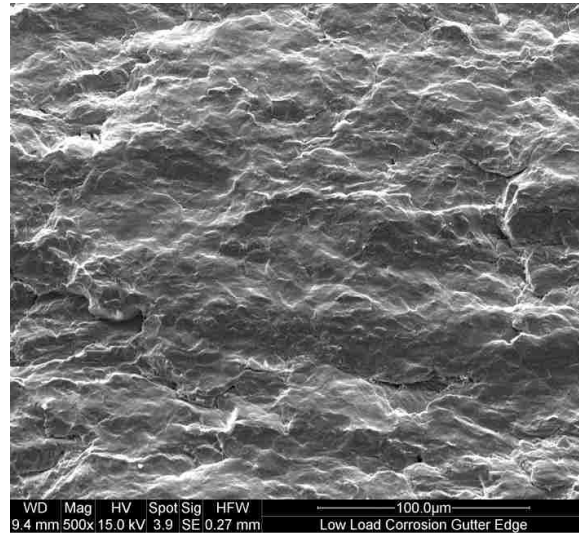
(a)



(b)



(c)



(d)

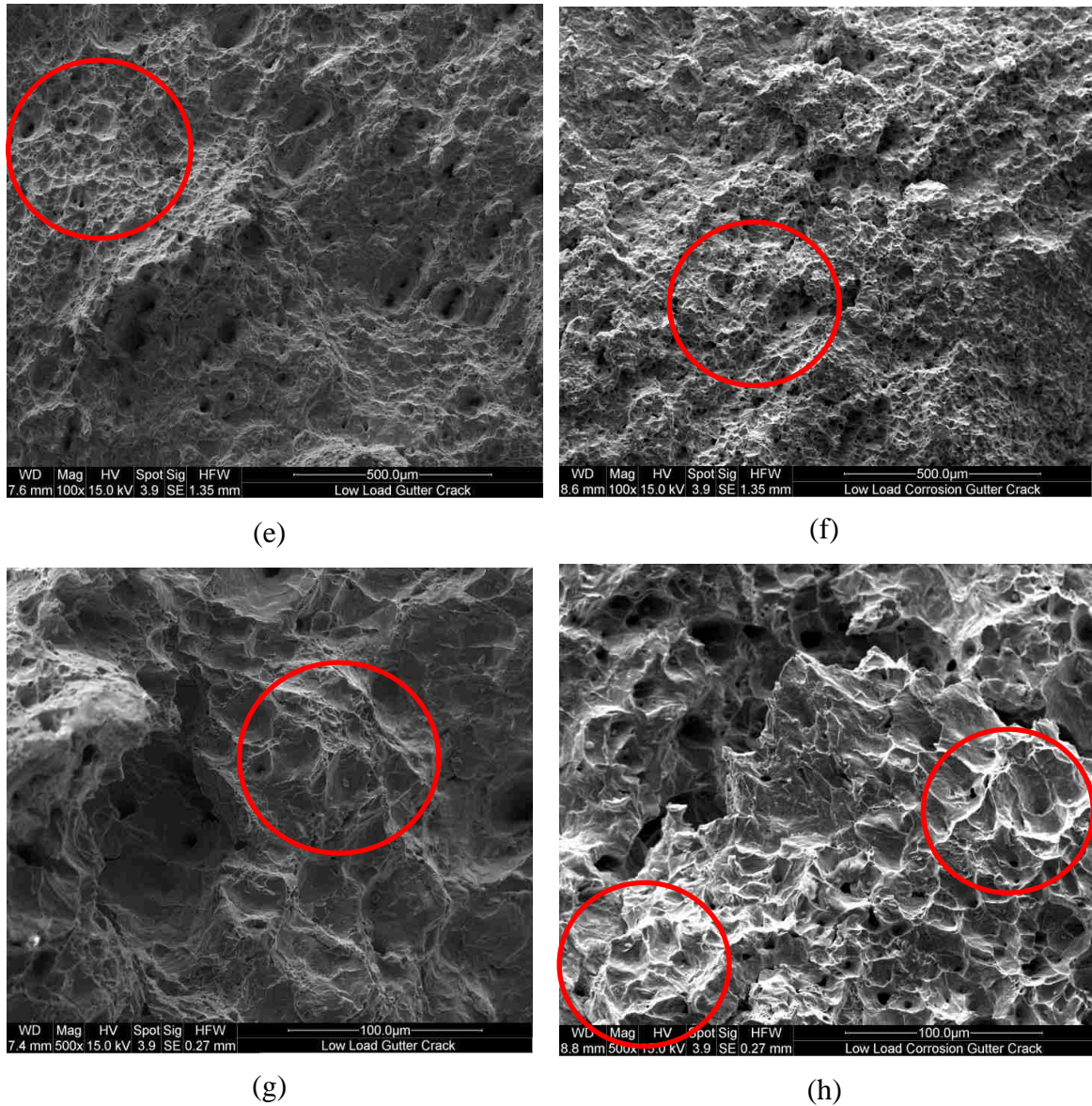


Figure 4.22: Higher magnification SEM fractographs of low-load Gutter fatigue specimens in the (left) as-extracted and (right) pre-corroded conditions. From top to bottom: (a,b) 100x, (c,d) 500x fatigue initiation zone; (e,f) 100x, (g,h) 500x fatigue failure zone.

High-load, low-cycle SEM surface fractographs of as-extracted and pre-corroded Gutter fatigue specimens are included in Figure 4.23. In these fractographs, it can be seen that the crack initiation phase occupies a smaller portion of the total surface area relative to the low-load, high-cycle surface fractographs. The fatigue failure region occupies a larger part of each fractograph. These observations are consistent with the

discussed low-cycle fatigue behaviour of the specimens, which is controlled by both the crack initiation and crack propagation phases.

While both fractographs share similarities in the area distribution of the crack initiation and crack propagation phases, it is important to note the difference between the locations of these phases. For the as-extracted specimen, crack initiation uniformly occurs at the top half of the specimen, and crack propagation/failure occurs at the bottom half. This is indicated by the red circle in Figure 4.23a, which shows the flatter surface region, associated with crack initiation. Conversely, for the pre-corroded specimen, crack initiation occurs at multiple locations along the specimen edge, while crack propagation/failure is somewhat in the middle of the specimen. The difference between these two specimens should be attributable to surface finish and the nominal applied stress. For the as-extracted specimen, the surface was relatively uniform and smooth, and so there were not many areas for crack initiation to occur, while for the pre-corroded specimen, there were many possible initiation points, resulting in crack propagation from many different locations. The high-load conditions further increased the probability for multiple crack initiation locations to occur, which is why the same fatigue phase locations were not observed as frequently in the case of the low-load pre-corroded fatigue specimens.

Higher magnification fractographs of crack initiation and propagation phases for high-load fatigue specimens were consistent with their low-load counterparts, and have been omitted to avoid repetition. It should, however, be noted that a small area of the as-extracted high-load fatigue failure region showed signs of brittle failure. This is likely the result of the increased loading conditions, and the reduction of the duration of the

fatigue initiation phase. Nevertheless, the majority of the as-extracted samples demonstrated a high level of plastic deformation, consistent with the behaviour of the low-load as-extracted fatigue specimen.

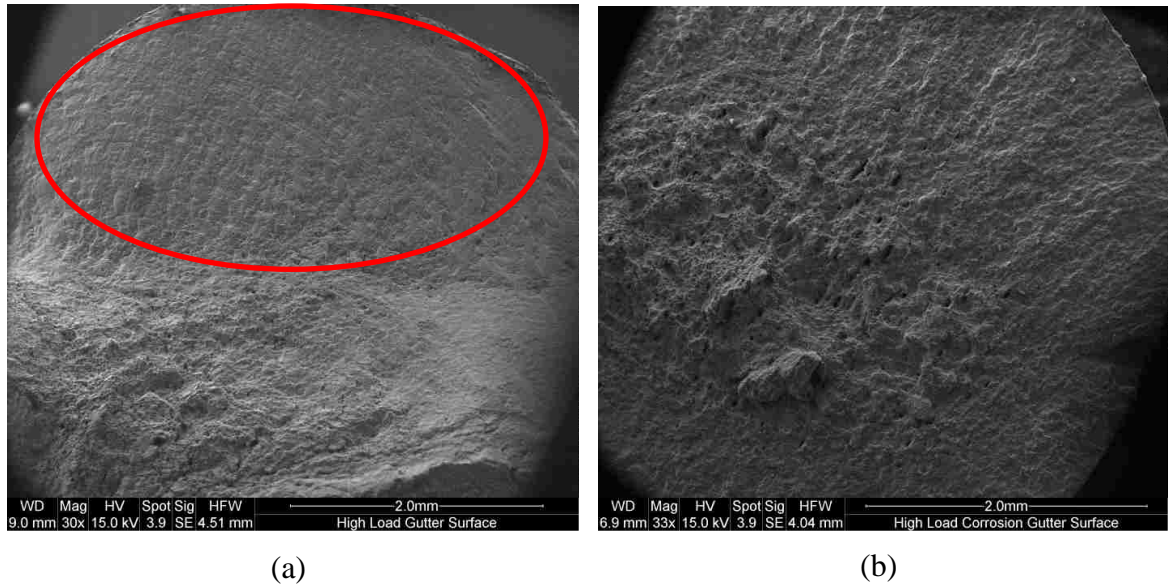


Figure 4.23: Fracture surfaces of high-load Gutter fatigue specimens (a) as-extracted and (b) pre-corroded

4.7. Summary of Results

Key results discussed throughout Chapter 4 are summarized in Table 4.16, below.

Table 4.16: Summary of key results from experimental testing discussed throughout Chapter 4

Property	Rim Base	BS Band	Flange	Gutter	Lock Ring
Average Mn Content (wt%)	1.23				
Average Si Content (wt%)	0.49				
Surface Area Mass-Loss Rate ($\text{mg}\cdot\text{cm}^{-2}\cdot\text{day}^{-1}$)	N/A	0.674		0.9645	
30 Day Surface Area Mass-Loss ($\text{mg}\cdot\text{cm}^{-2}$)	N/A	17.89		26.3	

Property	Rim Base	BS Band	Flange	Gutter	Lock Ring
R _a As-Extracted Surface Roughness (µm)	<0.4				
R _a Pre-Corroded Surface Roughness (µm)	N/A	14.73			
Microstructure Observations	All microstructures consist of a base ferrite matrix, with colony pearlite.				
Area Percent Pearlite (%)	8.53	9.26	10.24	14.92	41.06
Cross-Sectional Hardness (HRB)	92.84	84.05	92.85	Core: 84.11, Surface: 93.47	97.15
As-Extracted Average Yield Strength (MPa)	373.2-482.4				681.5
As-Extracted Average Ultimate Tensile Strength (MPa)	470.7-544.1				779.8
Fatigue Observations	Fatigue specimens from all components show consistent behaviour for each surface condition. The only exception is the as-extracted Gutter dataset, which showed slightly improved fatigue behaviour due to a suspected superior surface finish.				
As-Extracted Fatigue Stress at 50,000 Cycles (MPa)	413.97			449.17	413.97
As-Extracted Fatigue Stress at 5,000,000 Cycles (MPa)	294.89			352.61	294.89
Pre-Corroded Fatigue Stress at 50,000 Cycles (MPa)	N/A			336.36	
Pre-Corroded Fatigue Stress at 5,000,000 Cycles (MPa)	N/A			222.48	
'Rim' As-Extracted Fatigue Fit Equation	$\log_{10} N = -0.0168 \times S + 11.6531$				N/A

Property	Rim Base	BS Band	Flange	Gutter	Lock Ring
Lower CL2 Equation of 'Rim' As-Extracted Dataset	$\log_{10} N = -0.0168 \times S + 11.2369$				N/A
'Rim' Pre-Corroded Fatigue Fit Equation	N/A			$\log_{10} N = -0.0139 \times S + 9.7914$	
Lower CL2 Equation of 'Rim' Pre-Corroded Dataset	N/A			$\log_{10} N = -0.0139 \times S + 9.4533$	
Fatigue Surface Failure Features	Flat regions with striations and ripples, representative of crack initiation and elevated regions with ductile and brittle features, representative of crack propagation/fatigue failure. Brittle fracture features more prominent at high loads and in pre-corroded specimens.				

5. CONCLUSIONS AND RECOMMENDATIONS

The mechanical and material behaviour of the Q345 alloy used in the fabrication of five-piece mining wheel assemblies was investigated. Material samples were taken from all wheel components. Variances in composition between components were measured. Representative samples were corroded, and mass-loss and surface roughness measurements were taken. Microstructures of all wheel components were observed. Hardness measurements were recorded. Tensile properties of the alloy from all wheel components were evaluated in the as-extracted and pre-corroded conditions. The high-cycle fatigue behaviour of the alloy in the as-extracted and pre-corroded conditions was determined for specimens extracted from most wheel components. Tensile and fatigue results have been used within the research group to facilitate numerical prediction of multi-piece wheel failures. Key results from experimental testing are summarized below.

1. Manganese and silicon levels of samples from most wheel components were within the nominal permissible range of the Q345 alloy. Variance in Mn and Si levels were not high, with most wheel components showing consistent levels of the two alloying elements. The Gutter showed higher levels of Mn and Si than other components; however, these levels were still within the permissible range of the alloy, when considering error in EDS measurements.
2. Mass-loss corrosion of tensile and fatigue specimens from all tested components (BS Band, Flange, Gutter, and Lock Ring) was approximately linear over the duration of accelerated corrosion testing. BS Band, Flange, and Gutter specimens had similar

corrosion rates, while the Lock Ring had an increased rate of corrosion. Surface area mass-loss corrosion rates of Gutter and Lock Ring samples were $0.674 \text{ mg}\cdot\text{cm}^{-2}\cdot\text{day}^{-1}$ and $0.964 \text{ mg}\cdot\text{cm}^{-2}\cdot\text{day}^{-1}$, respectively. The increased rate of corrosion in Lock Ring specimens was attributed to higher pearlite content in the microstructure, which is more susceptible to corrosion than ferrite. The fully submerged corrosion rates from experimental testing were comparable to cyclic wet/dry corrosion rates reported in the literature. The R_a surface roughness of a sample corroded specimen was $14.73 \mu\text{m}$, while that of a worn wheel sample was $16.59 \mu\text{m}$. Overall, the level of corrosion to tensile and fatigue specimens was determined to be comparable to that of the mining environment, with corrosion rates being on the same order of magnitude as some observations reported in the literature.

3. Microstructures of samples from all wheel components were found to consist of a base ferrite matrix with colony pearlite dispersed throughout the microstructure. Area pearlite levels were near or below 10% for the Rim Base, BS Band, and Flange. Area pearlite of the gutter was observed to be approximately 14.9%. The Lock Ring sample had an average area pearlite content of 41.1%. The increased levels of pearlite in the Lock Ring should result from the higher cooling rates in the Lock Ring during production, due to its small thermal mass relative to other wheel components.
4. Cross-sectional hardness measurements found no significant variations in the Rim Base, BS Band, Flange and Lock Ring. Only the Gutter showed variations in cross-sectional hardness, with surface hardness values approaching those of the Lock Ring, and core hardness values near those of the BS Band. Overall, average cross-sectional Rockwell B hardness measurements were 92.8, 84.0, 92.8, 84.1, 93.5, and 97.2, for

- the Rim Base, BS Band, Flange, Gutter Core, Gutter Surface, and Lock Ring. The higher hardness readings of the Lock Ring were consistent with the elevated pearlite content in the Lock Ring microstructure. The difference in Gutter hardness values should be attributed to the forming process of the Gutter, which acts to harden the surface.
5. Tensile results of as-extracted specimens found that all wheel components meet the minimum yield strength and ultimate tensile strength requirements of ASTM A572 G50. The average yield strength of as-extracted specimens from the Rim Base, BS Band, Flange, and Gutter ranged from approximately 373 MPa to 482 MPa, while ultimate tensile strengths ranged from approximately 470 MPa to 544 MPa. As-extracted Lock Ring specimens had an average yield strength of 682 MPa, and an average ultimate tensile strength of 780 MPa. The increased performance of Lock Ring specimens correlated with microstructural observations, which found the Lock Ring to have a high pearlite content relative to other wheel components. Tensile results of pre-corroded specimens did not show large differences from the as-extracted results. Ultimate tensile strengths of pre-corroded specimens were no more than 10% lower than as-extracted specimens.
 6. The high-cycle fatigue behaviour of as-extracted wheel component specimens was largely consistent between all wheel components. As-extracted Lock Ring specimens did not show increased fatigue performance, despite improved tensile and microstructural properties. This observation was in line with the literature, which showed that pearlite content does not improve fatigue life, when a base ferrite matrix is present. Given the consistency between wheel component as-extracted fatigue

- datasets, they were analyzed as one cohesive dataset, representative of the high-cycle fatigue behaviour of the Q345 alloy in the as-extracted condition. The resulting dataset had a “Reliability” rating, per ASTM E739, with a percent replication of 91.2%. The log-linear regression analysis of the dataset yielded the following equation: $\log_{10} N = -0.0168 \times S + 11.6531$ (S in MPa). Endurance strengths at 5,000,000 cycles from experimental testing ranged from 282 MPa to 327 MPa, while the dataset fit yielded a stress of 295 MPa.
7. The high-cycle fatigue behaviour of pre-corroded wheel component specimens was consistent between the two tested wheel components (Lock Ring and Gutter). Thus, the two datasets were analyzed as one dataset, representative of the Q345 alloy in the pre-corroded condition. The ASTM E739 classification of the resulting dataset was “Reliability”, with a percent replication of 81.5%. A log-linear regression analysis of the dataset yielded the following equation: $\log_{10} N = -0.0139 \times S + 9.7914$ (S in MPa). The endurance strength of pre-corroded specimens from experimental testing ranged from 222 MPa to 236 MPa at 5,000,000 cycles, while the dataset fit yielded a stress of 222 MPa at 5,000,000 cycles. At 5,000,000 cycles, the endurance strength of the Q345 alloy in the pre-corroded condition decreased by 24.6% relative to the as-extracted condition.
 8. Lower confidence bands were generated for as-extracted and pre-corroded fatigue datasets of the Q345 alloy. Using these confidence bands, endurance strengths at 5,000,000 cycles were calculated for surface conditions. These strengths provide a more conservative estimate of the fatigue strength of the alloy. The stresses calculated using the lower confidence bands were 270 MPa and 198 MPa, for the as-

extracted and pre-corroded surface conditions, respectively. The percent difference between these two strengths was 26.7%.

9. Fracture surfaces of a select number of fatigue specimens were investigated. For high-cycle (>2,000,000 cycles) fatigue specimens, the fracture surface was predominantly associated with the fatigue crack initiation phase. The fracture surface of low-cycle (~50,000 cycles) fatigue specimens showed a more even distribution of the fatigue crack initiation and fatigue failure phases. Crack initiation regions showed striations, consistent with fatigue failure. Final failure regions showed primarily ductile failure features, such as void coalescences, and some brittle failure features, such as flat facets. Crack initiation of as-extracted specimens typically initiated in a single region, while crack initiation of pre-corroded specimens occurred at multiple sites. The difference in initiation behaviour was the result of the poor surface condition of pre-corroded specimens, which promoted multiple crack initiation locations.

The summary of corrosive mining environments and their relation to the experimental corrosion testing in this study provides a strong foundation for future corrosion studies of structural mining components. Such a thorough summary of corrosive mining conditions is not available in the literature to the knowledge of the author. The unique work conducted in this study provides insight into how the pre-corrosion of the Q345 alloy affects the high-cycle fatigue behaviour of the alloy, which is not available in the literature. This information is critical in the fatigue life assessment of multi-piece mining wheels fabricated from the Q345 alloy.

Observations from this study show that pre-corrosion greatly reduces the fatigue strength of the Q345 alloy; however, pre-corrosion may not be representative of actual corrosion conditions in a mining environment. Therefore, future work should be conducted to examine the synergistic effects of corrosion and fatigue on the high-cycle fatigue behaviour of mining wheel components. Until more thorough studies on the synergistic effects of corrosion and fatigue of the Q345 alloy are completed, the endurance strengths from the lower confidence bands generated in this study should be used to represent the behaviour of the Q345 alloy in the as-extracted and pre-corroded conditions. Using this fatigue data, the number of multi-piece wheel failures and resulting workplace injuries has the potential to be dramatically reduced.

REFERENCES

- [1] V. Vijaya, W. Altenhof and R. Banting, "A finite element approach to estimation of fatigue life for a three-piece mining vehicle wheel," *International Journal of Heavy Vehicle Systems*, vol. 17, no. 2, pp. 159-178, 2010.
- [2] L. Zhanbiao, A. Tonkovich, S. DiCecco, W. Altenhof, H. Hu and R. Banting, "Development and validation of a FE model of a mining vehicle tyre," *International Journal of Vehicle Design*, vol. 65, no. 2/3, pp. 176-201, 2014.
- [3] Department of Consumer and Employment Protection, "Safety and health alert; 13/97 Split ring wheel fatality," Government of Western Australia, 1997.
- [4] The National Institute for Occupational Safety and Health Fatality, "Mechanic Dies While Changing a Tire Mounted on a Multi-piece Split Rim Wheel - Massachusetts," Assessment and Control Evaluation (FACE) Program, Massachusetts Case Report: 07-MA-058, 2007.
- [5] Mines and Aggregates Safety & Health Association, "Multi-Piece Rims Leader Guide," Workplace Safety North, Ontario, Canada, 2000.
- [6] Occupational Health and Safety, "Hazard Alert; Truck Tire Explosions Claim Two More Lives," Saskatchewan Ministry of Labour Relations and Workplace Safety, Saskatchewan, Canada, 2004.
- [7] K. Heeres, "OTR Wheel Engineering," 25 July 2013. [Online]. Available: <http://blog.otrwheel.com/why-are-these-multi-piece-wheels-so-confusing/>. [Accessed 5 February 2014].
- [8] Occupational Health and Safety, "Hazard Alert; Tire Mount/Demount of Heavy Vehicles," Saskatchewan Ministry of Labour Relations and Workplace Safety, Saskatchewan, Canada, 1999.
- [9] The National Institute for Occupational Safety and Health, "Worker Struck By Multi-Piece Rim During Wheel Installation," Fatality Assessment and Control Evaluation (FACE) Program, Alaska Case Report: 03AK006, 2003.
- [10] The National Institute for Occupational Safety and Health, "Worker Killed While Inflating a Tire Mounted on a Multi-Piece Rim - Massachusetts," *FACE (Fatality Investigation and Control Evaluation) Facts*, vol. 7, no. 2, 2004.
- [11] Y. Zhang and C. Fleek, "Metallurgical Failure Analysis of Cracked Wheel Rim," Bodycote Materials Testing Canada Inc., Cambridge, Ontario, Canada, 2008.

- [12] Occupational Safety and Health, "Hazard Alert; Multi-Piece Rims; Lethal Hazards Part of Rim Repair Work," N.C. Department of Labor, Raleigh, North Carolina, USA, 2007.
- [13] S. Lampman, ASM Handbook Volume 19: Fatigue and Fracture, Materials Park, Ohio, USA: ASM International, 1996.
- [14] F. C. Campbell, "Chapter 14, Fatigue," in *Elements of Metallurgy and Engineering Alloys*, Materials Park, Ohio, USA, ASM International, 2008.
- [15] J. Schijve, "Chapter 2, Fatigue as a Phenomenon in the Material," in *Fatigue of Structures and Materials*, New York, New York, USA, Springer, 2008, pp. 13-58.
- [16] M. D. Sangid, "The physics of fatigue crack initiation," *International Journal of Fatigue*, vol. 57, pp. 58-72, 2013.
- [17] G. Totten, "Fatigue Crack Propagation," *Advanced Materials & Processes*, vol. 166, no. 5, pp. 39-41, 2008.
- [18] FEA-Opt Technology, "Stress-Life Fatigue Analysis," FEA-Opt Technology, [Online]. Available: http://www.fea-optimization.com/ETBX/stresslife_help.html. [Accessed 26 February 2014].
- [19] R. Budynas and K. Nisbett, "Fatigue Failure Resulting from Variable Loading," in *Shigley's Mechanical Engineering Design*, New York, New York, USA, McGraw-Hill Science/Engineering/Math, 2010, pp. 257-345.
- [20] EPI Inc., "Metal Fatigue," EPI Inc., [Online]. Available: http://www.epi-eng.com/mechanical_engineering_basics/fatigue_in_metals.htm. [Accessed 3 March 2014].
- [21] C. Lipson and R. C. Juvinall, Handbook of stress and strength: design and material applications, New York, New York, USA: Macmillan, 1963.
- [22] M. S. Corporation, "MSC Fatigue 2013 Theory Guide," MSC Software Corporation, Santa Ana, California, USA, 2008.
- [23] M. Papadopoulos, C. Apostolopoulos, N. Alexopoulos and S. Pantelakis, "Effect of salt spray corrosion exposure on the mechanical performance of different technical class reinforcing steel bars," *Materials and Design*, vol. 27, pp. 2318-2328, 2007.
- [24] L. Jianhua, H. Xuelong, L. Songmei and Y. Mei, "Effect of Pre-corrosion on Fatigue Life of High Strength Steel 38CrMoAl," *Journal of Wuhan University of Technology-Mater. Sci. Ed.*, vol. 26, no. 4, pp. 648-653, 2011.
- [25] K. van der Walde, J. Brockenbrough, B. Craig and B. Hillberry, "Multiple fatigue crack growth in pre-corroded 2024-T3 aluminum," *International Journal of Fatigue*, vol. 27, pp. 1509-1518, 2005.

- [26] M. Kurita, M. Yamamoto, K. Toyama, S. Nomura and K. Kunishige, "Effects of Strengthening Mechanisms on Fatigue Properties of Ferrite-Pearlite Hot-rolled Sheet Steel," *ISIJ International*, vol. 36, no. 4, pp. 481-486, 1996.
- [27] S. Sankaran, V. Subramanya Sarma and K. A. Padmanabhan, "Low cycle fatigue behavior of a multiphase microalloyed medium carbon steel: comparison between ferrite-pearlite and quenched and tempered microstructures," *Materials Science and Engineering*, vol. A345, pp. 328-335, 2003.
- [28] Y. Kim, J. Kwon, H. Lee, W. Jang, J. Choi and S. Kim, "Effect of Microstructure on Fatigue Crack Propagation and S-N Fatigue Behaviors of TMCP Steels with Yield Strengths of Approximately 450 MPa," *Metallurgical and Materials Transactions A*, vol. 42A, pp. 986-999, 2011.
- [29] G. MingFei and Y. Hao, "In-situ investigation on the fatigue crack propagation behavior in ferrite-pearlite and dual-phase ferrite-bainite low carbon steels," *Sci China Tech Sci*, vol. 56, no. 1, pp. 71-79, 2013.
- [30] P. C. Gope, "Scatter Analysis of Fatigue Life and Prediction of S-N Curve," *Journal of Failure Analysis and Prevention*, vol. 12, pp. 507-517, 2012.
- [31] ASTM Standard E739, 2010, "Standard Practice for Statistical Analysis of Linear or Linearized Stress-Life (S-N) and Strain-Life (e-N) Fatigue Data," ASTM International, West Conshohocken, Pennsylvania, USA, 2010.
- [32] H. J. Sutherland and P. S. Veers, "The Development of Confidence Limits For Fatigue Strength Data," in *2000 ASME Wind Energy Symposium*, Albuquerque, New Mexico, USA, 2000.
- [33] F. A. Morrison, "Obtaining Uncertainty Measures on Slope and Intercept of a Least Squares Fit with Excel," Michigan Technological University, Houghton, Michigan, USA, 2014.
- [34] S. Maddox, *Fatigue Strength of Welded Structures*, Swastan, Cambridge, England: Woodhead Publishing, 1991.
- [35] J. Guthrie, B. Battat and C. Grethlein, "Material Ease, Accelerated Corrosion Testing," *The AMPTIAC Quarterly*, vol. 6, no. 3, pp. 11-15, 2002.
- [36] S. Crammer and B. Covino Jr., *ASM Handbook Volume 13A Corrosion: Fundamentals, Testing, and Protection*, West Conshohocken, Pennsylvania, USA: ASTM International, 2003.
- [37] A. J. Mierzwa, "Sector 17 - Pulp and Paper, Appendix T, Mining," 2002.
- [38] A. Higginson and R. T. White, "A preliminary survey of the corrosivity of water in South African gold mines," *Journal of the South African Institute of Mining and Metallurgy*, vol. 83, no. 6, pp. 133-141, 1983.

- [39] J. Hadjigeorgiou, J. F. Dorion and E. Ghali, "Support System Performance Under Difference Corrosion Conditions," in *6th International Symposium on Ground Support in Mining and Civil Engineering Construction*, Cape Town, South Africa, 2008.
- [40] S. H. Ash, H. A. Dierks, E. W. Felegy and K. M. Huston, "Corrosive and Erosive Effects of Acid Mine Waters on Metals and Alloys for Mine Pumping Equipment and Drainage Facilities," United States Government Printing Office, Washington, District of Columbia, USA, 1955.
- [41] S. Nana, M. Cortie, R. Paton and D. Enright, "Environmentally assisted cracking of martensitic stainless steels in gold mining environments," *British Corrosion Journal*, vol. 29, no. 4, pp. 271-274, 1994.
- [42] R. Andrew, "Corrosion problems and their solutions in South African deep level gold mines," *British Corrosion Journal*, vol. 29, no. 3, pp. 219-225, 1999.
- [43] G. Singh, "A Survey of Corrosivity of Underground Mine Waters From Indian Coal Mines," *International Journal of Mine Water*, vol. 5, no. 1, pp. 21-32, 1986.
- [44] ASTM Standard G31, 2012, "Laboratory Immersion Corrosion Testing of Metals," ASTM International, West Conshohocken, Pennsylvania, USA, 2012.
- [45] ISO 9227, 2012, "Corrosion tests in artificial atmospheres - Salt spray tests," ISO/IEC, Geneva, Switzerland, 2012.
- [46] ISO 11130, 2010, "Corrosion of metals and alloys - Alternate immersion test in salt solution," ISO/IEC, Geneva, Switzerland, 2010.
- [47] ISO 14993, 2001, "Corrosion of metals and alloys - Accelerated testing involving cyclic exposure to salt mist, "dry" and "wet" conditions," ISO/IEC, Geneva, Switzerland, 2001.
- [48] P. A. M. H. J. T. T. Albrecht, "Atmospheric Corrosion Resistance of Structural Steels," *Journal of Materials In Civil Engineering*, vol. 15, pp. 2-24, 2003.
- [49] ASTM A572, 2013, "Standard Specification for High-Strength Low-Alloy Columbium-Vanadium Structural Steel," ASTM International, West Conshohocken, Pennsylvania, USA, 2013.
- [50] W. Wang, X. Qian, R. Su and X. Wang, "Tensile tests and analyses of notched specimens fabricated from high strength steels using a generalized yield model," *Fatigue & Fracture of Engineering Materials & Alloys*, vol. 33, pp. 310-319, 2010.
- [51] W. Yu, J. Zhao and J. Shi, "Dynamic mechanical behaviour of Q345 steel at elevated temperatures: experimental study," *Materials at High Temperatures*, vol. 27, no. 3, pp. 285-293, 2010.

- [52] S. Yao, L. Du and G. Wang, "Preparation of Diversified Ultra-Fine Microstructures in Q345 Steel with Improved Properties," *Steel Research International*, vol. 82, no. 7, pp. 806-808, 2011.
- [53] Y. Xiong and X. X. Hu, "The effect of microstructures on fatigue crack growth in Q345 steel welded joint," *Fatigue & Fracture of Engineering Materials & Structures*, vol. 35, pp. 500-512, 2011.
- [54] L. Baotung, L. Xiaoyan and Z. Xiulin, "Effects of Microstructure on Fatigue Crack Initiation and Propagation of 16Mn Steel," *Metallurgical Transactions A*, vol. 20A, pp. 413-419, 1989.
- [55] Y. Liu and S. Mahadevan, "Stochastic fatigue damage modeling under variable amplitude loading," *International Journal of Fatigue*, vol. 29, pp. 1149-1161, 2007.
- [56] L. Ji-xiong, C. Shi-hua, L. Jing, Z. Wan-ling and C. Xiao, "Evaluation of Anti-Weathering Performance of Different Construction Steels by in-Door Cyclic Corrosion Tests," in *Sino-Swedish Structural Materials Symposium 2007*, Beijing, China, 2007.
- [57] Z. Xueyong, G. Aimin, Y. Shanwy, W. Xuemin, Z. Yuntang, T. Ying, Z. Dehui and H. Xinlai, "Study on the Microstructure, Mechanical Properties and Corrosion Resistance of a Novel HSLA Steel," *Kang T'ieh/Iron and Steel (Peking)*, vol. 40, pp. 417-421, 2005.
- [58] Y. Wu, B. Cao and Z. Fang, "SCC Susceptibility of Steel 16Mn in Nitrate Solution and Its Mechanism," *Journal of University of Science and Technology Beijing*, vol. 9, no. 1, pp. 31-35, 2002.
- [59] L. Sharon, Interviewee, *University of Windsor, Personal Communication*. [Interview]. 13 February 2014.
- [60] T. J. Collins, "ImageJ for microscopy," *BioTechniques*, vol. 43, no. 1, pp. S25-S30, 2007.
- [61] E. Pavlina and C. Van Tyne, "Correlation of Yield Strength and Tensile Strength with Hardness for Steels," *Journal of Materials Engineering and Performance*, vol. 17, no. 6, pp. 888-893, 2008.
- [62] ASTM E18, 2014, "Standard Test Methods for Rockwell Hardness of Metallic Materials," ASTM International, West Conshohocken, Pennsylvania, USA, 2014.
- [63] ASTM E8/E8M, 2013, "Standard Test Methods for Tension Testing of Metallic Materials," ASTM International, West Conshohocken, Pennsylvania, USA, 2013.

APPENDIX A: SUMMARY OF CORROSION CONDITIONS IN SELECT MINES

Source	Type	Location	Tmp. (°C)	Water						Atmosphere		Notes
				pH	Oxygen Content (ppm or stated)	Solids Dissolved (ppm or stated)	Hardness (CaCo3 ppm or stated)	Chloride Content (ppm or stated)	Sulfate Content (ppm or stated)	Temp. Dry (°C)	Relative Humidity (%)	
[40]	Coal	PA, USA	N/A	3	N/A	2737 max	N/A	16 max	1683 max	N/A	N/A	Acidity: 522 (H2SO4 ppm)
[38]	Gold	South Africa	N/A	range 2-10; mode 7-8	range 2-11 mg/l; mode 6-7 mg/l	range 0-8 g/l; mode 2-3 g/l	range 0-3.5 g/l; mode 0.5-1 g/l	range 0-3 g/l; mode 0.0-0.5 g/l	range 0-3 g/l; mode 0.5-1 g/l	N/A	N/A	Corrosion Rate (steel): mode, 0.2-0.25 mm/yr (~4.31-5.38 g/m ² /day)
[41]	Gold	South Africa	N/A	2.7	N/A	3800	561	28	1829	N/A	N/A	Keep hardness below 34 HRC for type 431 stainless steel to reduce corrosion
[41]	Gold	South Africa	N/A	6.5	N/A	4600	730	1250	1075	N/A	N/A	
[42]	Gold	South Africa	N/A	N/A	N/A	N/A	0.5-0.7 g/l	avg 0.2-0.8 g/l; 2.5 g/l max	avg 0.05-0.2 g/l; 0.6 g/l max	30-45	75-95	Depth 1000-3000 m
[43]	Coal	India	N/A	7.8 avg	N/A	900 avg	500 avg	40 avg	250 avg	N/A	N/A	Mild steel cor. rate 0.21 mg/m ² /day
[43]	Coal	India	N/A	2.9 avg	N/A	N/A	2500 avg	30 avg	2500 avg	N/A	N/A	Mild steel cor. rate of 10.9 mg/m ² /day
[39]	Niobium	QC, CA	15 max	7 min	8.8 max	N/A	N/A	5701 max	247 max	20 max	100 max	Depth 350-442 m
[39]	Gold	QC, CA	11.6 max	6.9 min	9.0 max	N/A	N/A	3128 max	733 max	12 max	100 max	Depth 435-610 m
[39]	Gold	QC, CA	8 max	7.1 min	11.2 max	N/A	N/A	1450 max	84 max	9 max	100 max	Depth 605 m
[39]	Gold	QC, CA	16.8 max	2.9 min	9.0 max	N/A	N/A	140 max	18053 max	19 max	100 max	Depth 460-635 m
[39]	Gold	QC, CA	28.4 max	3.4 min	7.4 max	N/A	N/A	789 max	45757 max	30 max	100 max	Depth 1490-2030 m

VITA AUCTORIS

NAME: Sante Alexander DiCecco

PLACE OF BIRTH: Windsor, Ontario

YEAR OF BIRTH: 1989

EDUCATION: Ontario Secondary School Diploma
Ecole Secondaire E.J. Lajeunesse
Windsor, Ontario
2007

Bachelor of Applied Science
Honours Mechanical Engineering With Materials and Co-op
Options
University of Windsor
Windsor, Ontario
2011

Master of Applied Science
Engineering Materials
University of Windsor
2014